

FINAL REPORT

Lead and Antimony Speciation in Shooting Range Soils: Molecular Scale Analysis, Temporal Trends and Mobility

SERDP Project ER-1770

NOVEMBER 2017

Thomas Trainor
University of Alaska - Fairbanks

Distribution Statement A

This document has been cleared for public release



Page Intentionally Left Blank

This report was prepared under contract to the Department of Defense Strategic Environmental Research and Development Program (SERDP). The publication of this report does not indicate endorsement by the Department of Defense, nor should the contents be construed as reflecting the official policy or position of the Department of Defense. Reference herein to any specific commercial product, process, or service by trade name, trademark, manufacturer, or otherwise, does not necessarily constitute or imply its endorsement, recommendation, or favoring by the Department of Defense.

Page Intentionally Left Blank

REPORT DOCUMENTATION PAGE					Form Approved OMB No. 0704-0188	
<p>The public reporting burden for this collection of information is estimated to average 1 hour per response, including the time for reviewing instructions, searching existing data sources, gathering and maintaining the data needed, and completing and reviewing the collection of information. Send comments regarding this burden estimate or any other aspect of this collection of information, including suggestions for reducing the burden, to Department of Defense, Washington Headquarters Services, Directorate for Information Operations and Reports (0704-0188), 1215 Jefferson Davis Highway, Suite 1204, Arlington, VA 22202-4302. Respondents should be aware that notwithstanding any other provision of law, no person shall be subject to any penalty for failing to comply with a collection of information if it does not display a currently valid OMB control number.</p> <p>PLEASE DO NOT RETURN YOUR FORM TO THE ABOVE ADDRESS.</p>						
1. REPORT DATE (DD-MM-YYYY)		2. REPORT TYPE		3. DATES COVERED (From - To)		
11/20/2017		Final Report		9/17/2010 - 9/17/2013		
4. TITLE AND SUBTITLE Lead and Antimony Speciation in Shooting Range Soils: Molecular Scale Analysis, Temporal Trends and Mobility				5a. CONTRACT NUMBER		
				W912HQ-10-C-0068		
				5b. GRANT NUMBER		
6. AUTHOR(S) Thomas Trainor University of Alaska - Fairbanks Thomas A. Douglas U.S. Army Cold Regions Research and Engineering Laboratory				5c. PROGRAM ELEMENT NUMBER		
				5d. PROJECT NUMBER		
				ER-1770		
7. PERFORMING ORGANIZATION NAME(S) AND ADDRESS(ES) University of Alaska - Fairbanks 505 South Chandalar DriveFairbanks, AK 99775				5e. TASK NUMBER		
				5f. WORK UNIT NUMBER		
9. SPONSORING/MONITORING AGENCY NAME(S) AND ADDRESS(ES) Strategic Environmental Research and Development Program 4800 Mark Center Drive, Suite 17D03 Alexandria, VA 22350-3605				8. PERFORMING ORGANIZATION REPORT NUMBER		
				ER-1770		
10. SPONSOR/MONITOR'S ACRONYM(S) SERDP				11. SPONSOR/MONITOR'S REPORT NUMBER(S)		
				ER-1770		
12. DISTRIBUTION/AVAILABILITY STATEMENT Public distribution; unlimited						
13. SUPPLEMENTARY NOTES						
14. ABSTRACT The objective of this project was to provide a detailed analysis of the changes in lead (Pb) and antimony (Sb) speciation that occur over time as bullet fragments weather in shooting range impact berm soils. This project is motivated by the fact that most bullet alloys are composed of about 90% Pb with up to 5% Sb, and lesser amounts of Cu, Ni, Zn and other metal (loid)s. Bullet fragments found in berm soils associated with training activities are highly susceptible to oxidation and weathering processes that can generate mobile and bio-available forms of these metal(loids). This requires a detailed understanding of how the speciation of the key metal(loids) changes under typical soil/geochemical conditions.						
15. SUBJECT TERMS Lead, Antimony, Shooting Range, Soil Chemistry, Hydrogeochemistry						
16. SECURITY CLASSIFICATION OF:			17. LIMITATION OF ABSTRACT	18. NUMBER OF PAGES	19a. NAME OF RESPONSIBLE PERSON	
a. REPORT	b. ABSTRACT	c. THIS PAGE			Thomas Trainor	
UNCLASS	UNCLASS	UNCLASS	UNCLASS	98	19b. TELEPHONE NUMBER (Include area code) 907-474-5628	

Page Intentionally Left Blank

Table of Contents

1. Objective	1
2. Background	3
3. Materials and Methods	6
4. Results and Discussion	8
4.1 Construction of berm facility and basic soil characterization	8
4.2 Mobile Pb and Sb concentrations and speciation in berm runoff	16
4.3 Localized solid phase Sb and Pb speciation in berm soils	16
4.4 Pb and Sb speciation in a historic shooting range berm	19
4.5 Oxidation and mobilization of Sb metal in simulated groundwater	28
4.6 Alteration of Sb metal surfaces in model laboratory systems	31
4.7 Column studies and Pb and Sb attenuation by iron amendments	33
4.8 Structure of sorption complexes binding to a hematite model substrate	44
4.8.1 Pb(II) sorption	46
4.8.2 Sb(V) sorption	50
4.9 Substrates as passive sensors	54
5. Conclusions and Implications for Future Research/Implementation	57
6. Literature Cited	60
Appendix A. Supporting Data	72
Appendix B. List of Publications	80

List of Tables

Table 1. Characterization of soils used to construct the field site impact berms.....	10
Table 2. Total metal concentrations in the 12 test berms analyzed by x-ray fluorescence (XRF). Pristine soil concentrations shown for comparison. LLD = lower limit of detection.	11
Table 3. Fitting parameters and EXAFS results for historic shooting range samples. Fitting was done in R-space, k-weights of 1,2 and 3 were fitted simultaneously and the amplitude reduction factor (S_0) was set at 0.97..	25
Table 4. Composition of the Sb metal oxidation batch reactors. The experiments were performed at 20°C in equilibrium with atmosphere, light was not excluded, pH was measured during sampling.....	28
Table 5. Linear combination fitting results for column experiment end member soil types using reference spectra. Sum (%) refers to the actual sum of the partial contributions of reference spectra for the overall best fit. χ^2 and reduced χ^2 are derived from the fit refinement process. Pb(0) = Metallic bullet alloy; L = Litharge (PbO); C = Cerussite; Ferri = Pb(II) sorbed to Fe(III) oxides; error associated with fit in parenthesis.....	43

List of Figures

Figure 1.	Schematic depiction of some of the potential processes controlling Pb and Sb speciation in shooting range berm soils.....	1
Figure 2.	Field site located on Ft. Greely in Delta, AK; the construction of the new berms and contamination in a controlled event are shown.	8
Figure 3.	Schematic showing layout of the berms. Berms 1-4 are “pristine” and berms 5-12 are “contaminated”.....	9
Figure 4.	Box plot diagram of total Pb (left half) and Sb (right half) concentrations from 2011 to 2014 (prior to Fe addition) as a function of soil type (sand, sandy loam, loamy sand and silt loam) for the duplicate contaminated test berms (a) refers to berms 5, 7, 9, 11 and (b) refers to berms 6, 8, 10, 12. Gray lines indicate median values during the 4 years. The gray boxes depict the lower (25 th percentile) and upper (75 th percentile) quartiles. A, B, C, D, E indicates levels that are statistically different at $p < 0.05$. Levels are not comparable between Pb and Sb. Samples were filtered to 0.45- μ m, acidified with ultra-pure HNO ₃ and analyzed using ICP-MS. Samples were analyzed in triplicate, calibrated to known standards and error values are within 5%.....	12
Figure 5.	The oxidation state of Sb in aqueous samples determined using liquid chromatography coupled to an ICP-MS. (a) standards (100 μ g/L Sb(III) and Sb(V)) and berm water runoff collected (b) summer 2011 and (c) summer 2012.	13
Figure 6.	Pb concentrations in berm runoff as a function of soil type for the duplicate berms (a) 5, (b) 6, (c) 7, (d) 8 (e) 9, (f) 10, (g) 11 and (h) 12. ‘Fe’ indicates amended berms and ‘ctrl’ indicates un-amended berms. A, B, C indicate levels that are statistically different at $p < 0.05$, but are not comparable between duplicate soil types. ‘*’ signifies statistical differences between Pb distributions between the Fe versus control berm runoff..	14
Figure 7.	Sb concentrations in berm runoff as a function of soil type for the duplicate berms (a) 5, (b) 6, (c) 7, (d) 8 (e) 9, (f) 10, (g) 11 and (h) 12. ‘Fe’ indicates amended berms and ‘ctrl’ indicates un-amended berms. A, B, C indicate levels that are statistically different at $p < 0.05$, but are not comparable between duplicate soil types. ‘*’ signifies statistical differences between Sb distributions between the Fe versus control berm runoff..	15
Figure 8.	Normalized Sb-L _{III} μ -XANES spectra for the silt loam berm 12 soil end member. Sample data is in black lines with corresponding LCF plotted in gray circles. Standards are black lines without any overlying gray circles. Dotted line corresponds to the absorption edge for Sb-L _{III} (4132.0 eV).....	16

Figure 9.	Normalized Pb-L _{III} μ -XANES for the end member test berms (5, 12) over 4 years. Sample data is in black lines with corresponding LCF plotted in gray circles. Standards are in black with no fits present. Pb•Ferri corresponds to Pb sorption product with synthesized Fe(III) oxides.	17
Figure 10.	XRF maps showing distributions of Pb (red) and Fe (green) in thin sections collected from the (a) sand and (b) sandy loam test berms in the summer of 2012. Thin section area is 25x25 mm and scale bar units are in μ m. Pb ⁰ = metallic Pb, L = litharge, C = cerussite, H = hydrocerussite.	18
Figure 11.	Composition of an unweathered 5.56 mm bullet. (a) Back scatter electron image showing chemically distinct zones. (b) Schematic depiction of bullet anatomy. (c) WDS elemental map showing heterogeneous distribution of Pb. (d) Metallic Pb spheres designated by arrows are the result of melting during analyses at high beam current (≥ 100 nA). (e) WDS elemental map showing that Sb is relatively well-mixed within Pb in the slug but exists mainly as discrete hotspots (2-5 μ m) within the (f) Pb-rich interlayer.	20
Figure 12.	Metal distribution in the historic shooting range soil. Area of interest outlined in white square is Region 1.	21
Figure 13.	BSE image of Region 1 in Figure 12. The sample features a crack within the Pb-rich rim that propagates and is increasingly (left to right) filled by soil (dark particles). A,B,C represent different areas analyzed.	21
Figure 14.	(a) BSE image showing soil particles embedded between the Cu rim and the Pb-rich interlayer of the bullet. (b) WDS map showing elemental distribution in the bullet and soil, Cu = blue, Pb = green, Al = yellow, Sb = magenta. (c) Pb intensity profile calculated using image greyscale values from the Pb distribution WDS map.	22
Figure 15.	Lead analysis of (a) the hotspot from the historic berm sample, (b) XANES map showing principle Pb components contributing to the signal intensity, and (c) Pb-L _{III} XANES spectra from standards and model compounds (in black) and experimental data (colored). XANES data measured at Pb-L _{III} absorption edge was processed using the Microanalysis Toolkit software developed at the Stanford Synchrotron Radiation Lightsource and LCF of the data was performed using the Athena interface (Ravel and Newville, 2005) to the IFEFFIT (Newville, 2001) program.	23
Figure 16.	Thin section of a bullet collected from the pure sand newly constructed berm after 1 year of weathering: (a) and (b) Optical images, and (c) micro-focused x-ray fluorescence map of Pb and Fe.. Map was collected on BL2-3, Stanford Synchrotron Radiation Lightsource, Palo Alto, CA and optical images were collected on Leica Optical Microscope at Advanced Instrumentation Laboratory, University of Alaska Fairbanks	24

Figure 17.	Sb K-edge EXAFS spectra of samples collected from the historic shooting range (weathering crust and Region 1), a laboratory generated sample (Sb soil) and an unfired, new bullet. Empty gray circles correspond to experimental data and solid black lines represent best fit. EXAFS data was processed using the Athena interface (Ravel and Newville, 2005) to the IFEFFIT (Newville, 2001) program. The background subtraction, normalization, and conversion into k-space was performed (Kelly et al., 2008), the spectra was Fourier transformed over k-range from 3-9, and analyzed using the Artemis interface (Ravel and Newville, 2005) to the IFEFFIT (Newville, 2001) program. Theoretical scattering paths were based on the crystal structure of Sb_2O_5 (Jansen, 1979).	26
Figure 18.	Antimony oxidation and dissolution in batch reactors as a function of time: a) Changes in the aqueous concentration of the total dissolved antimony; b) The extent of Sb(0) oxidation to Sb(III) and further to Sb(V).	29
Figure 19.	EXAFS data (solid lines) and fit (empty circles) for Sb(0), senarmontite, and the post-reaction solids collected after 5 months of reaction from the DI/Sb and SGW/Sb batch reactors.	30
Figure 20.	Processes observed in the batch reactors: heterogeneous oxidation of Sb(0) to Sb(III) and, further, to Sb(V), homogeneous oxidation of Sb(III) to Sb(V), and precipitation/dissolution of the Sb(III) and Sb(V) phases.	31
Figure 21.	Comparison of antimony (Sb) metal surfaces before and after 51 days of equilibration: (a) clean Sb surface, (b) and (c) photo and scanning electron microscope image (SEM) of Sb surface reacted in deionized water, (d) SEM of a surface reacted in simulated groundwater (SGW) pH = 5.6, (e) SEM of a surface in SGW pH = 7.5, (f) and (g) SEM and photo of a surface reacted in SGW pH = 8.4.	32
Figure 22.	Orientation of two polymorphs of Sb_2O_3 , isometric senarmontite and orthorhombic valentinite, identified on surface of antimony metal reacted for 51 days in a simulated groundwater ($I = 0.01 \text{ M NaNO}_3$) with initial pH adjusted to 8.4 by Na_2CO_3 .	32
Figure 23.	Box plot of Sb concentrations in runoff leachate for each of the soil types in all the columns prior to the Fe additions. Concentrations of Sb in each soil type leachate were measured in triplicate indicated by 'a, b, c' on the plot. Plot is arranged in order of increasing % of sand. Dark gray lines indicate median values during the runoff experiment (prior to the Fe additions) and the gray boxes depict the lower (25 th percentile) and upper (75 th percentile) quartiles. A, B, C, D, E indicates levels that are statistically different between data sets using one-way ANOVA with bivariate analysis and Student's t-test to compare means, p-value < 0.05. Levels connected by the same letter were determined to not be significantly different at $p < 0.05$.	34

Figure 24. Box plot of Pb concentrations in runoff leachate for each of the soil types in all the columns prior to the Fe additions. Concentrations of Sb in each soil type leachate were measured in triplicate indicated by 'a, b, c' on the plot. Plot is arranged in order of increasing % of sand. Dark gray lines indicate median values during the runoff experiment (prior to the Fe additions) and the gray boxes depict the lower (25 th percentile) and upper (75 th percentile) quartiles. A, B, C, D indicates levels that are statistically different between data sets using one-way ANOVA with bivariate analysis and Student's t-test to compare means, p-value <0.05. Levels connected by the same letter were determined to not be significantly different at $p < 0.05$.	35
Figure 25. Effects of saturation time on Pb concentrations as a function of soil type and column set (a, Columns 1-4; b, columns 5-8; and c, columns 9-12) in triplicate in the column runoff experiment.	36
Figure 26. Effects of saturation time on Sb concentrations as a function of soil type and column set (a, Columns 1-4; b, columns 5-8; and c, columns 9-12) in triplicate in the column runoff experiment.	37
Figure 27. Antimony concentrations in runoff leachate for the (a) silt loam column set and the (b) sand column set (soil type end members). The amendments were added after runoff sample 15 and were (1) no amendment in the controls, (2) nZVI and (3) $\text{FeCl}_2 + \text{CaCO}_3$. Black dotted line indicates when the amendments were added.	38
Figure 28. Lead concentrations in runoff leachate for the (a) silt loam column set and the (b) sand column set (soil type end members). The amendments were added after runoff sample 15 and were (1) no amendment in the controls, (2) nZVI and (3) $\text{FeCl}_2 + \text{CaCO}_3$ (plotted on the right axis for scale). Black dotted line indicates when the amendments were added.	39
Figure 29. Trends between log Pb and Sb concentrations ($\mu\text{g/L}$) and pH as a function of soil type in the Fe(II) amended columns.	40
Figure 30. FFF-ICP-MS results of the sandy loam mixed soil column and the silt loam soil after the addition of the Fe(II) amendment. (a, b) correspond to FFF fractogram of time versus UV detector response (a; 254 nm and b; 284 nm) and (c, d) refers to in-line coupling to ICP-MS detector counts. There is approximately a 100 second delay between FFF and ICP-MS signal. The ICP-MS data has been normalized to 1 and stacked. The UV detector signal has been visually increased in (f) for the sandy loam and (g) for the silt loam with Fe(II) addition. The ICP-MS counts (not normalized) were visually increased in (e) for the sandy loam and (h) for the silt loam with Fe(II) addition.	41

- Figure 31. Normalized Pb-L_{III} μ -XANES spectra of end member column samples and corresponding linear combination fits. Black lines representing the LCF fits. Black dotted line represents the Pb L_{III} absorption edge. 42
- Figure 32. Normalized Sb-L_{III} μ -XANES spectra of (a) standards and model compounds used for visual comparison with (b) column samples. 43
- Figure 33. (A) Layer stacking sequence along the C_s axis for the full layer termination ($\bar{1}\bar{1}02$); (B) Layer stacking sequence along the C_s axis for the half layer termination ($\bar{1}\bar{1}02$); (C) polyhedral representation of the oxygen-terminated full layer termination surface of hematite ($\bar{1}\bar{1}02$) (second octahedral layer and those beneath are not shown for clarity) ; (D) polyhedral representation of the oxygen-terminated half layer termination surface of hematite ($\bar{1}\bar{1}02$) (second octahedral layer and those beneath are not shown for clarity). Lengths for unit cell edges are $a_s=5.035$ Å, $b_s=5.427$ Å and $c_s=7.364$ Å. The ^{III}O, ^{II}O, and ^IO represent oxygen triply, doubly and singly coordinated to iron, respectively. Each atom layer is labelled as “Layer-n E”, where n is integer from 1 and E is the element symbol for either O or Fe. 45
- Figure 34. Experimental structure factors (F_{HKL}) as a function of perpendicular momentum transfer (L, in reciprocal lattice units) for the hematite ($\bar{1}\bar{1}02$); surface reacted with 200 μ M Pb(II) at pH 5.5. The red solid lines represent the calculated CTR profiles based on the optimized model O1O3_O1O4 and the green dashed lines represent the calculated CTR profiles based on the optimized model O5O7_O5O8. 46
- Figure 35. Structures of surface complex species with two types of edge-sharing binding configurations on the HLT based on the best fit model. The top view of the interfacial structure for Pb binding at site O₂O_{4+x} (A) and site O₂O_{3+x} (C) with the first Fe layer visualized as octahedra and the local structure of surface complex species as ball and stick models with green spheres representing distal oxygen, red spheres surface binding oxygen, and gray spheres Pb. Symmetry related sites are omitted for clarity. Detailed structural information for the surface complex species at site O1O3 (B) and site O1O4 (D) in terms of bond angles (°) and bond lengths (Å). The near neighbor Fe atoms (blue spheres) are shown as well. 47
- Figure 36. (A) Schematic showing inter-site distances identified from a fully occupied super cell. (B) The simulated site coverage (%) as a function of the Pb-Pb cutoff distances. The horizontal dashed line marks the CTR derived site occupancy. (C) Simulated site occupation pattern associated with a Pb-Pb cutoff distance of 5.42 Å, where the circles in different colors highlight the adjacent sites of same type aligned along b_s. (D) Maximum site occupation via super lattice formation satisfying the cutoff Pb-Pb distance of 5.42 Å. 49
- Figure 37. Experimental (gray circles) and model-based structure factors (F_{HKL}) as a function of perpendicular momentum transfer (L, in reciprocal lattice units) for

the hematite ($1\bar{1}02$) surface reacted with 200 μM Sb(V) at pH 5.5. The solid lines in green represent the calculated CTR profiles based on the best fit model Model4, solid lines in blue represent the calculated CTR profiles based on the best fit model Model6, and solid lines in red represent the calculated CTR profiles based on the best fit model Model5	51
Figure 38. (A) Octahedral local structure of the Sb(V) surface complex in the best fit model structure. (B) bond lengths of the Sb(V) surface complex. (C) Surface binding structure and atomic layer spacing values for Sb(V) sorbed to the half layer termination based on the best fit model structure for Model5.....	52
Figure 39. Field deployment of (a) single crystal hematite ($\alpha\text{-Fe}_2\text{O}_3$) and (b) polished antimony metal chip in (c) acid washed quartz (SiO_2) sand; (d) samples were reacted for 30 days.....	54
Figure 40. Fluorescence yield for the surface of a single surface hematite ($\alpha\text{-Fe}_2\text{O}_3$) crystal after 30-day deployment in the contaminated soil of a newly constructed berm. Fluorescence data (dashed) are contrasted with the surface x-ray reflectivity (solid). Concurrent measurements were conducted at two beam energies, 6.9 and 13.5 keV, at GSECARS, Advanced Photon Source, Chicago, IL.....	55
Figure 41. Simplified conceptual model of key processes controlling the mobilization of Pb and Sb within the berm soils.	57

List of Acronyms

APS – Advanced Photon Source

CRTC – Cold Regions Test Center

CTR – crystal truncation rods

DoD – US Department of Defense

EDTA – ethylenediaminetetraacetic acid

EPA – US Environmental Protection Agency

EXAFS – extended x-ray absorption fine structure spectroscopy

GI-FY – grazing incidence angle fluorescent yield

GI-XAFS – grazing incidence angle x-ray absorption fine spectroscopy

GI-XRD – grazing incidence angle x-ray diffraction

GSECARS – GeoSoilEnviro Center for Advanced Radiation Sources

ICP-MS – inductively coupled plasma-mass spectrometer

LC-ICP-MS – liquid chromatography coupled to inductively coupled plasma-mass spectrometer

LCF – linear combination fitting

PCA – principle component analysis

PTFE – polytetrafluoroethylene (Teflon)

RAXS – resonant anomalous x-ray scattering

SEM – scanning electron microscopy

SOM – soil organic matter

SSRL – Stanford Synchrotron Radiation Laboratory

WDS – wavelength dispersive spectroscopy

XAFS – x-ray absorption fine structure spectroscopy

XANES – x-ray absorption near-edge structure

XR – high resolution x-ray reflectivity

XRD – x-ray powder diffraction

XRF – x-ray fluorescence

Keywords

Lead, Antimony, Shooting Range, Soil Chemistry, Hydrogeochemistry

Acknowledgements

This work is supported by the Strategic Environmental Research and Development Program Grant SERDP ER-1770. Portions of this work were performed at GSECARS (Sector 13), Advanced Photon Source (APS), Argonne National Laboratory. GSECARS is supported by the National Science Foundation (EAR-1128799) and Department of Energy (DE-FG02-94ER14466), and at the Stanford Synchrotron Radiation Laboratory supported by the Department of Energy Office of Basic Energy Sciences. We also acknowledge the University of Alaska Advanced Instrumentation Laboratory for extensive support in obtaining the analytical results reported in this work, the Cold Regions Test Center (Ft. Greely Alaska) for field support, and the Alaska Army National Guard Ft. Greely MP Company, 49th Missile Defense Battalion.

Abstract

Objective

The objective of this project was to provide a detailed analysis of the changes in lead (Pb) and antimony (Sb) speciation that occur over time as bullet fragments weather in shooting range impact berm soils. This project is motivated by the fact that most bullet alloys are composed of about 90% Pb with up to 5% Sb, and lesser amounts of Cu, Ni, Zn and other metal(loid)s. Bullet fragments found in berm soils associated with training activities are highly susceptible to oxidation and weathering processes that can generate mobile and bio-available forms of these metal(loids). In order to understand the potential for metal(loid) migration, as well as evaluate remediation scenarios, requires a detailed understanding of how the speciation of the key metal(loids) changes under typical soil/geochemical conditions. Our project set out to investigate three topics related to Pb and Sb in shooting range soils: (i) how soil physical/chemical properties will influence on how metal-fragments weather over time, (ii) understand the significance of sorption processes controlling the mobility of Pb and Sb in range soils, and (iii) determine how the mobility of the oxidized Pb and Sb metals depends on soil solution properties such as pH. Finally, we also set out to test the use of iron-amendments as a means of limiting the mobility of both Pb and Sb range soils.

Technical Approach

We approached these questions with a combination field and laboratory experiments. We constructed a new test site at the Cold Regions Test Center (CRTC) Ft. Greely Donnelly Training Area (DTA), Alaska. At this site we made fresh shooting range berms using four soil types: a local silt-loam end member, a sand end-member and soils of intermediate composition made by mixing the end member. These berms were loaded with bullets in a single controlled firing event and monitored from 2010 to 2016. A series of batch reactor studies was performed with a focus on characterizing oxidation rates and products, particularly for Sb metal. Column experiments, using the range soils, were used to investigate weathering rates and metal(loid) speciation under controlled conditions, including the degree of soil saturation. These studies were also used to investigate the proposed amendment procedure and to test the degree to which metal(loids) may be mobilized via colloid facilitated transport. These measurements were complimented by a series of surface specific measurements used to investigate the speciation / structure of Pb and Sb sorbed to iron-oxide surfaces. These surface measurements also formed the basis for understanding the efficacy of using well characterized mineral substrates as a passive sensor, useful for providing a qualitative indication of metal(loid) mobility. These studies were carried out using a range of analytical tools; traditional of soil and solution composition analysis, aqueous speciation methods for distinguishing between Sb(III) and Sb(V), colloid characterization/separation methods, solid phase analysis using electron probe and synchrotron x-ray methods, and surface specific diffraction techniques. These experimental methods and analytical tools generated a unique data set of trace element speciation and temporal/spatial variation with physicochemical conditions.

Results

Solution samples from berm runoff and column experiments were monitored for total “dissolved” metal(loid) concentrations. An important observation from the solution data is that the Pb and Sb are highly mobile, with concentrations on the order of 10’s to 100’s of $\mu\text{g/L}$ sustained over the course of the experiments in all soil types. Furthermore, we observe that while Sb only makes up roughly 1wt% of the bullets used (99wt% Pb), the dissolved concentrations of Sb typically exceeded the Pb, showing that Sb is highly susceptible to oxidation and mobilization in the test soils. Speciation analysis confirmed that the mobile Sb was dominated by Sb(V), with only a trace of Sb(III) ever being observed in solution. Field flow fractionation measurements of solutions from soils and column experiments show that the majority of Sb is truly dissolved, while a significant fraction of “dissolved” (operationally defined by 0.45 μm filter) was actually associated with Fe-bearing colloids, and to a lesser extent organic colloids. Our measurements suggest that Pb concentrations did not strongly vary with soil type, while the Sb concentrations showed a trend towards greater mobility in higher sand content soils. The observation of rapid oxidation agrees with our batch studies of oxidation rates of metallic Sb, where initial oxidation to aqueous Sb(III) is rapid in a range of solution conditions. The further oxidation to Sb(V) is also rapid, but is strongly influenced by the solution composition, as is the ultimate weathering (solid phase) products in highly concentrated systems. Characterization of the solid phase speciation in test soils and in historic range soils show that Pb forms PbO, and increasingly over PbCO₃ as the primary weathering phases – which are in turn likely the predominant sources of dissolved Pb(II). We found little evidence of secondary minerals containing oxidized Sb in the test soils. Both Pb and Sb were found to sorb to minerals in the soil matrix, with iron-oxides serving as the predominant sorbent. Our studies of Pb(II) and Sb(V) binding to model iron-oxide substrates shows that both species form inner-sphere multi-dentate coordination with the mineral surfaces – suggesting strong sorbate-sorbent interaction. Our studies of the use of iron as a potential soil amendment show that it may be highly effective for reducing dissolved Sb concentrations. However, the difficulty in controlling pH indicates that such treatments may result in increases in Pb concentrations, emphasizing the difficulty in controlling both the cation and oxyanion mobilities with a single treatment.

Benefits

This study provides a highly detailed analysis of the speciation changes observed for Pb and Sb during the weathering of bullets in a range soil environments. Results of this work contribute to building a model of the weathering and mobilization pathways, that is essential to assessing risk and predicting the efficacy of remediation scenarios. This work also highlights how some solution and solid phase speciation tools may be used in complement to traditional analytical methods in providing a detailed characterization of weathering processes.

1. Objective

The objective of this project was to provide a detailed analysis of the changes in lead (Pb) and antimony (Sb) speciation that occur over time as bullet fragments weather in shooting range impact berm soils. The US Department of Defense (DoD) manages more than 3,000 active small arms training facilities (IRTC, 2003), some of which are highly contaminated with metals due to bullet fragments weathering after decades of repetitive use (Clausen et al., 2004). Most bullet alloys are composed of about 90% Pb with up to 5% Sb, and lesser amounts of Cu, Ni, Zn and other metal(loid)s (Scheuhammer and Norris, 1995; Basunia and Landsberger, 2001; Randich et al., 2002; Walsh, 2004; Johnson et al., 2005; Strömseng et al., 2009; Sanderson, et al., 2010; Martin et al., 2013; Guemiza, et al., 2014). Fragments of bullets and other munitions are highly susceptible to oxidation and weathering processes in soil systems (Vantelon et al., 2005). Understanding the potential for metal(loid) migration from shooting ranges into surface or subsurface aquatic systems is a priority for DoD land managers (Murray et al., 1997). Furthermore, the ability to stabilize or remediate existing sites, and construct new sustainable training facilities, requires having a fundamental understanding of the chemical pathways of transformation of metals in soil systems.

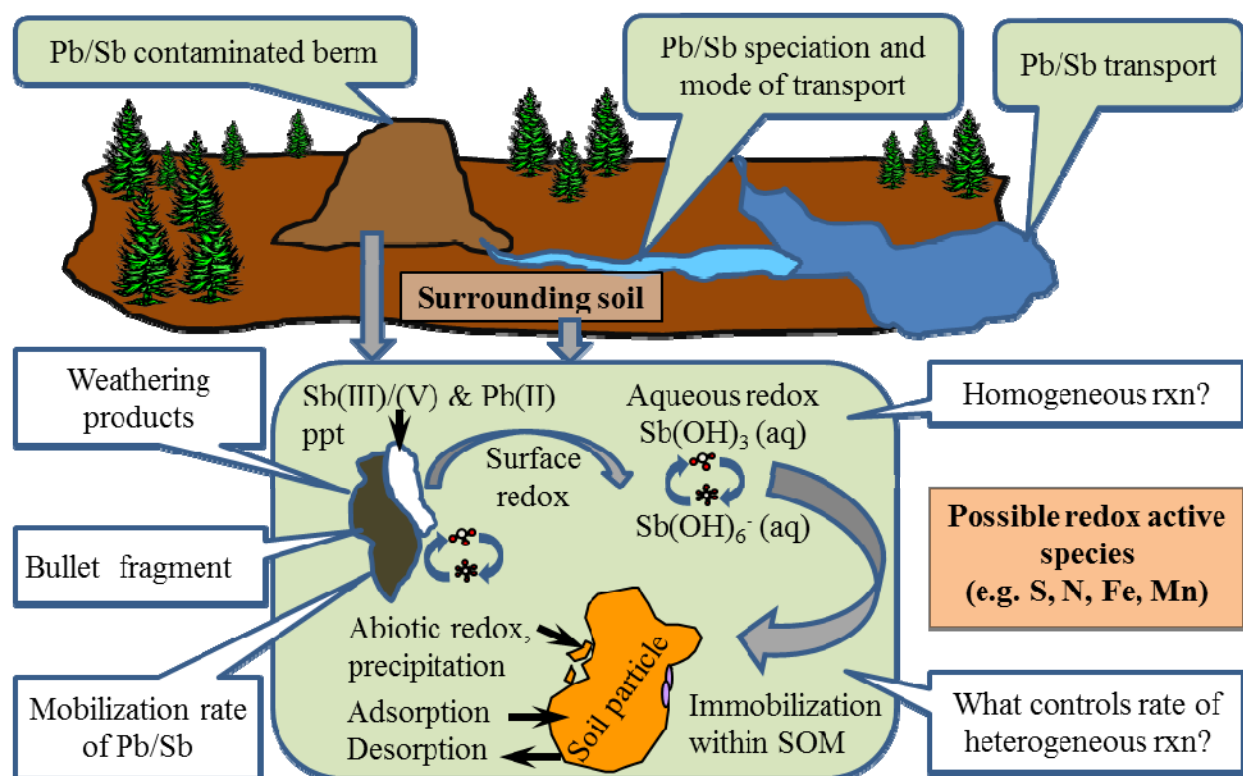


Figure 1. Schematic depiction of some of the potential processes controlling Pb and Sb speciation in shooting range berm soils.

The geochemical processes during bullet weathering in soils are unique relative to other metal contamination situations, mostly due to the high localized concentrations and redox disequilibrium between the bullet fragments (zero-valent metals) and the oxidizing soils. The core of a bullet is composed of a Pb-alloyed core with Sb added as a hardening agent, with average concentrations ranging from 0.7 wt. % Sb (Randich et al., 2002) for a 0.22 caliber (5.56 mm) to 1.8 wt. % Sb for a 0.357 caliber (9 mm) round (Keto, 1999). Concentrations of Sb in shooting range soils have been reported from 1-517 mg/kg in a Texas firing range (Basunia and Landsberger, 2001) to upwards of 10,000 mg/kg at a Swiss shooting range reported by Johnson et al., 2005 of the <0.5 mm sieved bank material including bullets. Lead concentrations have been found in the range of 11 to 4675 mg/kg (Basunia and Landsberger, 2001), 1142 mg/kg (Hardison et al., 2004) and 68,000 mg/kg (Vantelon et al., 2005). In addition to Pb and Sb, elevated (above background) concentrations of Cu have been reported in shooting range soils, approximately 13 to 359 mg/kg (Basunia and Landsberger, 2001). When a small arms round impacts a berm the bullet is fragmented, exposing fresh metallic surfaces that are highly susceptible to oxidation and alteration. The oxidized metals may be released directly into soil solution or bound within secondary mineral phases associated with metal fragment surfaces. In the latter case these alteration products serve as a secondary source of metals to soil water through dissolution pathways. Once metal(loid)s are released into soil pore waters, their dispersion and potential for transport are largely controlled by partitioning and the heterogeneous chemistry at the mineral/soil solution interface (Jørgensen and Willems, 1987; Hardison et al., 2004; Scheinost et al., 2006). These processes are outlined in the schematic diagram depicted in **Figure 1**. Among the key questions that need to be addressed for understanding the transport and biological availability of metals in such systems are (i) what are the most important physical and (bio)geochemical factors dictating the predominant transformation pathways, and (ii) what are the corresponding relevant timescales when considering contaminant migration and remediation scenarios?

A novel aspect of our project is the construction of target berms into which small arms rounds have been fired during a controlled event. This controlled in-situ experiment allows for the testing of a number of hypotheses related to understanding how soil physicochemical properties influence weathering rates of metallic fragments and the transport/retention of metal(loid)s in shooting range soils. The berms we constructed are located adjacent to an existing berm, which has been in use for 15+ years. We are monitoring both the newly constructed and the historic berms in order to observe the long term fate of metals in berm soils under the same hydrologic and climate conditions. In addition, we designed a series of laboratory based experiments to address specific questions about chemical controls on lead and antimony speciation (changes).

Our work focused on three specific hypotheses related to understanding the controls of Pb and Sb speciation in range berm soils:

1. The extent of surface alteration of bullet fragments and the chemical form of surface alteration products is strongly influenced by the hydraulic conductivity and composition of berm soils. In particular, soil properties will determine how mineral surfaces evolve over time towards different steady state conditions.

- Metal fragments in low hydraulic conductivity soils will have more heavily reacted surfaces, with alteration products remaining in place. The alteration products (once formed) will resemble those predicted from equilibrium analysis based on pore water composition, which in turn is controlled largely by soil composition. Surface alteration will result in passivation, which ultimately then slows the release of metals into soil solution.
 - In high hydraulic conductivity soils the higher rate of flow, combined with the more dilute composition of soil pore waters, will result in less extensive alteration of bullet fragment surfaces. Metal fragment weathering will be associated with mild surface oxidation and the more extensive release of oxidized metals to solution rather than the deposition of alteration products in proximity to the source.
2. The chemical speciation of metal(loid)s released into solution will be dominantly controlled by partitioning reactions between soil solution and fine grained soil minerals.
- In low hydraulic conductivity soils with a high proportion of fine grained oxides and clay minerals, metal dispersion will be limited and speciation will be dominated by relatively high concentrations of adsorbed or co-precipitated metal(loid) species. The metal(loid) speciation will locally reflect near equilibrium conditions.
 - High hydraulic conductivity soils will also be dominated by the adsorption of metals, however, binding will be dominated by easily exchangeable species, and metal(loid)s will be more dispersed.
3. Once released into solution, differences in mobility between lead and antimony are correlated with geochemical properties and element speciation. Under circum-neutral pH conditions, lead in solution will be oxidized and found primarily associated with fine grained oxides, while antimony will be predominantly in the +5 oxidation state and will be substantially more mobile than lead.

Many shooting ranges have been used for decades, and the (bio)geochemical processes that control bullet fragment weathering occur on timescales of hours to multiple years. To address this large temporal range, our study was designed to allow for long term monitoring of the solid and aqueous composition, as well as the speciation of lead and antimony in newly constructed and bullet loaded berm soils of variable composition/physical properties. The temporal evolution of the geochemistry in these berms is compared with (1) geochemical data collected on the bullets from the historic berm (located at our field site) and (2) the results from focused short-term laboratory measurements of the oxidation rates and speciation changes under controlled conditions. Furthermore, we have investigated the use of a simple soil amendment for the stabilization of Pb and Sb in soils. Such amendment procedures are intended to provide a cost effective method for limiting metal(loid) mobility. The difficulty is trying to find a single amendment that can stabilize both cations (such as oxidized Pb) and the oxyanions (such as oxidized Sb) that are the primary contaminants associated with spent bullets.

2. Background

The chemical fate, mobility and ultimate bioavailability of metal(loid)s deposited into soils are controlled by a complex array of chemical, biological and physical processes that directly or indirectly affect contaminant speciation. A number of previous studies have focused on characterizing these processes in firing range soils (Lin, 1996; Murray et al., 1997; Astrup et al., 1999; Chen et al., 2002; Cao et al., 2003a, 2003b; Clausen et al., 2003; Garten et al., 2003; Labare et al., 2004; Johnson et al., 2005; Duggan et al., 2007; Ackermann et al., 2009; Clausen et al., 2011; Guemiza, et al., 2014). However, there remains a limited understanding of molecular scale processes that control speciation, bullet fragment weathering and dispersion rates of metal(loid)s in soil pore waters. Also, shooting range field studies tend to focus on characterizing speciation products from very old shooting ranges (Ackermann, et al., 2009; Vantelon, et al., 2005; Scheinost, et al., 2006), >90 years old in some cases, only speculating on the initial oxidation pathways. Detailed knowledge of the weathering/alteration pathways of metallic fragments in soils and the mobilization versus retention of oxidized metal(loid) species as a function of time and varying soil properties are essential for developing accurate assessments of the environmental risk associated with bullet fragments in shooting ranges (Bridges et al., 2008). Molecular characterization of reaction pathways utilized in this project offers the opportunity to construct qualitative and quantitative models based on chemical mechanisms. As a consequence, the results can be extrapolated to a variety of physical and (bio)geochemical conditions. This knowledge is important for understanding the efficacy of potential remediation scenarios and in providing constraints on future site design and monitoring efforts.

Because of their widespread occurrence, potential for offsite migration and high toxicity, the majority of our efforts are focused on furthering our understanding of factors controlling lead and antimony speciation in shooting range soils. Lead fragments from small arms are highly susceptible to oxidation, which may result in the release of aqueous Pb(II) directly to solution. However, oxidized Pb is also often bound with secondary mineral phases such as Pb(II)-carbonate or Pb(II)-sulfate that may be associated with Pb metal surfaces (Lin et al., 1995, 1996; Sturchio et al., 1997). The complete transformation from the metallic to the oxidized form occurs over timescales of years to decades (Lin et al., 1995; Lin, 1996). The rate and extent of formation of the secondary minerals and the release of dissolved species through oxidation/dissolution of the metallic fragments and/or secondary mineral phases is largely dependent on pH, the reduction/oxidation (redox) potential of the soil and the physical history of the substrate (Jørgensen and Willems, 1987; Astrup et al., 1999; Cao et al., 2003a,b). Once Pb is released into solution its mobility is typically controlled by adsorption reactions, where aqueous Pb(II) shows a strong affinity for binding to metal (hydr)oxides in the (high surface area) fine fractions of soils and sediments (Bargar et al., 1997; Ostergren et al., 1999; Strawn and Sparks, 1999; Janssen et al., 2007).

The high affinity for Pb(II) binding to oxides is typically attributed to the formation of strong inner-sphere complexes, particularly with oxides of iron (Bargar et al., 1997, 2004). Model system studies indicate that Pb(II) binding to clay minerals (Strawn and Sparks, 1999) and aluminum oxides (Bargar et al., 1996, Janssen et al., 2007) are generally weaker, possibly due to outer-sphere adsorption. We have recently proposed a molecular scale interpretation of the

various binding affinities to isostructural forms of Al- and Fe-oxides based on periodic density functional theory studies (Mason et al., 2009). These studies indicate that Pb-O bonding is significantly more covalent in the case of binding to iron oxides, in part due to the contribution of iron d-states. However, the degree of covalency depends on the particular geometry of the adsorption complex and type of binding site on the mineral surface. The binding affinity of Pb for soil minerals is also influenced strongly by solution chemistry, including pH, CO₂ fugacity, and the presence of other dissolved species such as sulfate (Ostergren et al., 2000a,b; Villalobos et al., 2001). These factors may result in the formation of competing solution complexes or the formation of ternary surface complexes.

In field settings, it remains difficult to predict the chemical form/speciation that will dominate under a particular set of (bio)geochemical conditions, making reliable predictions of binding affinity, and hence mobility, difficult at best. Furthermore, recent work suggests that adsorption affinity may be strongly influenced by modification of the substrate surface structure as geochemical conditions vary. For instance, through seasonal periods of soil saturation it is anticipated that the soil redox potential will fluctuate significantly, largely due to microbial activity (Roden and Zachara, 1996; Zachara et al., 2001; Nevin and Lovley, 2002). These fluctuations may be accompanied by dissolution and precipitation of various redox sensitive secondary mineral phases (including oxides and clay minerals), and variable concentrations of redox active solutes in solution such as Fe(II) (Hansel et al., 2005). The reaction of soil mineral surfaces with solutes such as Fe(II) results in a transformation of the structure and stoichiometry of the mineral surfaces, including changes in the predominant coordination chemistry of surface functional groups (Tanwar et al., 2008), the growth of partially ordered overlayers, or surface roughening/changes in topography due to dissolution and growth (Yanina and Rosso, 2008). These structural changes are likely to lead to alterations in the surface reactivity, and hence to variations in adsorbate binding affinity due to changes in the substrate (Tanwar et al., 2008). The fate, and molecular-/nano-scale geochemical speciation of Pb in firing range impact berm soils is a major focus of this study, with the goal of connecting the aforementioned model system studies to the different environmental conditions in the experimental berm facility constructed as part of this project.

Lead bullets typically contain up to a few weight percent of Sb. Hence the oxidation of bullet fragments will also generate significant quantities of potentially highly mobile oxidized Sb species. The fate of Sb in natural waters is controlled by its oxidation state, the formation of solution complexes, and its association with secondary (hydr)oxide phases of Fe-, Mn-, Al-, or organic matter. Furthermore, the potential bioavailability and risks for human and wildlife exposure to Sb depend directly on its speciation, as Sb(III) is believed to be more toxic than Sb(V) (Bencze, 1994; Gurnani et al., 1994). However, the relative importance of the various species and partitioning mechanisms controlling the fate and mobility of Sb are poorly understood (Filella et al., 2002; Scheinost et al., 2006; Leuz et al., 2006). The natural occurrence and chemical behavior of Sb is generally assumed to be similar to arsenic, and like arsenic, Sb is considered highly toxic (maximum contaminant level for Sb in drinking water is 6 µg L⁻¹ (U.S. EPA, 2009)), as well as a suspected carcinogen (IARC, 1989). In ore deposits Sb typically occurs as the sulfide mineral stibnite (Sb₂S₃), which is transformed into stibiconite (Sb₃O₆OH) or other oxides and sulfosalts accompanied by the soluble Sb(III) and Sb(V) oxyanions during oxidative weathering (Filella et al., 2002; Ritchie et al., 2013). Model system studies further

indicate that aqueous Sb(III) is readily oxidized under environmental conditions (Luez et. al., 2006; Ilgen et al., 2011, 2012), producing aqueous Sb(V). The fully oxidized form, Sb(V), tends to be highly mobile due to the relatively low binding affinity of this oxyanion species to clay and oxide mineral surfaces, however, analysis of field samples from mine impacted drainages suggests that co-precipitation with poorly crystalline iron-oxides may be a significant sequestration mechanism (Ritchie et al., 2013). Regarding the factors controlling the fate of Pb in soil systems, such as competing adsorbates and the influence of surface structure on the sorption affinity, very little data exists for Sb species. Due to the limited understanding of the geochemical behavior of Sb in firing range soils the molecular processes controlling Sb speciation in small arms impact berm soils are a major focus of our study.

Our current research builds upon previous field and model system studies of Pb and Sb speciation by improving our understanding of the molecular scale speciation and rates of processes in complex soils found on small arms shooting ranges and munitions impact areas.

3. Materials and Methods

Our approach combined long term monitoring of field experiments and parallel batch experiments with state-of-the-art investigation of molecular speciation under realistic soil conditions. Our speciation work is based in large part on the use of (synchrotron based) x-ray scattering and spectroscopy studies of soil materials and “pristine reactive substrates” that are allowed to react in field and laboratory settings. The “reactive substrate” studies in particular directly build on our previous studies of the surface structure, composition and reactivity/trace element binding on single crystal hematite (α -Fe₂O₃), alumina (Al₂O₃), magnetite (Fe₃O₄) and goethite (FeOOH) substrates, which provide a baseline for our proposed work (Trainor et al., 2006; Brown et al., 2007; Ghose et al., 2008). In our previous work we have developed a detailed understanding of how these individual mineral surfaces are modified by their interaction with aqueous solutions and how solutes bind to these surfaces under highly controlled conditions. The results are based on synchrotron surface x-ray diffraction (crystal truncation rod and resonant surface diffraction) and grazing incidence x-ray spectroscopic measurements (long period x-ray standing wave fluorescent yield spectroscopy and grazing angle XAS and reflectivity) (Fenter, 2002; Fenter and Sturchio, 2005; Trainor et. al., 2006). These methods are generally coupled with atomic force microscopy and ab-initio (all electron periodic density functional theory) computational chemistry methods (Eng et al., 2000; Trainor et al., 2002a, 2004, 2006; Brown et al., 2007; Tanwar et al., 2007a,b, 2008; Ghose et al., 2008; Mason et al., 2011). Based on our current studies we are showing that these methods can be used with samples deployed under field conditions in small arms target berms. Analyses of the substrate surfaces (and surfaces modification) provide an element specific picture of the interface structure and composition which is characteristic of the geochemical conditions (e.g. solution chemistry and redox conditions) of the exposed surface and influenced by the mobility/speciation of trace elements (e.g. Pb and Sb, among others) within the soil systems. These same methods are also proving useful for monitoring the in-situ oxidation rates of Sb metal substrates, and in particular allowing us to examine the surface specific speciation changes under a variety of laboratory and field conditions.

The major technical components of this project are categorized as follows:

1. Field studies were performed using well characterized, pristine impact berms constructed with four distinct soils into which small arms rounds were fired during a single controlled event. Physicochemical conditions of the sites, including soil moisture, soil temperature and soil water chemistry, were monitored over time. Soil and water samples were collected routinely from the constructed berms for a detailed analysis to monitor solid and aqueous phase trace element speciation over the time-scale of this study. These results are compared with similar (solid phase) analysis of samples from a historic firing range berm located adjacent to the controlled site. The impact berms were constructed in the summer of 2010 and sample collection and detailed analysis began after bullet deposition. Sample collection and analysis continued through the 2016 field season. In addition we tested the efficacy of a soil amendment using $\text{FeCl}_2/\text{CaCO}_3$ additions to duplicate berms to determine if these additions could limit mobility of both Pb and Sb from the soils.
2. Laboratory studies were performed using batch and column reactors to (i) examine the rates of Sb oxidation under variety of (controlled) geochemical conditions, and (ii) test different soil amendment scenarios. In these studies we controlled parameters such as aqueous composition and pH in order to have laboratory analogs for interpretation of field results.
3. Surface speciation of Pb and Sb were studied in detail using pristine macroscopic reactive substrates in the field and laboratory settings. The substrates are carefully prepared and characterized prior to exposure to field or laboratory experimental conditions. The substrates act as passive sensors to monitor oxidation and alteration of metals, integrated geochemical conditions, and metal(loid) transport and speciation. The passive sensors allow the application of a novel array of surface sensitive tools (noted below) that can provide detailed characterization of the speciation (oxidation state) of metals, how they are distributed at the interface of the sensor, and how they are bound (e.g. as adsorbed or precipitated species). These results yield important information about potential for off-site mobility of metals and can be used in conjunction with analytical results on fine grained materials in field and laboratory studies to provide a direct link with theoretical studies of mineral-fluid interface structure and reactivity. We deployed passive sensors in the field impact berms in the summer of 2011 and 2012 to test this approach and compare results with a full suite of measurements of Pb and Sb binding to model iron-oxide substrates to decipher the molecular details of metal ion binding.

Within these technical components we utilize an array of analytical tools to generate the data necessary to address our hypothesis. These techniques include traditional approaches to the analysis of water and soil chemistry including x-ray diffraction, ion-chromatography, ICP-mass spectrometry and conventional potentiometric analysis. Elemental speciation methods include chromatographic and spectrophotometric methods for aqueous speciation, and synchrotron based x-ray spectroscopy, micro-spectroscopy methods for solid phase trace element speciation and micro-scale spatial correlations. Nano- and molecular-scale surface sensitive techniques, including atomic force microscopy, surface x-ray diffraction, grazing incidence x-ray spectroscopy and grazing incidence x-ray diffraction, are utilized to specifically study the alteration of surfaces, and to directly probe the speciation of metal(loid)s associated with surfaces. These experiments and methods generate a highly unique data set of trace element speciation and temporal/spatial variation with physicochemical conditions.

4. Results and Discussion

4.1 Construction of berm facility and basic soil characterization

The field site construction represents one of the central aspects of this project, and provides a novel facility for studying metal transport in shooting range soils. The field site has allowed us to observe, in detail, the progression of Pb and Sb oxidation from time zero (deposition) as a function of differing soil properties. This observed progression gives new insight to the field of metal transport in soil and aqueous media and help interpret some of the findings from other shooting range studies that focused on old field sites.

In this study, we constructed shooting range test berms comprised of four different, well-characterized soils and fired approximately 2,000 - 5.56 mm bullets into each of the berms in the summer of 2010 at the Cold Regions Test Center (CRTC) Ft. Greely Donnelly Training Area (DTA), Alaska (**Figure 2**). Ft. Greely is located at approximately 63°55'N latitude, and has a subarctic climate characteristic of interior Alaska; cold dry winters and warm summers with periodic showery precipitation. Sampling occurred during the summer seasons for a total of 5 years. Samples were collected to determine Pb and Sb aqueous concentrations and speciation using the berm liquid runoff as well as solid-phase speciation. After 4 years of reaction time, slurries of FeCl_2 and CaCO_3 were added to a set of duplicate test berms to evaluate the potential of this treatment as a low-cost, easy to apply remediation strategy for range managers. Given the natural attenuation of both Pb and Sb by Fe present in soil via surface complexation reactions, it has been postulated that Fe additions have the potential to work as an effective sorbent in shooting range soil systems (Dzombak et al., 1990; Belzile et al., 2001; Leuz et al., 2006b). Remediation strategies designed for small arms ranges should ideally immobilize both Pb and Sb, which can be challenging due to differences in mobility with pH among their respective mobile species (Jardine et al., 2007; Mitsunobu, et al., 2010ab; Griggs et al., 2011; Okkenhaug, et al., 2013; Sanderson et al., 2013; Ogawa et al., 2015; Okkenhaug, et al., 2016).



Figure 2. Field site location (Ft. Greely, AK) and images of field site construction and loading.

Twelve test berms were constructed from four different types of soil: silt loam, loamy sand, sandy loam and sand and each cover an area approximately 2 square meters. The silt loam end member was sourced locally from DTA and the sand end member was purchased from Delta Sand and Gravel. The soil end members were mixed by Delta Sand and Gravel in a large soil

mixer and construction began in August 2010 in conjunction with Cold Regions Test Center (CRTC) on the Texas Range of DTA. During the construction each soil material was piled onto a water-proof geoliner and the sides of the liner were rolled tightly and leveled to direct water flow towards a bucket lysimeter to collect berm surface water runoff (**Figure 3**). Soil moisture and temperature probes were installed into a subset of berms of each soil type and were installed 180 degrees away from bullet pocket and 1 m up from the ground at a depth of 0.5 m into the berm (**Appendix A, Figure A1**). Data loggers for soil/air temperature and soil moisture (Onset HOBO Data Loggers, Bourne, MA) were logged every hour for 5 years and downloaded twice per year. There were periodic breaks in data collection primarily due to equipment failure or to animals chewing/destroying the logger cords.

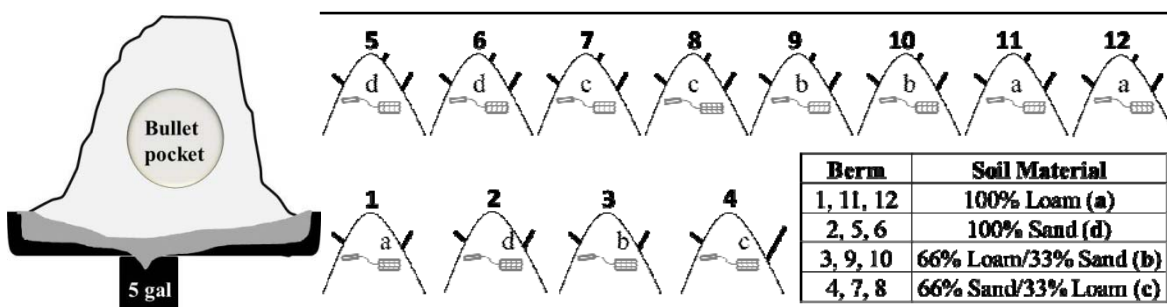


Figure 3. Schematic showing layout of the berms. Berms 1-4 are “pristine” and berms 5-12 are “contaminated”.

Of the twelve separate berms and four soil types, four berms are classified as ‘pristine’ with no metals addition. The other 8 berms (duplicates of each soil type) were fired into in a controlled firing event in September 2010 and are classified as the ‘contaminated’ berms. The firing event was facilitated by CRTC and Alaska Army National Guard Ft. Greely MP Company, 49th Missile Defense Battalion. We fired 2,000 military-issued 5.56 mm bullets into each of the 8 contaminated berms. The typical alloyed bullet slug were composed of about 99% Pb with 1% Sb (31.7 g Pb and 0.3 g Sb), and lesser amounts of Cu, Ni, Zn and other metal(loid)s (**Appendix A, Table A1**). We used military issue M4 rifles and fired bullets into the center of the berms in what is termed the ‘bullet pocket’. In August 2014, an Fe amendment was added to a subset of the contaminated berms, 5, 7, 9 and 11 (one of each of the soil types) in order the investigate the effectiveness of Fe as a treatment for limiting Pb and Sb mobility. The Fe amendment was added as a solution made up by adding 40 g of Fe(II) in the form of FeCl₂ (Alfa Aesar, 99.5% metals basis powder, Haverhill, MA) to 15 liters of drinking water (Fairbanks, AK) in a pre-washed 15 L capacity fertilizer sprayer pump (Echo, MS-401) and manually mixed. In another 15 L sprayer, we added 75 g of CaCO₃ (Powder, J.T. Baker, Center Valley, PA) to 15 liters of drinking water and manually mixed. We sprayed the two mixtures independently, but in tandem, to each of the selected berms.

Each berm was sampled 1-16 times for aqueous metal concentrations and 1-2 times for solid phase metal distribution and speciation, on average per year. The pristine berms were routinely

monitored for background concentrations of metals, approximately 1-4 sample collections per summer.

The loamy soil, when compared to the sand, has higher surface area, higher organic content and a lower pH (**Table 1**). For the field project, we constructed berms from these sand and loam end members, as well as mixtures of the two, in order to create a gradient of soil physicochemical characteristics (e.g. pH, organic matter content) along which we could monitor distinct differences in metal speciation and mobility. Soil 1 is pure silt loam, soil 2 is pure sand, soil 3 is a mixture of 2/3 loam and 1/3 sand, and soil 4 is a mixture of 2/3 sand and 1/3 loam. Major mineral phases in common between the soil types are quartz (SiO_2) and plagioclase $(\text{Na,Ca})(\text{Si,Al})_4\text{O}_8$. Chlorite $(\text{Mg,Fe,Li})_6\text{AlSi}_3\text{O}_{10}(\text{OH})_8$ and mica/illite $(\text{KAl}_3\text{Si}_3\text{O}_{10}(\text{OH})_2$ were found exclusively in silt loam-containing soils.

		Soil type 1 (\pm)		Soil type 2 (\pm)		Soil type 3 (\pm)		Soil type 4 (\pm)	
<u>Soil Classification</u>		<i>Silt Loam</i>		<i>Sand</i>		<i>Loamy sand</i>		<i>Sandy loam</i>	
<u>Soil Texture</u>									
	% sand	26	0.8	96	2.9	52	1.6	74	2.2
	% silt	71	2.1	2.0	1.0	46	1.4	24	0.7
	% clay	3.0	1.0	2.0	1.0	2.0	0.1	2.0	0.1
	surface area (m^2/g)	5.2	0.10	1.9	0.10	3.8	0.10	3.7	0.10
<u>Chemical Characteristics</u>									
	soil pH	5.3	0.27	8.4	0.42	5.7	0.28	6.8	0.34
	Organic matter % (L.O.I.)	3.8	/	0.1	/	3.2	/	1.3	/
	Non-purgeable organic carbon (ppm)	12	/	3.0	/	16	/	12	/
<u>Chemical Quantification</u>									
	Al_2O_3 (%)	15.0	0.0100	13.6	0.0100	14.8	0.0100	14.8	0.0100
	CaO (%)	1.73	0.0100	2.41	0.0100	1.99	0.0100	2.11	0.0100
	Fe_2O_3 (%)	5.73	0.0100	5.98	0.0100	5.95	0.0100	5.95	0.0100
	SiO_2 (%)	58.9	0.0200	62.1	0.0200	56.3	0.0200	56.0	0.0200
	As (mg/kg)	15.8	1.83	18.2	1.92	20.1	1.82	21.0	1.84
	Ba (mg/kg)	831	3.28	779	3.35	808	3.25	831	3.29
	Cu (mg/kg)	26.5	0.527	54.3	0.602	29.6	0.533	32.2	0.541
	Mn (mg/kg)	599	3.00	1020	3.84	686	3.14	689	3.16
	Ni (mg/kg)	34.2	0.530	38.3	0.573	36.2	0.538	36.9	0.546
	Pb (mg/kg)	19.5	0.666	30.0	0.724	25.4	0.678	20.4	0.668
	Sb (mg/kg)	bld	/	6.37	1.57	6.29	1.52	6.56	1.52
	Sn (mg/kg)	8.30	1.06	13.4	1.11	8.30	1.06	7.87	1.06
	Sr (mg/kg)	193	0.296	204	0.313	203	0.301	202	0.302
	TiO_2 (mg/kg)	9650	7.22	10700	7.87	9630	7.19	9620	7.22
	W (mg/kg)	6.30	1.20	6.60	1.28	5.48	1.21	6.74	1.21
	Zn (mg/kg)	69.3	0.372	101	0.418	72.7	0.375	74.0	0.377
<u>Background Aqueous Conc.</u>									
	Sb ($\mu\text{g/L}$)	2.0	0.10	2.4	0.10	1.1	0.10	1.4	0.10
	Pb ($\mu\text{g/L}$)	bld	/	bld	/	bld	/	bld	/

^{1/} = error not quantified

Table 1. Characterization of soils used in construction of the field site impact berms.

The concentrations of metals found in the shooting range berms following the loading event are provided in **Table 2**. The Pb and Sb values are consistent with previously observed values in shooting range soils. From these values it is clear that Pb is the primary soil contaminant, with Sb and other metals roughly 20-50 times lower concentrations. We also note the discrepancy in

the values between the soil types, with the highest metal(loid) concentrations found in the sand soil; this is likely due to the fact that bullet fragmentation was greatest in the sand relative to the loam, and during analysis large bullet fragments were excluded (soils were saved to <75 µm prior to analysis).

Berm	Soil type	Status	Pb (mg/kg)	+/-	Sb (mg/kg)	+/-	Cu (mg/kg)	+/-	Ni (mg/kg)	+/-	Sn (mg/kg)	+/-	Zn (mg/kg)	+/-
1	Silt loam	Pristine	19.5	0.666	bld	/	26.5	0.527	34.2	0.530	8.30	1.06	69.3	0.372
2	Sand	Pristine	30.0	0.724	6.37	1.57	54.3	0.602	38.3	0.573	13.4	1.11	101	0.418
3	Loamy sand	Pristine	25.4	0.678	6.29	1.52	29.6	0.533	36.2	0.538	8.30	1.06	72.7	0.375
4	Sandy loam	Pristine	20.4	0.668	6.56	1.52	32.2	0.541	36.9	0.546	7.87	1.06	74.0	0.377
5	Sand (a)	Fired	14500	7.83	281	2.21	658	1.35	36.5	0.645	74.8	1.39	172	0.555
6	Sand (b)	Fired	16400	8.36	275	2.21	733	1.42	34.8	0.647	75.1	1.40	172	0.566
7	Sandy loam (a)	Fired	1680	2.46	42.5	1.61	132	0.700	37.5	0.562	17.4	1.10	88.8	0.405
8	Sandy loam (b)	Fired	2810	3.22	61.8	1.66	215	0.809	37.6	0.565	19.1	1.12	99.2	0.421
9	Loamy sand (a)	Fired	1260	2.12	25.7	1.57	129	0.687	36.2	0.552	11.4	1.08	88.0	0.400
10	Loamy sand (b)	Fired	1680	2.49	32.5	1.60	165	0.739	36.8	0.556	14.3	1.10	94.8	0.409
11	Silt loam (a)	Fired	301	1.17	9.56	1.53	50.0	0.568	34.0	0.532	8.24	1.06	69.1	0.375
12	Silt loam (b)	Fired	459	1.39	12.0	1.53	62.8	0.590	34.1	0.533	10.3	1.06	71.7	0.380
		LLD	2.47		5.91		1.28		1.30		3.43		1.07	

Table 2. Total metal concentrations in the 12 test berms analyzed by x-ray fluorescence (XRF). Pristine soil concentrations shown for comparison. LLD = lower limit of detection.

4.2 Mobile Pb and Sb concentrations and speciation in berm runoff

A key part to understanding metal transport at shooting ranges is not only quantifying the amount of contaminants being dispersed from bullet fragments as a result of interactions with the atmosphere and pore water flow, but also determining the speciation of the mobile species. The EPA maximum contaminant level standards for drinking water are 6 µg L⁻¹ and 15 µg L⁻¹ for Sb and Pb respectively (U.S. EPA, 2009). Metallic Pb and Sb deposited in soils tend to be highly mobile, with mobility potentially increasing with time due to progressive weathering and transformation of the metals to soluble secondary products. Therefore, temporal monitoring of Pb and Sb concentrations in the berm runoff reflects the solid phase speciation and temporal extent of metals weathering. Furthermore, characterization the speciation of dissolved metal(loids) (e.g. Sb oxidation state) is essential to understanding the specific soil (bio)geochemical conditions controlling weathering and mobility pathways and potential bioavailability. Lead exists predominately in a +2 oxidation state in dissolved form, and Sb is typically found in either +3 or +5 oxidation state. The reduced form of Sb, Sb(III), is believed to be more toxic than Sb(V), while Sb(V) is a relatively more mobile species (Andreae et al., 1981; Bencze, 1994; Gurnani et al., 1994).

The average values of Pb and Sb in the berm runoff are given in **Figure 4**. The total dissolved concentrations of Sb and Pb were determined by inductively coupled plasma-mass spectrometer (ICP-MS) using an Agilent 7500ce (Agilent Technologies, Santa Clara, CA) following the general procedure outlined in Creed et al. (1994). Statistically significant differences (p <0.05) in the distributions are indicated with lettered levels; levels not connected by the same letter are considered to be significantly different.

These results show that there is very little variation in the aqueous concentrations of Pb among the soil types (with slight increases in the sandy loam and loamy sand), with the average concentration at about 20 $\mu\text{g/L}$. Interestingly we observe that the average Sb concentrations are elevated with respect to Pb, with average values exceeding 100 $\mu\text{g/L}$. We also observe significant variation in the Sb concentrations among the soil types. These observations suggest that Sb is significantly more mobile than Pb (with roughly 50 times lower soil concentration the Sb is elevated in solution by a factor of 4 or 5), and shows a general trend for higher dissolved concentrations in soils with greater sand content (and higher pH).

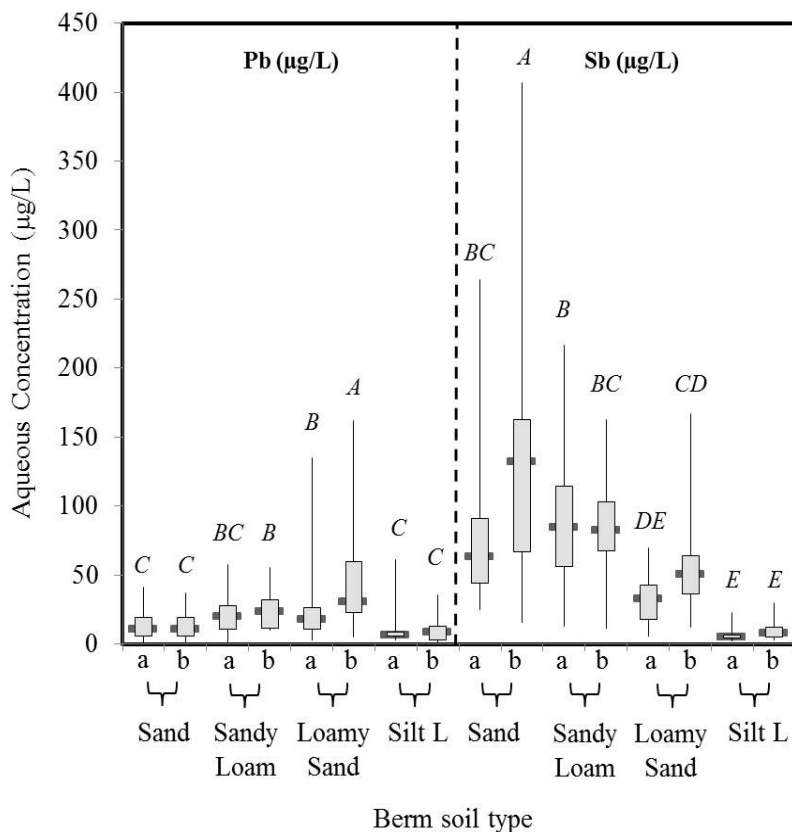


Figure 4. Box plot diagram of total Pb (left half) and Sb (right half) concentrations from 2011 to 2014 (prior to Fe addition) as a function of soil type (sand, sandy loam, loamy sand and silt loam) for the duplicate contaminated test berms (a) refers to berms 5, 7, 9, 11 and (b) refers to berms 6, 8, 10, 12. Gray lines indicate median values during the 4 years. The gray boxes depict the lower (25th percentile) and upper (75th percentile) quartiles. A, B, C, D, E indicates levels that are statistically different at $p < 0.05$. Levels are not comparable between Pb and Sb. Samples were filtered to 0.45- μm , acidified with ultra-pure HNO_3 and analyzed using ICP-MS. Samples were analyzed in triplicate, calibrated to known standards and error values are within 5%.

The speciation of mobile Sb species was investigated for the soil types of the test berms for years 1-2, results are shown in **Figure 5**. Analysis of the sand and sandy loam berm runoff in 2011 showed the sole presence of Sb(V). There is detectable Sb(III) in the loamy sand runoff of one of the duplicate sets of berms and was quantified to be 35 $\mu\text{g/L}$ Sb(III). This is the only observation of Sb(III) in the runoff during the 5 year monitoring, in the high loam content berms after less than 1 year of weathering. All other Sb samples tested were found to be fully oxidized. The silt loam-draining berms were not quantified for Sb speciation due to the overall low sample volume collected from the berm runoff and the low concentrations of total Sb, however, we expect similar behavior in that Sb(III) is the initial aqueous oxidation product. The Sb(III) species identified in water from the loamy berms in 2011, was most likely stabilized via complexation with soil organic matter (SOM) (Filella et al., 2002b; Ceriotti and Amarasinga, 2009).

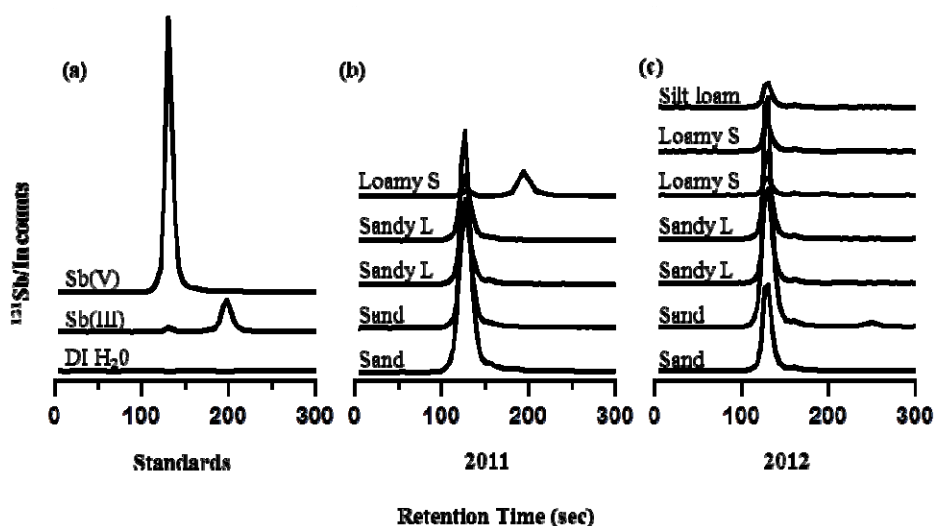


Figure 5. The oxidation state of Sb in aqueous samples determined using liquid chromatography coupled to an ICP-MS. (a) standards (100 $\mu\text{g/L}$ Sb(III) and Sb(V)) and berm water runoff collected (b) summer 2011 and (c) summer 2012.

However, at the beginning of summer 2 (2012) we analyzed the test berms again, but found only fully oxidized Sb for all soil types. Oxidation of Sb was expected to be fast, as determined by Ilgen et al., 2014, and sequential oxidation is rarely observed in shooting range berms due to the lack of Sb(III) stability in oxidizing soil conditions and the usually long reaction time shooting range berms have before analysis.

Both Sb(III) and Sb(V) species have been shown to become immobilized via sorption reactions with oxidized iron/manganese (hydr)oxides (Fe/MnO-OHs), due primarily to amphoteric dissociation of the hydroxyl group on the surfaces of these oxides providing effective binding sites (Zimdahl et al., 1977; Thanabalasingam and Pickering, 1990; Belzile et al., 2001). The presence of such reactive surfaces in soil plays an important role in controlling the transport of dissolved trace metals and metalloids (Trainor et al., 2004). Antimony in the +5 oxidation state

primarily exists in aqueous media at environmentally relevant pH ranges as the $\text{Sb}(\text{OH})_6^-$, negatively charged oxyanion; its sorptive behavior is typical of oxyanions in that it partitions most strongly to oxide surfaces at low pH. Aqueous $\text{Sb}(\text{III})^0$ predominately exists as neutral $\text{Sb}(\text{OH})_3^0$ complex, therefore the adsorption is not affected by the charge on the adsorbate surface (Thanabalasingam and Pickering, 1990; Allison et al., 1991; Vink, 1996; Belzile et al., 2001). Our solution data shows the trend of lower dissolved Sb concentrations in the loamy soil, which has lower pH and greater proportion of organic matter that may serve as affective binding sites for Sb. To summarize aqueous Sb trends in our berms thus far; loamy material exhibits lower concentrations of dissolved Sb, with the potential to stabilize the +3 oxidation state at the initial reaction times, whereas sand exhibits much higher concentrations of the more mobile $\text{Sb}(\text{V})$.

As discussed below our results suggest that in all soils the release of $\text{Pb}(\text{II})$ species into solution is controlled by the dissolution of PbO or PbCO_3 weathering products, consistent with previous results (SAAMI, 1996). Solubility of these solid species has a minimum at neutral to slightly alkaline pH values (Allison et al., 1991).

The box plots in **Figure 6** show concentrations of Pb as a function of sampling season and the Fe-amendment versus control (August 22, 2016 to end of sampling 2015). Similar data are shown in **Figure 7** for Sb. For Pb, there is a greater variability from year to year with increasing sand proportions. While there were spikes in concentrations for the silt loam draining berms, overall the majority of the data and the means were not significantly different over the course of

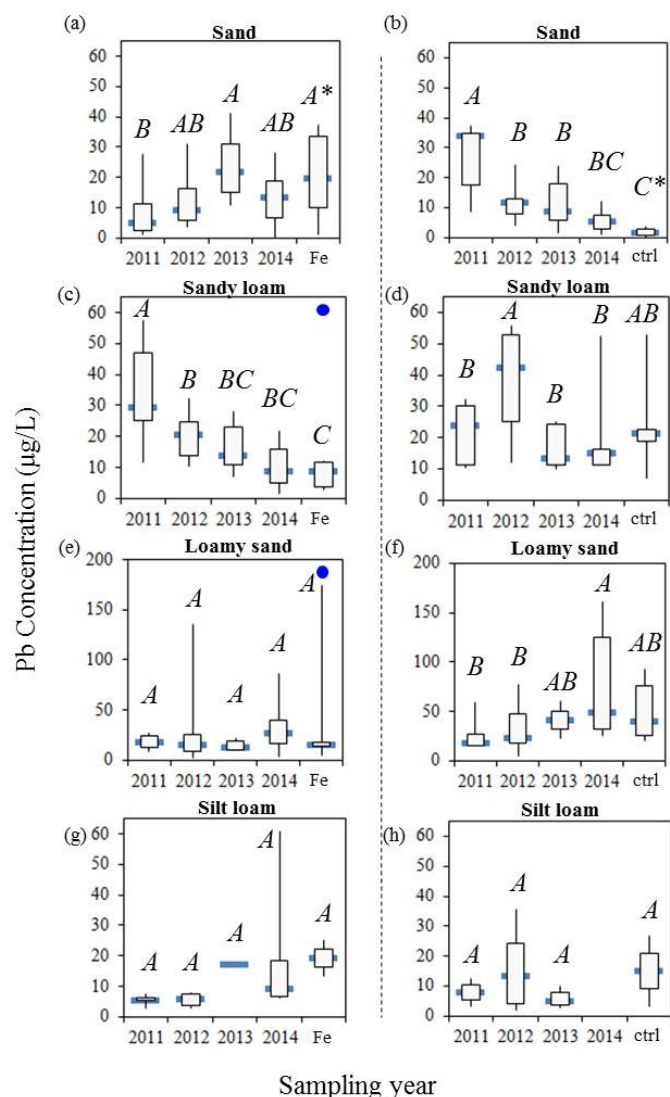


Figure 6. Pb concentrations in berm runoff as a function of soil type for the duplicate berms (a) 5, (b) 6, (c) 7, (d) 8 (e) 9, (f) 10, (g) 11 and (h) 12. ‘Fe’ indicates amended berms and ‘ctrl’ indicates un-amended berms. A, B, C indicate levels that are statistically different at $p < 0.05$, but are not comparable between duplicate soil types. ‘*’ signifies statistical differences between Pb distributions between the Fe versus control berm runoff.

5 years. For Sb, sand soil runoff did not show significant variability between years. Similar to Pb, the silt loam runoff contained generally low concentrations of Sb and showed little variability over the course of 5 years, except for 2012 to 2013 in Berm 12 (Figure 15h). These results suggest that the Pb and Sb reach steady-state concentrations relatively quickly (during the first season of oxidation), but the higher variability (at least for Pb) in the sandy soils suggest some relationship to hydrologic conductivity.

The $\text{FeCl}_2/\text{CaCO}_3$ amendment was added to a subset of the berms (5, 7, 9, and 11) at the end of summer 2014 in order to study Pb and Sb retention, results are shown for Pb in **Figure 6** in comparison to the control berms that were not amended and for Sb in **Figure 7** in comparison to the control berms that were not amended. The Fe amendment had little effect on Pb immobilization in berm soil runoff, except in the sand draining soils where Pb distributions were significantly lower in the control sand berm (un-amended) than the Fe amended berm (**Figure 6**). The Fe versus ‘ctrl’ distributions are marked (*) if distributions are significantly different at $p < 0.05$. For the remainder of the berms, the runoff was not significantly different at $p < 0.05$ comparing the amended and un-amended berms. Antimony, however, behaves much differently than Pb after the Fe addition and is significantly immobilized in all the soil types except the silt loam (**Figure 7**), where concentrations of Sb were already low. In addition, the silt loam Berm 11 contained little runoff during 2015 and sampling was limited.

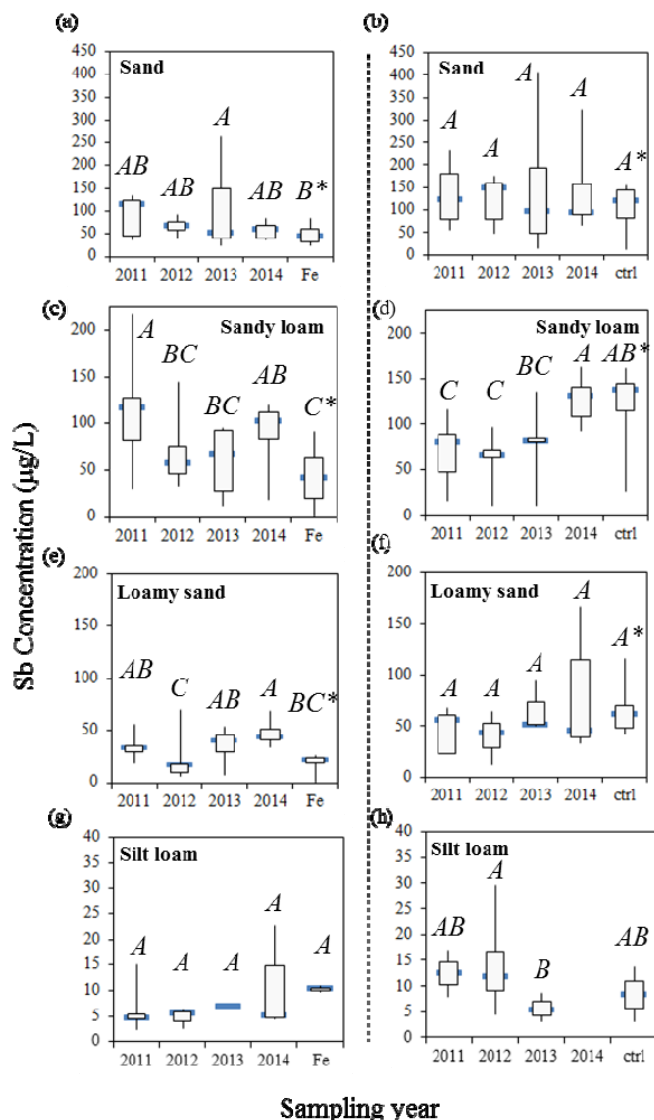


Figure 7. Sb concentrations in berm runoff as a function of soil type for the duplicate berms (a) 5, (b) 6, (c) 7, (d) 8 (e) 9, (f) 10, (g) 11 and (h) 12. ‘Fe’ indicates amended berms and ‘ctrl’ indicates un-amended berms. A, B, C indicate levels that are statistically different at $p < 0.05$, but are not comparable between duplicate soil types. ‘*’ signifies statistical differences between Sb distributions between the Fe versus control berm runoff.

4.3 Localized solid phase Sb and Pb speciation in berm soils

A key aspect of understanding the reaction pathways controlling Pb and Sb behavior in the range soils is to identify and characterize the solid phase weathering products, that in turn control the release of metal(loid)s to solution. The speciation of Sb in the soil fraction was investigated for all test berm soil types as a function of time using x-ray fluorescence (XRF) mapping and Sb L_{III}-edge μ -XANES spot analysis (**Figure 8**). Corresponding linear combination fitting (LCF) results are provided in **Appendix A Table A2**. Zero-valent Sb occurred within the bullet core and Sb(V) occurred in the soil fraction in the silt loam soil type, adjacent to the bullet core. The normalized absorption edge energies (**Figure 8**) show differences between the zerovalent Sb absorption (4132.0 eV), trivalent Sb oxide absorption (4133.4 eV) and pentavalent Sb oxide absorption (4143.1 eV). Spectra were compared to a variety of Sb(III) and Sb(V) compounds with metallic Sb and Sb₂O₅ contributing to the best fit. Only spectra from the silt loam-soil sample are shown due to the higher Sb content in the soil. The sandy soils have Sb content within the soil matrix that is too low a concentration for speciation analysis. These results are consistent with the observation that Sb is retained within the loam matrix (via sorption) and is more mobile in the (higher pH and higher permeability) sand matrix. These results are also consistent with the observation that Sb(V) is the dominant form resulting from bullet weathering/oxidation.

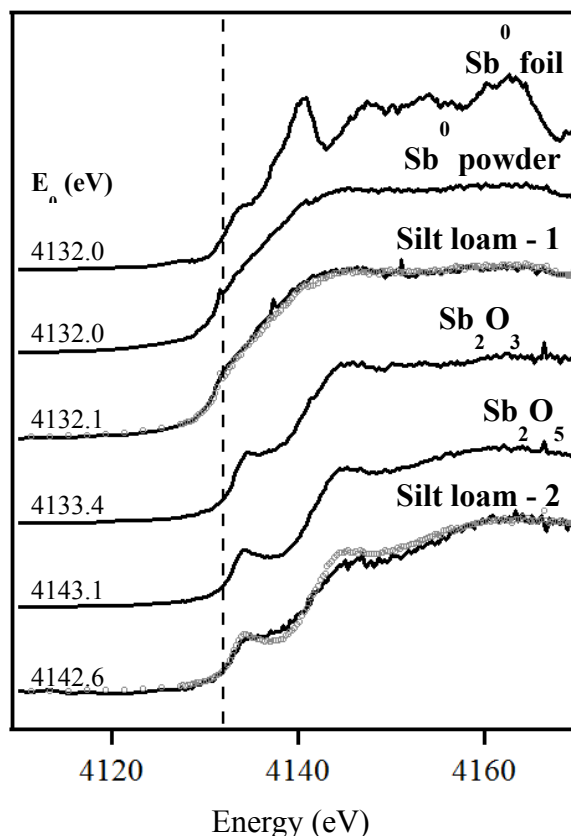


Figure 8. Normalized Sb-L_{III} μ -XANES spectra for the silt loam berm 12 soil end member. Sample data is in black lines with corresponding LCF plotted in gray circles. Standards are black lines without any overlying gray circles. Dotted line corresponds to the absorption edge for Sb-L_{III} (4132.0 eV).

Lead speciation was investigated for all test berm soil types as a function of time using XRF and Pb L_{III}-edge μ -XANES spot analysis. Overall, 90 samples were analyzed from the four types of soil as a function of year from 2011 to 2014. A subset of these are shown in **Figure 9** with LCF parameters presented in the **Appendix A Table A3**. The Pb speciation in the soil fractions was found to consist primarily of metallic Pb, litharge (PbO), cerussite (PbCO₃), hydrocerussite ((Pb₃(CO₃)₂(OH)₂) and Pb(II) sorbed to Fe(III)-oxides.

Fragmentation of bullets upon impacting a soil often resulting in highly heterogeneous distributions of metals. Lead and Fe distribution are shown for samples collected after two years of weathering in **Figure 10**. Metallic Pb was detected in each soil type throughout the sampling years and remained a large fraction of the total Pb in the samples. In addition to metallic Pb, the primary Pb products were litharge, cerussite and hydrocerussite for the first two summer seasons (2011-2012). These species occurred primarily as a crust around the Pb alloy or present as Pb hotspots throughout the soil (**Figure 10**). After two years, the presence of Pb sorbed species was detected and the best fits of many soil samples included contributions of Pb(II) sorbed to Fe(III) oxides. While the majority of the spots for years 3 and 4 include contributions from sorbed species, there are also spots that are characterized differently. There are distributions that only contain metallic Pb and are either part of the bulk metal alloy or present in small ($\sim 1\text{-}50\text{ }\mu\text{m}$) highly concentrated globular areas, similar to the initial weathering samples. This highlights the heterogeneity of bullet samples and emphasizes the fact that metal release from the weathering of bullets is discontinuous. After four years reaction time, there is still a large percentage of metallic Pb present, but major Pb phases consists largely of litharge, cerussite, hydrocerussite and Pb(II) sorbed.

The results of our field study directly address several hypothesis of the the overall project. We have shown that Sb and Pb oxidation and mobilization is rapid - within the first several months after metals deposition. We also observe that Sb, while only about 1wt% of the bullet, had significantly higher dissolved concentrations than Pb, indicating a much greater mobility. This was particularly true in the soils with a greater sand fraction (and higher pH). We also observe that Sb is predominantly observed as Sb(V), although a minor amount of Sb(III) was observed at initial weathering stages in the loam soil. The relatively constant concentrations of Pb among the soil types indicate that it is likely controlled to a large extent

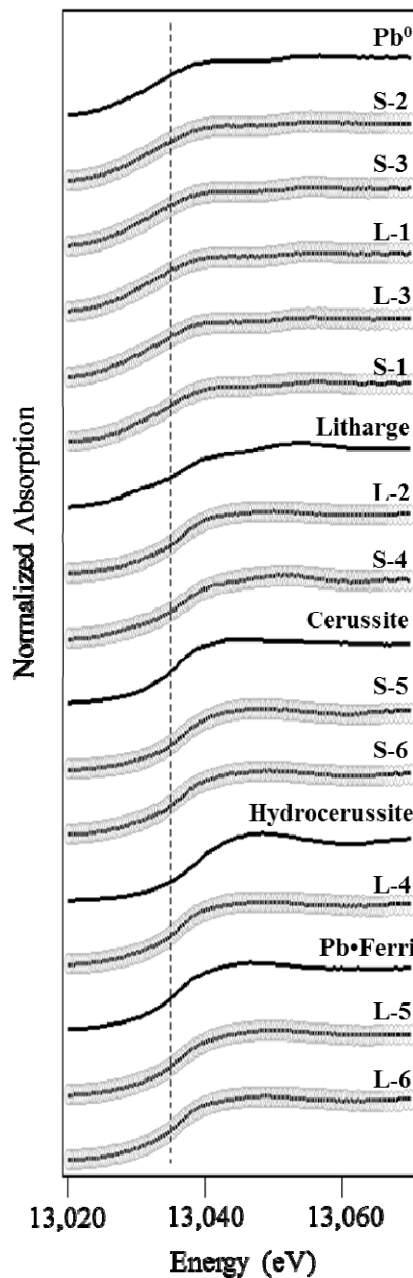


Figure 9. Normalized Pb-L_{III} μ -XANES for the end member test berms (5, 12) over 4 years. Sample data is in black lines with corresponding LCF plotted in gray circles. Standards are in black with no fits present. Pb•Ferri corresponds to Pb sorption product with synthesized Fe(III) oxides.

by solubility of the secondary phases, which we observe to be litharge, cerussite, and hydrocerussite. However, over time we also observe an increasing fraction of “sorbed” Pb within the soil matrix, indicating sorption processes are an important factor controlling mobility. Sorbed Sb was only significant in the higher surface area loamy soils. We also observed that our amendment procedure, using $\text{FeCl}_2/\text{CaCO}_3$, led to an increase in the retention of Sb likely through the sorption of Sb to Fe(III)-oxides. However, we saw little effect of the amendment on the Pb(II) concentrations. Several key questions that result from the field studies include (i) what are the controls on initial oxidation/weathering of Sb (ie short term kinetics) and relationship with observation of Sb(III) at short time scales, (ii) what are the molecular controls (e.g. via sorption) on Pb and Sb once released into the soil column and (iii) what are the long term fates of metals in shooting range soils. We address this last point in the following section where we investigate Pb and Sb speciation in berm soils that have been weathering for 15+ years under the same conditions (soil type and climate) at our test berm site.

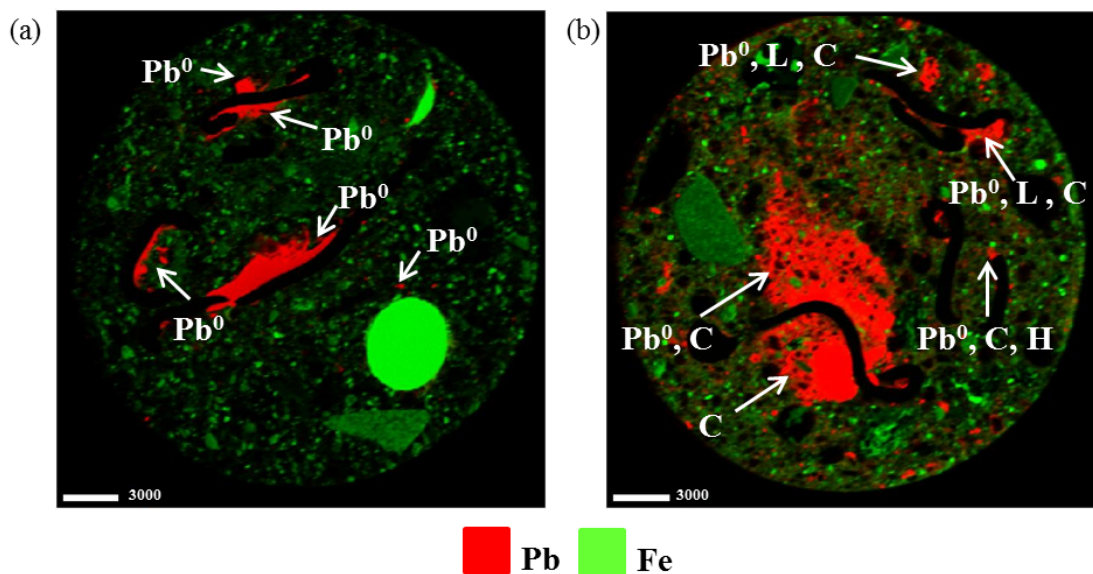


Figure 10. XRF maps showing distributions of Pb (red) and Fe (green) in thin sections collected from the (a) sand and (b) sandy loam test berms in the summer of 2012. Thin section area is 25x25 mm and scale bar units are in μm . Pb^0 = metallic Pb, L = litharge, C = cerussite, H = hydrocerussite.

4.4 Sb and Pb speciation in a historic shooting range berm

Soil samples and bullet fragments were obtained from a hillside used as a natural berm-style backdrop at the Meadows Range Donnelly Training Area, Fort Greely, Alaska. While no longer active, the Meadows Range was heavily used for small arms training exercises approximately 15-20 years ago. Multiple types of ammunition rounds were fired into the berm including .50 caliber, 7.62 mm and 5.56 mm bullets. The 5.56 mm rounds were the only size examined in this study. The bullet alloy is composed of 99 wt. % Pb and 1 wt. % Sb (DAC, 2010). The silty loam soil is the same as that used as the loam end-member in the construction of the test berms as described above. Bulk concentrations of Pb (77.91 mg/kg) in this historic range soil are almost an order of magnitude higher than Sb (8.43 mg/kg) as determined by X-ray fluorescence.

Elemental distribution and semi-quantitative analysis were conducted on a JEOL JXA-8530F field emission electron microprobe in both wavelength-dispersive (WDS) and energy-dispersive (EDS) mode. Samples were analyzed for Sb elemental distribution, spatial correlation and speciation using synchrotron-based x-ray spectroscopy. Extended x-ray absorption fine structure (EXAFS) data was collected at beamline sector 13 IDE (GSECARS), Advanced Photon Source (APS), Argonne National Laboratory.

Electron microprobe analyses were conducted on an intact, unfired, military-issued 0.22 caliber (5.56 mm) bullet in order to characterize the initial composition prior to weathering and alteration, shown in **Figure 11**. The pristine bullet consists of four distinct chemical zones of varying thickness. The outermost layer consists mainly of Fe, approximately 500 – 1500 μm thick, and surrounds a Cu-rich interlayer, approximately 50 – 100 μm thick. A discontinuous Pb-rich interlayer (50 – 150 μm thick) exists between the Cu-rich interlayer and the slug (500 – 4000 μm thick), the innermost region of the bullet. Electron microprobe analyses revealed that the distribution of Pb and Sb within the bullet is heterogeneous. Lead is the main component in the matrix but occurs in different proportions with Sb in the matrix of the slug (87 and 13 mol%, respectively) than in the Pb-rich interlayer (96 and 4 mol%, respectively), making these two regions chemically distinct. Lead also occurs as discrete $\sim 2 \times 2 \mu\text{m}$, ~ 100 mol% spheres, which form as a result of melting during analyses conducted at high beam currents ($\geq 100\text{nA}$) and are thus an artifact of the analytical method.

Antimony is relatively evenly distributed within the matrix of the slug (**Figure 11**), except that it occurs as diffuse, discrete, roughly circular Sb-rich spherical ‘hotspots’ (40 mol% Sb). The hotspots are $\sim 2\text{-}5 \mu\text{m}$ in diameter and are embedded within the Pb-matrix and not specifically associated with Pb spheres that are an artifact of melting during analysis. The Sb-rich hotspots are more common within the Pb-rich interlayer, where they have a higher Sb content (88 mol % Sb) and contain the majority of the Sb present. When averaged across the entire area of the Pb-rich interlayer, Sb is present at a level of 4 mol% Sb.

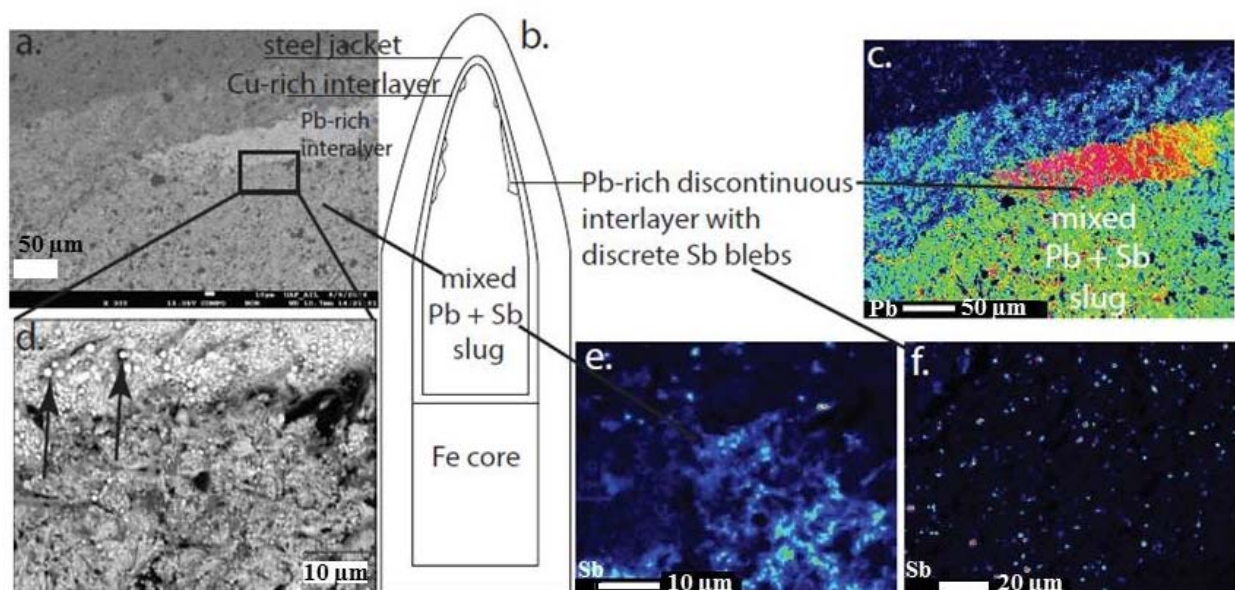


Figure 11. Composition of an unweathered 5.56 mm bullet. (a) Back scatter electron image showing chemically distinct zones. (b) Schematic depiction of bullet anatomy. (c) WDS elemental map showing heterogeneous distribution of Pb. (d) Metallic Pb spheres designated by arrows are the result of melting during analyses at high beam current ($\geq 100\text{nA}$). (e) WDS elemental map showing that Sb is relatively well-mixed within Pb in the slug but exists mainly as discrete hotspots (2-5 μm) within the (f) Pb-rich interlayer.

An example of X-ray fluorescence maps collected on a spent bullet that had weathered for approximately 15 years is shown in **Figure 12**. The steel and Cu jacket partially separated from one another, leaving the Pb/Sb slug exposed. While Pb comprises the bulk of the alloyed core, there are also particles of Pb present within the soil matrix. The back-scattered electron image of Region 1 (outlined in white box in **Figure 12**) depicts the interface of the bullet with soil particles (**Figure 13**). Soil minerals are present within the fracture that passes through the slug and Pb-rich interlayer of the bullet. The tip of the fracture has little exposure to soil while at the base of the fracture, soil grains are the predominant material. As a result, we identified three different areas within a single region of the sample that experienced differing degrees of exposure to soil and exhibited different degrees of weathering and alteration.

The Pb and Sb distribution in the area at the tip of the fracture (**Figure 13A**) is similar to that seen in the pristine bullet. The Sb-rich hotspots in this region have WDS totals equal to 100% with contributions from only Sb and Pb, indicative of the metals being present in their elemental form. The axis of the fracture becomes progressively more soil rich until eventually, in areas of the sample further from the bullet, fragments of slug material are completely incased in soil material such as seen in **Figure 13C**. As the abundance of soil particles increases, there is a

corresponding decrease in the relative abundance of Pb and Sb, as illustrated in the wavelength dispersive spectroscopy (WDS) elemental maps, suggesting progressive weathering occurs along the axis of the fracture.

The weathering crust and bullet-soil interface is primarily comprised of Pb, whereas Sb is present in segregated clusters (**Figure 13**). Back scatter electron imaging and chemical analyses by electron microprobe reveal the crust appears to act as a cement between the bullet fragments and surrounding soil particles as well as between individual soil particles. Similar weathering crusts have previously been observed around bullets weathering in shooting range soils (Jorgensen and Willems, 1987; Lin et al., 1995; Hardison et al., 2004; Vantelon et al., 2005; Ackermann et al., 2009). The alteration crust in the current study is discontinuous; it does not entirely surround any single bullet fragment. The distance the alteration crust extends away from the bullet fragments varies between individual fragments.

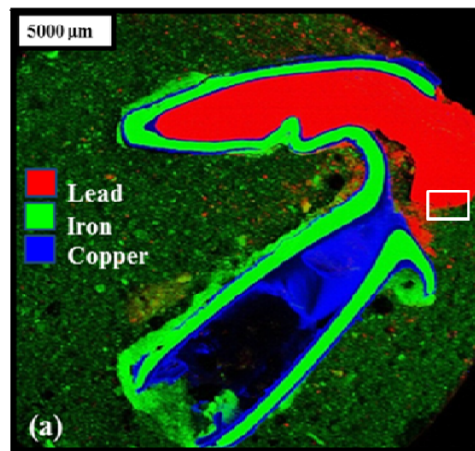


Figure 12. Metal distribution in the historic shooting range soil. Area of interest outlined in white square is Region 1.

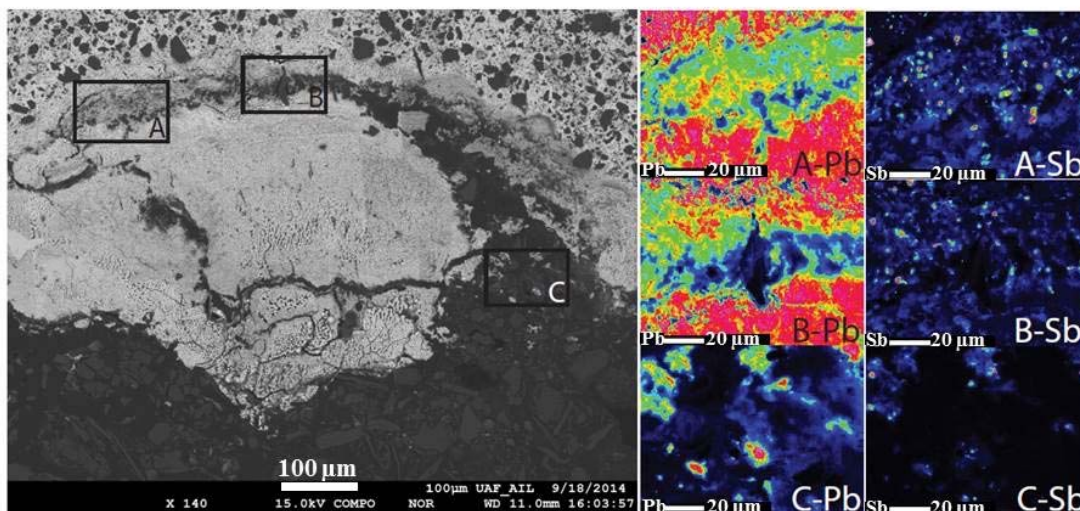


Figure 13. BSE image of Region 1 in Figure 12. The sample features a crack within the Pb-rich rim that propagates and is increasingly (left to right) filled by soil (dark particles). A,B,C represent different areas analyzed.

The change in relative Pb intensity with distance from the bullet is shown in **Figure 14**. The Pb profile represents the average Pb intensity at every pixel from the bullet-soil interface to the edge of the mapped area. To obtain this profile, an area on the sample was chosen that had relatively

linear features with respect to bullet to soil interface (**Figure 14a**). The particular pixel fulfilling the definition of the bullet-soil interface was defined in each column of image intensity data and the x coordinate of that pixel was set to be at a distance equal to 0 micrometers. After identification of the 0 μm pixel in each column, the columns were adjusted to align the pixels representing $x = 0$ micrometers. Once the data was aligned, the Pb intensities for every column of data were averaged.

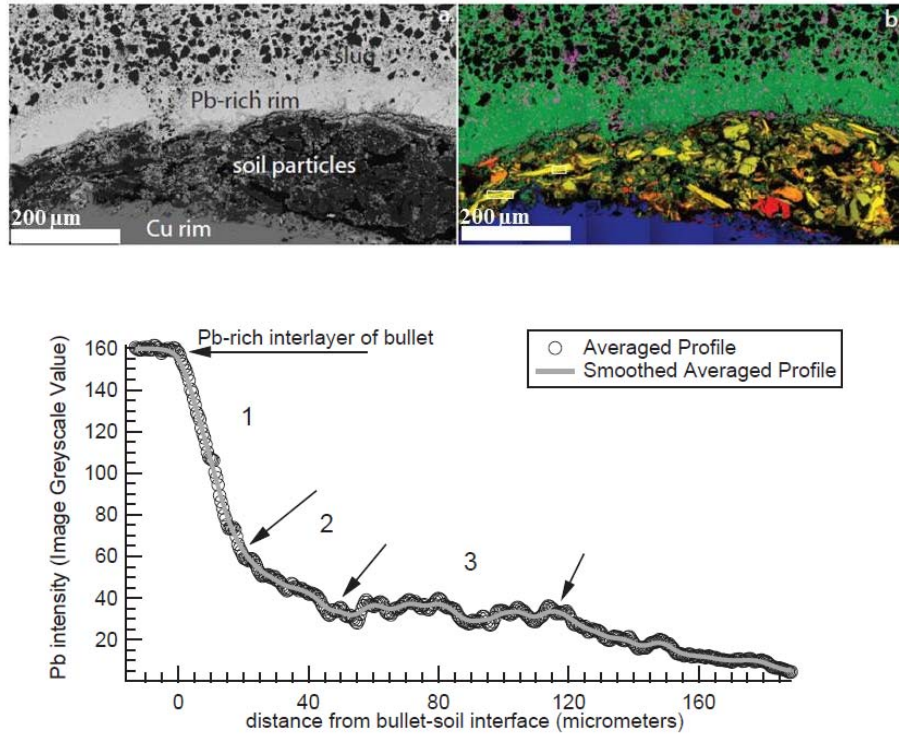


Figure 14. (a) Backscatter image showing soil particles embedded between the Cu rim and the Pb-rich interlayer of the bullet. (b) WDS map showing elemental distribution in the bullet and soil, Cu = blue, Pb = green, Al = yellow, Sb = magenta. (c) Pb intensity profile calculated using image greyscale values from the Pb distribution WDS map.

The profile in **Figure 14** shows a sharp decrease in Pb concentration (by ~60%) over the first 20 μm from the bullet-soil interface. Within this area, relatively unaltered but physically separated shards of the Pb-rich interlayer are concentrated. At a distance of 20-50 μm from the interface, the Pb intensity continues to decrease though with a shallower slope, reaching 20% of the original Pb signal at a distance of 50 μm from the bullet. The Pb intensity remains relatively constant over the distance of 50-120 μm before beginning a steady decline to 3% of the original Pb intensity at 190 μm from the bullet-soil interface. These results are similar to a previous study where the Pb concentration profile revealed a strong decrease in Pb over a distance of a few hundred micrometers from the weathering crust (Vantelon et al., 2005). The distribution of Sb is discontinuous in the bullet alloy and cemented crust, which prevents determination of a

similar concentration profile. As mentioned previously, Sb concentrations present in the soil fraction were low indicating Sb is highly mobile in the soil system.

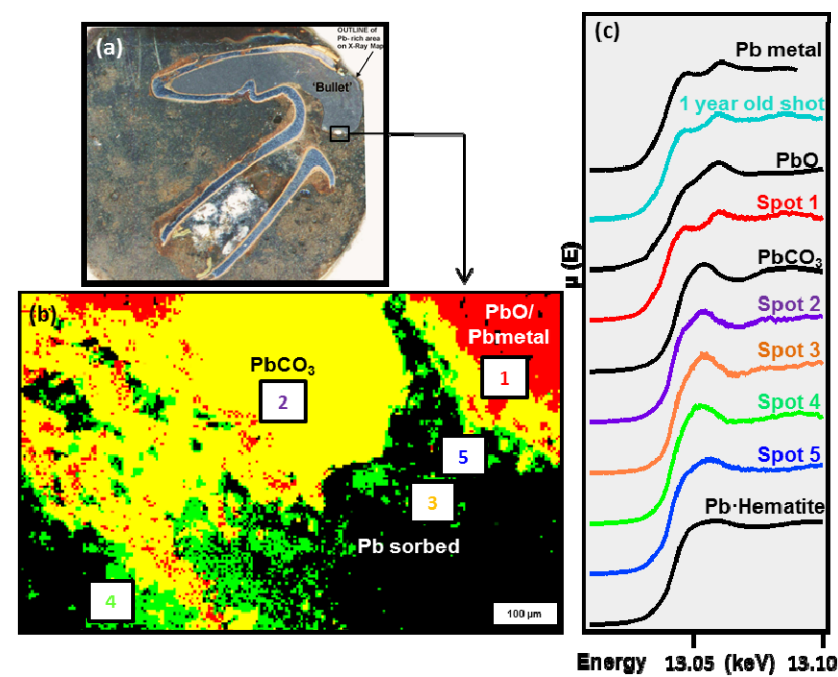


Figure 15. Lead analysis of (a) the hotspot from the historic berm sample, (b) XANES map showing principle Pb components contributing to the signal intensity, and (c) Pb-L_{III}XANES spectra from standards and model compounds (in black) and experimental data (colored). XANES data measured at Pb-L_{III} absorption edge was processed using the Microanalysis Toolkit software developed at the Stanford Synchrotron Radiation Lightsource and LCF of the data was performed using the Athena interface (Ravel and Newville, 2005) to the IFEFFIT (Newville, 2001) program.

Detailed micro-scale analysis of the Pb speciation in the weathering feature in Region 1 revealed the presence of oxidized Pb species most adjacent to the fracture, in addition to containing metallic parent material. Multiple energy mapping and principle component analysis (PCA) of Region 1 showed distinct distributions of Pb components (**Figure 15**) and representative spots (1-4) were further analyzed by XANES to determine the speciation. Linear combination fitting (LCF) of the XANES spectra in **Figure 15c** show that spot 1 is composed of cerussite (42%) with lesser amounts of litharge (32%) and hydrocerussite (28%) and correspond to the yellow principle component distribution (**Figure 15b**). Spot 2 best fit analysis corresponds to primarily metallic Pb (88%) with lesser amounts of cerussite (15%), represented by the red component distribution (**Figure 15b**). Spot 3 XANES spectra contains relatively equal contributions of litharge (52%) and cerussite (51%). Spot 4 best fit analysis corresponds to Pb(II) sorption to Fe oxides, in addition to relatively equal contributions from litharge and hydrocerussite, as denoted

by the green component distribution (**Figure 15b**). Lead speciation analysis of Region 1 suggests there are unique distributions correlated to both distance from alloyed parent material and distance from soil particles. Lead is distributed in low, relative concentrations closest to soil particles along the axis of the fracture in Region 1 (**Figure 15a**) in comparison to the higher concentrations of Pb found approximately 5-10 μm from the fracture. In addition to micro-scale speciation measurements, the weathering crust of approximately 15 bullets was scraped and consolidated into a powder sample and the bulk Pb speciation was analyzed; these results show the average crust was comprised of predominantly cerussite (54%), with lesser, relatively equal contributions of litharge (26%) and hydrocerussite (23%).

The LCF analyses suggest that dissolution of PbCO_3 on the outside of the occluded PbO , which is the initial weathering product of Pb metal in the bullet fragments, ultimately controls the solubility of Pb in the historic berms at this time (10+ years). Dispersion of dissolved Pb into the soil of the historic berm is limited by sorption onto Fe oxides present in the soil. Both of these processes (dissolution and sorption) together with their counterparts (precipitation and sorption) limit the activity of Pb(II) species in soil pore water in the historic system. In comparison, the XANES spectra recorded from a 1-year old bullet collected from the newly constructed berm comprised of 100% sand (**Figure 16**) corresponds only to metallic Pb and massicot, an orthorhombic polymorph of PbO . Similar to the thin section from the historic berm, PbO is the initial oxidation product that coats the Pb metal and thus initially controls the solubility of Pb in the sand berms after 1 year.

Antimony K-edge EXAFS analysis was carried out on four separate samples from the historic shooting range (Region 1, the consolidated weathering crust, a laboratory soil sample, and an unaltered bullet alloy) and revealed various Sb oxidation states. The absorption edge energies (**Figure 17**) range from 30,491 eV, corresponding to the unfired bullet alloy, to 30,495 eV, belonging to the consolidated weathering crust scraped from the outside of the bullet fragments. The Sb species in Region 1 exhibits intermediate edge energy at 30,492 eV. Similarly, the local, uncontaminated soil that was mixed with metallic Sb powder in the laboratory also has absorption energy of 30,492 eV. The normalized absorption for the new bullet is dampened due to self-absorption effects, as the cross-section sample was thick

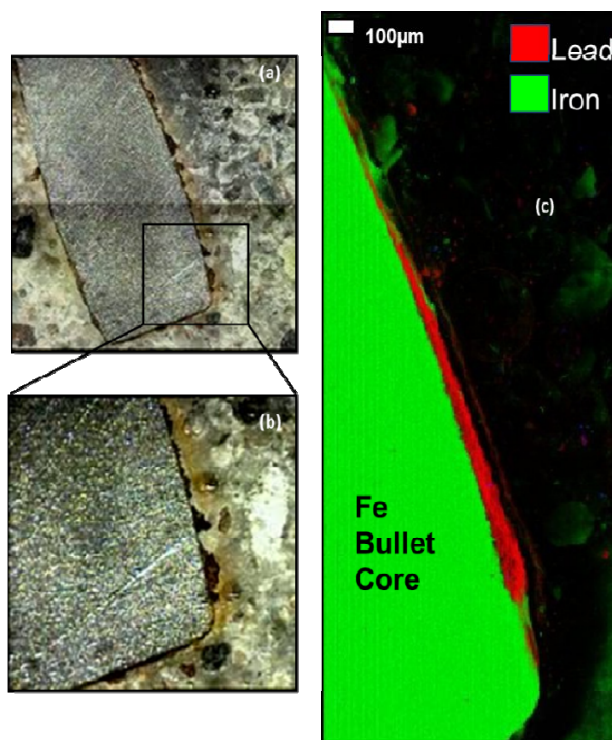


Figure 16. Thin section of a bullet collected from the pure sand newly constructed berm after 1 year of weathering: (a) and (b) Optical images, and (c) micro-focused x-ray fluorescence map of Pb and Fe.. Map was collected on BL2-3, Stanford Synchrotron Radiation Lightsource, Palo Alto, CA and optical images were collected on Leica Optical Microscope at Advanced Instrumentation Laboratory, University of Alaska Fairbanks.

(approximately 1 mm) and comprised entirely of bullet slug alloy. In addition, the two samples with intermediate edge energies (Sb soil and Region 1) also display a less pronounced normalized absorption line than the weathering crust sample and the Sb-O peaks at approximately 1.5 Å (not corrected for phase shift) in the EXAFS Fourier transform plot are much larger for the weathering crust than for the Sb soil and Region1 sample.

Shell-by-shell fitting of the backscattering features was carried out to elucidate the local structure of the Sb species most prevalent in the samples. The respective fit parameters are shown in **Table 3**. The two samples with intermediate edge energies exhibited comparable backscattering features and were fit with an O with a coordination of 2.6 (Sb soil) and 3.1 (Region 1) at distance 1.96 and 1.97Å, consistent with trivalent Sb speciation. Based on assumptions concerning the structure of the two samples, the higher order shells were fit with Sb-Sb scattering paths, but iterations did not significantly improve the fit. Particularly for the Sb hotspot in Region 1, there likely is a heavy atom in a more distant shell based on the small backscattering feature at 2.8Å (uncorrected for phase shift) and an unfit oscillation feature in the k^3 weighted EXAFS spectra at approximately 7.2 Å⁻¹. However, the backscattering features are weak, indicating a relatively disordered system. Therefore, only the first shell fittings are presented for Sb soil and Region 1. The weathering crust was the most oxidized of the samples analyzed, bearing a more prominent white line than the other samples with an absorption edge energy of 30,495 eV (**Figure 17**). The Sb-O path was best fit with a coordination number of 5.3 at a distance of 1.99 Å, indicative of an octahedral-coordinated pentavalent Sb species. The larger distance FT peaks were fit with an Fe atom at 3.15 Å and a coordination number of 3 (**Table 3**).

Sample	E_0 (eV)	k -range	R -range (Å)	Shell	CN ^d	R (Å) ^e	σ^2 (Å ²) ^f	ΔE_0 (eV) ^g	R -factor ^h	Red χ^2 ⁱ	Ind. Pts. ^j
^a Weathering Crust	30,495	3.0 - 10.5	1.1 - 4	Sb-O	5.3(1)	1.99(2)	0.002(2)	11(2)	0.007	62.9	14
				Sb-Fe	3(1)	3.15(3)	0.006(8)				
^b Sb soil	30,492	3.0 - 9.0	1 - 5	Sb-O	2.6(8)	1.96(3)	0.002(4)	10(4)	0.06	30.1	15
^c Region 1-4	30,492	3.0 - 9.0	1 - 4.5	Sb-O	3.1(2)	1.97(3)	0.005(4)	7(3)	0.03	45.4	13

^aWeathering crust surrounding approx. 15 bullets from the historic shooting range site, removed and consolidated.

^bMetallic Sb powder scrubbed onto local, uncontaminated soil adjacent to the historic shooting range site

^cSb hotspot from Region 1-4 historic shooting range sample

^dCoordination number

^eBond length

^fDebye-Waller factor (mean-square amplitude reduction factor) including thermal and static disorder components

^gEnergy shift between the theoretical and measured spectrum

^h R -factor = $\frac{\sum_i (data_i - fit_i)^2}{\sum_i data_i^2}$

ⁱRed $\chi^2 = \frac{N_{fit}}{N_{pts}} \sum_i \left(\frac{data_i - fit_i}{\sigma_i} \right)^2 / (N_{fit} - N_{par})$

^jIndependent points ($N_{pts} - N_{par}$)

Table 3. Fitting parameters and EXAFS results for historic shooting range samples. Fitting was done in R-space, k-weights of 1,2 and 3 were fitted simultaneously and the amplitude reduction factor (S_0) was set at 0.97.

Therefore, it appears that the speciation of Sb in the alteration crust is dominated by an Sb-Fe sorption complex. The Sb-Fe distance for the weathering crust sample (3.15 Å) is consistent with edge-sharing as found by previous authors (~3.10 Å Scheinost et al., 2006; ~3.11-3.13 Å Ackermann et al., 2009; Ritchie et al., 2013). The relatively high Sb-Fe coordination number we observe (~3) has been attributed to the presence of tridentate Sb octahedral complexes or direct

incorporation of Sb into the structure of Fe oxides, e.g. 2.0-2.5 (Guo et al., 2014); 2.9-3.5 for Sb(V) in ferrihydrite (Mitsunobu et al., 2006).

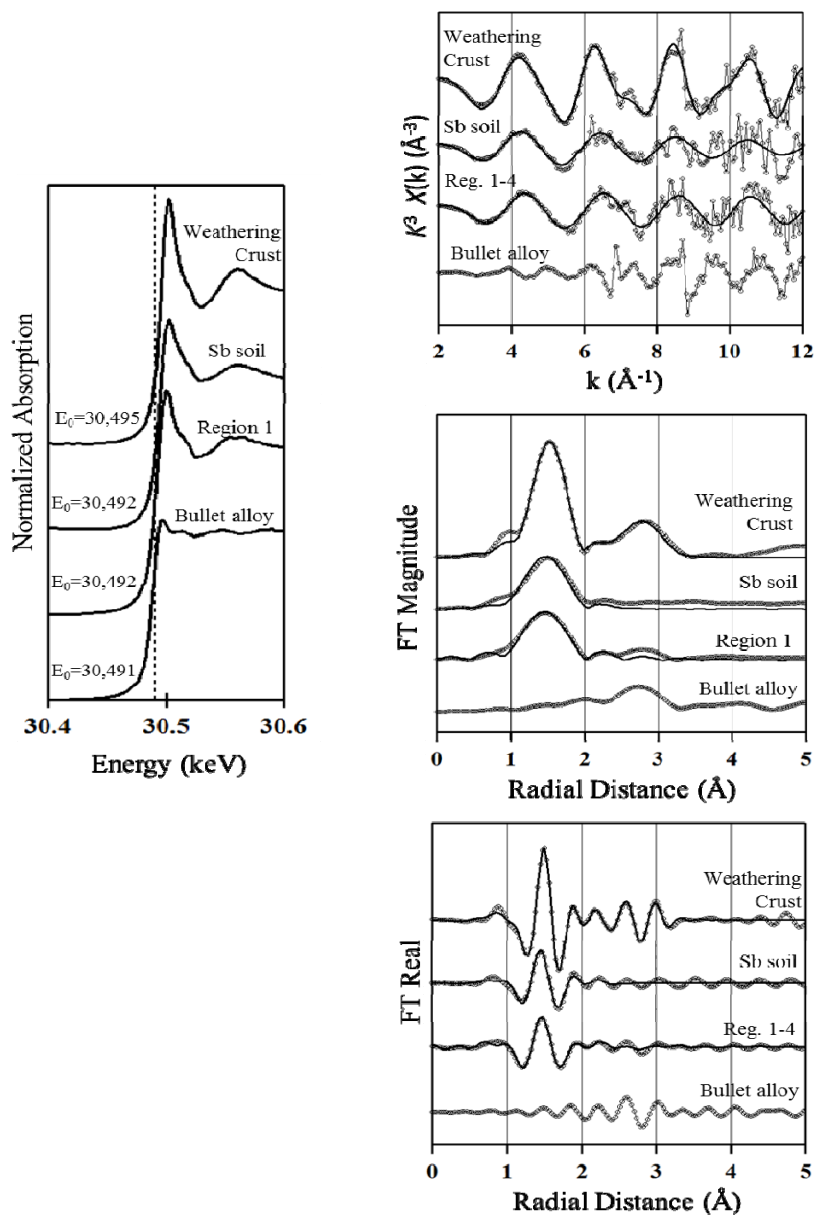


Figure 17. Sb K-edge EXAFS spectra of samples collected from the historic shooting range (weathering crust and Region 1), a laboratory generated sample (Sb soil) and an unfired, new bullet. Empty gray circles correspond to experimental data and solid black lines represent best fit. EXAFS data was processed using the Athena interface (Ravel and Newville, 2005) to the IFEFFIT (Newville, 2001) program. The background subtraction, normalization, and conversion into k-space was performed (Kelly et al., 2008), the spectra was Fourier transformed over k-range from 3-9, and analyzed using the Artemis interface (Ravel and Newville, 2005) to the IFEFFIT (Newville, 2001) program. Theoretical scattering paths were based on the crystal structure of Sb_2O_5 (Jansen, 1979).

The trivalent Sb weathering product observed in the fracture in Region 1 is likely a transient weathering product and not stable long-term unless in reducing conditions (Johnson et al., 2005; Ilgen et al., 2014). However, the occurrence has implications to the overall mobility and toxicity of Sb. Antimony (V) species will have enhanced mobility at circum-neutral pHs, whereas the mobility of Sb (III) species is nearly independent of pH (Johnson et al., 2005) and trivalent Sb compounds have a ten times higher acute toxicity than pentavalent species (Krachler et al., 2001). Besides in the alteration crust and bullet fracture (Region 1), Sb was not detected in the soil either independently or associated with Fe. Rapid oxidation of Sb(III) to Sb(V) (e.g. Ilgen et al., 2014) in berm water could explain the low concentration of soil-bound Sb. Other potential sorbents for Sb were investigated including organic fractions and clay mineral surfaces, all of which were detected in the soil, but did not contribute significantly to the overall best fits for the x-ray absorption spectra.

4.5 Oxidation and mobilization of Sb metal in simulated groundwater

Field measurements, due to the complex range of variables involved, often require laboratory experiments to assist in interpretation. For this, we designed and performed a set of batch experiments to study the oxidation and dissolution of metallic Sb as a function of solution composition (Ilgen et al., 2014, 2016). The overall goal of these experiments was to better understand the factors controlling the $\text{Sb}(0) \rightarrow \text{Sb}(\text{III}) \rightarrow \text{Sb}(\text{V})$ oxidation sequence in heterogeneous systems. We also tested how the addition of metallic Pb and the organic ligand ethylenediaminetetraacetic acid (EDTA) affect the rates of $\text{Sb}(0)$ oxidation and dissolution, and characterized the solid oxidation products which may potentially control aqueous concentrations of Sb. The simulated ground water (SGW) was made using salts of ions typically encountered in natural waters (e.g. $\text{Na}(\text{I})$ and $\text{Ca}(\text{II})$) in Milli-Q deionized (18.2 M Ω cm) water (DI H_2O). The summary of experimental conditions is shown in **Table 4**. The oxidation state of Sb in aqueous samples was determined using LC-ICP-MS. Post-reaction solid phases were characterized using EXAFS, scanning electron microscopy (SEM), and x-ray powder diffraction (XRD).

Batch	DI/Sb	^{a)} SGW/Sb	SGW/Sb/EDTA	DI/Sb/Pb	DI/Sb/Pb/EDTA	DI/Sb/ $\text{Ca}(\text{NO}_3)_2$	DI/Sb/ NaNO_3
Medium	DI H_2O	SGW	SGW	DI H_2O	DI H_2O	DI H_2O	DI H_2O
Sb^0 , g	0.100	0.100	0.100	0.050	0.050	0.100	0.100
Pb^0 , g	\	\	\	0.050	0.050	\	\
EDTA, mM	\	\	10	\	10	\	\
Na^+ , mM	\	0.29	20.29	\	20.0	\	10
Ca^{2+} , mM	\	1.24	1.24	\	\	10	\
NO_3^- , mM	\	1.97	1.97	\	\	20	10
Cl^- , mM	\	0.28	0.28	\	\	\	\
Time, days	222	222	146	146	146	146	146

Table 4. Composition of the Sb metal oxidation batch reactors. The experiments were performed at 20 °C in equilibrium with atmosphere, light was not excluded, pH was measured during sampling.

The observed mobilization of Sb is fast: after 5-15 minutes of reaction, the aqueous concentration reached 0.05-0.60 mM, with 96.3-100% as $\text{Sb}(\text{III})$ (**Figure 18**). Senarmontite (Sb_2O_3) is the primary crystalline oxidation product in all examined systems (with exception of DI/Sb/Pb reactor) based on the EXAFS (**Appendix A, Table A4** and **Figure 19**) and XRD analysis (data not shown). By completion of the experiment (>146 days) the aqueous concentration of $\text{Sb}(\text{III})$ is apparently controlled by the mineral phase solubility, while on a shorter time scales the concentration of $\text{Sb}(\text{III})$ indicates significant over-saturation with respect to senarmontite.

The extent of $\text{Sb}(\text{III})$ oxidation to $\text{Sb}(\text{V})$ depends on the aqueous composition: $\text{Sb}(\text{V})$ was the dominant aqueous species (56-84% of total dissolved Sb) in the systems with simulated ground water (SGW/Sb), dilute NaNO_3 (DI/Sb/ NaNO_3) and $\text{Ca}(\text{NO}_3)_2$ (DI/Sb/ $\text{Ca}(\text{NO}_3)_2$) solutions, and

DI H₂O (DI/Sb). Complexation with EDTA decreases the rate of Sb(III) oxidation to Sb(V), but does not stop this reaction. Some Sb(0) remains in the systems after 5 months of reaction, as determined by XRD. The upper concentration of Sb(V) is controlled by the precipitation of mopungite (NaSb(OH)₆, in reactors where Na(I) is above 20 mM), and, likely, amorphous Pb[Sb(OH)₆]₂ (in reactors with added Pb). The observed solubility of Sb(V) in the systems with Ca(II) is significantly larger than solubility reported for romeite (Diemar et al., 2009) and amorphous Ca[Sb(OH)₆]₂ (Johnson et al., 2005). Results of this study indicate that mobility of Sb in soils could be greater than currently predicted by thermodynamic models due to levels of Sb(III) and Sb(V) released during Sb(0) oxidation experiment in excess of the equilibrium with senarmonite and known solubility constants in Ca(II) containing systems.

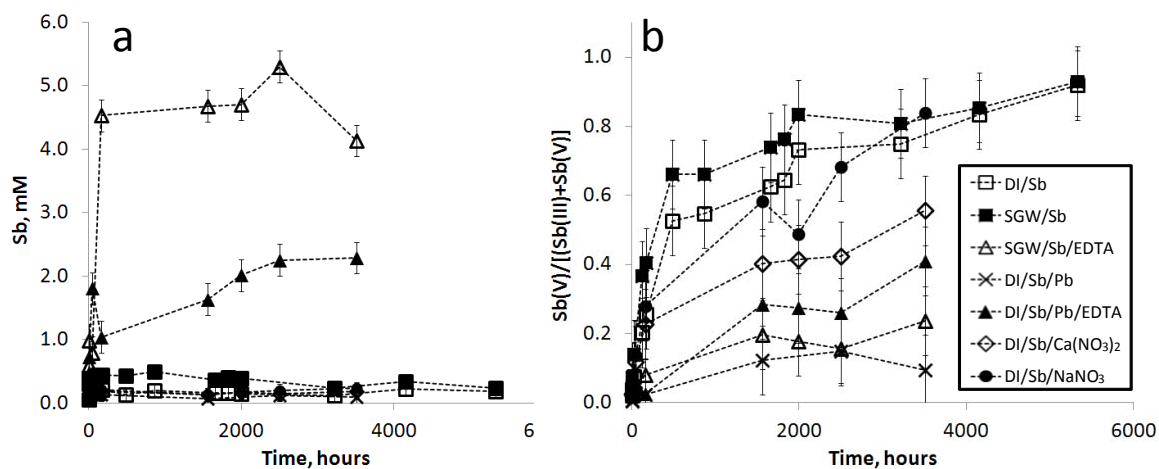


Figure 18. Antimony oxidation and dissolution in batch reactors as a function of time: a) Changes in the aqueous concentration of the total dissolved antimony; b) The extent of Sb(0) oxidation to Sb(III) and further to Sb(V).

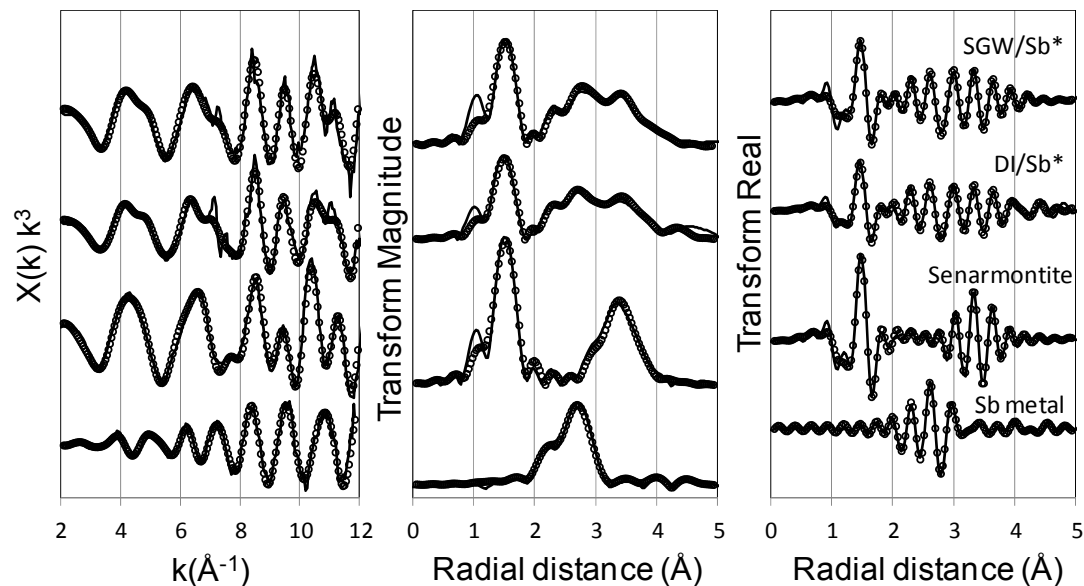
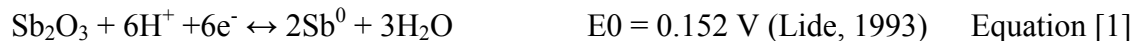


Figure 19. EXAFS data (solid lines) and fit (empty circles) for Sb(0), senarmontite, and the post-reaction solids collected after 5 months of reaction from the DI/Sb and SGW/Sb batch reactors.

Furthermore, in the batch reactor with added Pb(0) (DI/Sb//Pb) the extent of Sb(III) oxidation to Sb(V) was significantly lower compared to the identical batch reactor without the addition of lead (DI/Sb). The low Sb(V) concentration in the DI/Sb/Pb batch reactor and absence of Sb(III) and Sb(V) solid phases in the XRD analysis indicate that addition of Pb(0) inhibits the oxidation of Sb(0). Two plausible explanations for this observation include: 1) Pb(0) buffers the redox potential of the system, making it too reducing for Sb(0) to oxidize, and 2) Pb(0) oxidation products are deposited on the Sb(0) particles which decreases their reactive area. The first scenario is supported by considering the tabulated standard redox potentials involving Pb(0) and Sb(0):



where we would expect Pb(0) oxidation to poise the system at a much more reducing condition than would favor Sb(0) oxidation (assuming the reactions are coupled). The experimental findings indicate that Pb(0) has a significant effect on the degree of Sb(0) oxidation and mobilization. During the corrosion of lead/antimony bullet alloys, it is expected that the oxidation of Sb will be impeded prior to the complete oxidation of Pb metal. Future work should be focused on understanding of the mechanism by which metallic Pb impedes the oxidation of Sb(0) whether this is due to competitive oxidation, coupling of Sb and Pb redox reactions, and whether amorphous $\text{Pb}[\text{Sb}(\text{OH})_6]_2$ is the predominant solid phase immobilizing both Sb and Pb.

The summary of the processes observed in the batch reactors is shown in **Figure 20**, and Equations [3–6]:

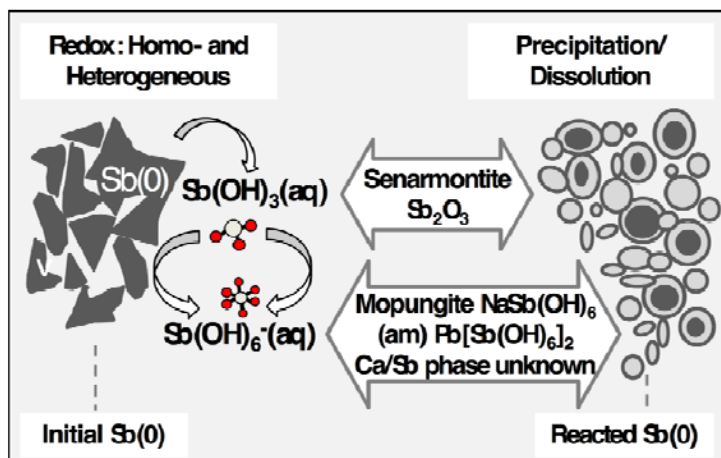
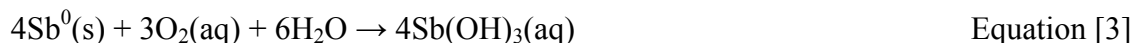


Figure 20. Processes observed in the batch reactors: heterogeneous oxidation of Sb(0) to Sb(III) and, further, to Sb(V), homogeneous oxidation of Sb(III) to Sb(V), and precipitation/dissolution of the Sb(III) and Sb(V) phases.

4.6 Alteration of Sb metal surfaces in model laboratory systems

Our field data were further complimented by laboratory determination of the intrinsic rates (factoring out surface area) of Sb(0) fragment alteration as a function of pH. This is essential to estimating potential for metallic fragments to serve as a source of Sb(III/V) to soil solution. To answer this question we prepared a set of circular pucks of 12-mm diameter by coring a bulk polycrystalline Sb(0) ingot and polished the surface of those pucks to a mirror finish. The experimental study focused on understanding the effect of common cations (Na(I) and Ca(II)) on the formation of precipitates on an Sb(0) puck surface as a function of time during oxidation in SGW. Solutions were prepared at a range of environmentally relevant pH values, and a fixed (environmentally relevant) ionic strength ($I = 0.01\text{ M}$). We compared these results to the same processes in background solutions containing either DI water or 30% hydrogen peroxide (H_2O_2). We determined the speciation and preferred orientation of the precipitates with grazing incidence x-ray diffraction (GI-XRD) and texture measurements, respectively, and the morphology of the altered surfaces with scanning electron microscopy (SEM).

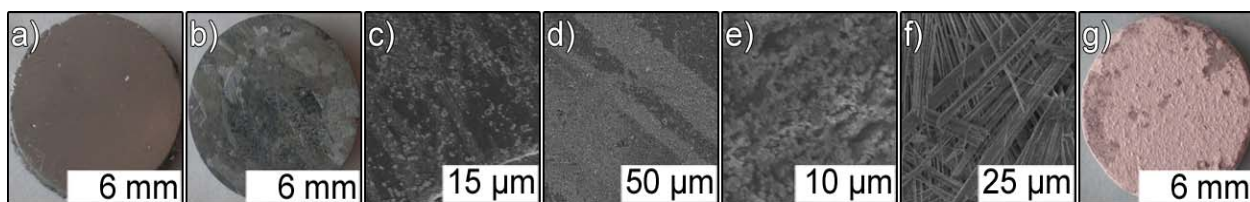


Figure 21. Comparison of antimony (Sb) metal surfaces before and after 51 days of equilibration: (a) clean Sb surface, (b) and (c) photo and scanning electron microscope image (SEM) of Sb surface reacted in deionized water, (d) SEM of a surface reacted in simulated groundwater (SGW) pH = 5.6, (e) SEM of a surface in SGW pH = 7.5, (f) and (g) SEM and photo of a surface reacted in SGW pH = 8.4.

The surface of Sb(0) oxidizes rapidly under the examined conditions; within 24 hours we observed the formation of cubic and orthorhombic polymorphs of Sb_2O_3 (senarmontite and valentinite) on surfaces exposed to DI H_2O . Equilibration over a period of 51 days resulted in formation of a crust that grew progressively thicker with increasing initial pH (**Figure 21**) and was accompanied by consumption of hydroxide ions from the background solution as indicated by a measured drop in pH during reaction. Valentinite exhibited strong preferential orientation with the a-axis, the shortest of the unit cell edges, normal to the Sb(0) surfaces (**Figure 22**). The valentinite fraction in the precipitate increased with increasing solution pH but no measurable difference in speciation was found between the addition of Na(I) and Ca(II) background solutions. An oxidation end member, hydrated Sb_2O_5 , precipitated on Sb(0) surfaces only in the presence of the extremely oxidizing H_2O_2 solution.

These measurements show a detailed connection between soil solution pH and likely solid phase speciation of the corrosion products. However, the laboratory measurements suggest that Sb(III) bearing solids are a predominant reaction product, where field measurements find only little evidence for these phases. This suggests that in field settings weathering reactions associated with Sb in bullet alloys produces dissolved (oxidized) Sb that is highly mobile and transported from the localized region of weathering reactions.

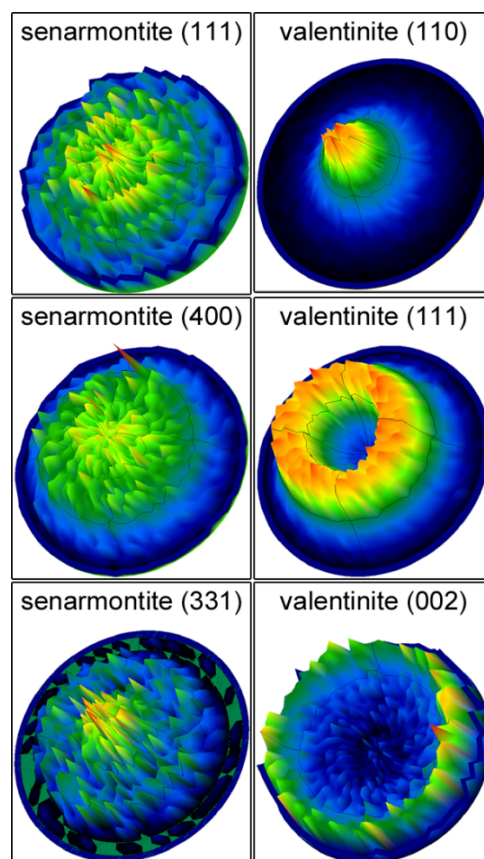


Figure 22. Orientation of two polymorphs of Sb_2O_3 , isometric senarmontite and orthorhombic valentinite, identified on surface of antimony metal reacted for 51 days in a simulated groundwater ($I = 0.01 \text{ M NaNO}_3$) with initial pH adjusted to 8.4 by Na_2CO_3 .

4.7 Column studies and Pb and Sb attenuation by iron amendments

As we observed in both field and laboratory studies, oxidized Sb associated with weathering of bullet alloys is highly mobile. One aspect of our study was to determine if there was a simple, cost effective, method for attenuating the mobile Sb and associated Pb. The remediation of Pb and Sb in shooting range soils has been the subject of recent studies due to the large amount of ammunition deposited on military training lands (Jardine et al., 2007; Conesa et al., 2010; Griggs et al., 2011; Moon et al., 2013a-c; Dorjee, et al., 2014). A number of strategies have been studied to limit Pb mobility including additions of phosphate to form insoluble lead-phosphate compounds (Jardine et al., 2007), carbonate to buffer the pH and form less soluble lead-carbonate phases (Spuller et al., 2007; Griggs et al., 2011), and red mud, fly ash, oyster/mussel shells, cow bone and biochar to reduce metal availability (Lee et al., 2009; Moon et al., 2013a; Moon et al., 2013b; Moon et al., 2013c; Ahmad et al., 2014). Overall, the soil additions limited Pb mobility, biochar was shown to also limit Sb mobility to some extent, but cow bone and mussel shell increased Sb mobility (Ahmad, et al., 2014). Antimony may also be displaced from solids via competition with other anionic species such as phosphate or carbonate, thus increasing the mobility (Conesa et al., 2010). Therefore, design of a remediation strategy for both Pb and Sb is complicated by their differing geochemical behaviors.

While Pb amendment strategies are the focus of numerous studies, a lesser number of have focused on limiting Sb mobility in shooting range soils and the majority have centered around natural attenuation via sorption complexes with Fe present in soil (Scheinost, et al., 2006; Manaka, et al., 2007; Mitsunobu, et al., 2010a) and manual Fe soil additions (Spuller et al., 2007; Okkenhaug, et al., 2013). Antimony concentrations in solution have been shown to be reduced with the addition of polyaluminum chloride, ferric chloride and freshly precipitated ferrihydrite (Bagby and West, 1995; Kang et al., 2003; Guo et al., 2009). In addition, iron oxyhydroxides have the ability to form surface complexes with both cationic and anionic species due to variable charged surface groups (Dzombak et al., 1990), giving them potential to work as an effective sorbent for both Pb and Sb (Belzile et al., 2001; Leuz et al., 2006; McComb et al., 2007).

Here we employed two types of Fe amendments to soil columns containing spent bullets. The amendments were composed of: (1) a slurry solution of nano-zero valent iron (nZVI) and (2) an FeCl_2 solution with CaCO_3 to act as a pH buffer. Twelve acrylic soil columns were loaded with the four (uncontaminated) soils from our field study (loamy soil, sandy soil, sandy loam and loamy sand). These soils were fired into with 5.56 mm bullets in a controlled firing event prior to loading the columns. Once the columns were loaded they were reverse-flushed with electrolyte solution to simulate ‘wet’ and ‘dry’ events typical of the conditions observed at our field site at Ft. Greely, Alaska.

The columns were initially saturated for 1 hour and then drained to produce sample 1. The columns were then repeatedly flushed and drained for the next 100 days for a total of 15 sampling events. Each sampling event had various ‘saturation’ times and ‘drying’ durations to simulate rain and drying cycles. After the collection of runoff sample 15, the two types of Fe amendments were introduced to a subset of the columns (5-8 and 9-12) representing the duplicates of the 4 main soil types in columns 1-4. The saturation durations for the remainder of the runoff samples (16-30) were kept constant at 1 hour. Nano-scale zero-valent Fe (nZVI) was

added to columns 5-8 and $\text{FeCl}_2/\text{CaCO}_3$ was added to columns 9-12. Both amendments were introduced to the column systems in reverse-flow in a slurry solution and allowed to fully saturate the soils. The column eluent from each sampling event was monitored for major and minor dissolved elements. After completion of the runoff study, the soil from all columns was analyzed for bulk metal concentrations and a subset of the soil from each column was analyzed for Pb and Sb speciation using synchrotron based x-ray absorption spectroscopy (XAS).

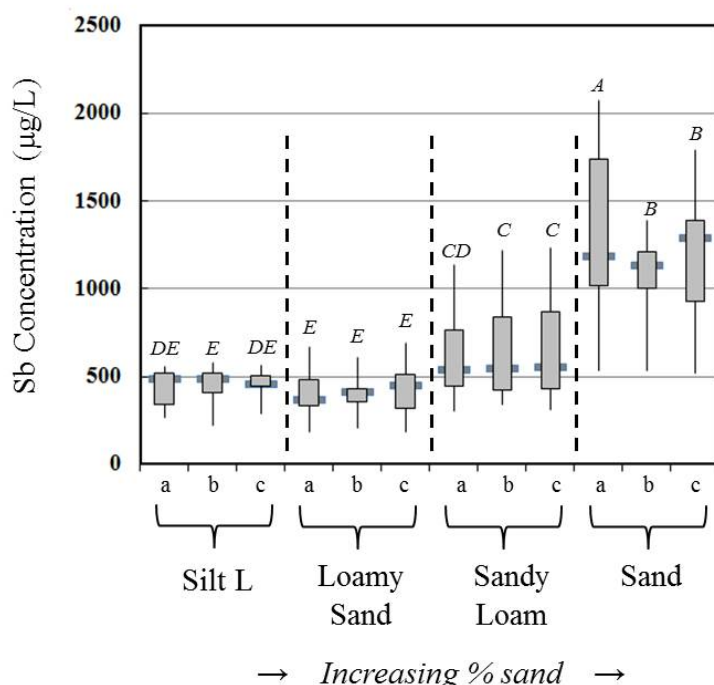


Figure 23. Box plot of Sb concentrations in runoff leachate for each of the soil types in all the columns prior to the Fe additions. Concentrations of Sb in each soil type leachate were measured in triplicate indicated by ‘a, b, c’ on the plot. Plot is arranged in order of increasing % of sand. Dark gray lines indicate median values during the runoff experiment (prior to the Fe additions) and the gray boxes depict the lower (25th percentile) and upper (75th percentile) quartiles. A, B, C, D, E indicates levels that are statistically different between data sets using one-way ANOVA with bivariate analysis and Student’s t-test to compare means, p-value <0.05. Levels connected by the same letter were determined to not be significantly different at p < 0.05.

Analysis of the column runoff highlights the unique behavior for both Pb and Sb in relation to soil type. Antimony concentrations were the highest in the sand column effluent (sand ‘a’), and lowest in the silt loam and loamy sand draining columns (silt loam ‘b’ and loamy sand ‘a, b, c’). Results are shown in **Figure 23** and depicted using box plot diagrams for each triplicate column as a function of soil type. Statistically significant differences between columns are indicated using lettered levels. In general, the results from the soil column analysis showed similar behavior between triplicates columns (levels connected by the same letter are not significantly different at p < 0.05), except for the sand column ‘a’, which contained the highest Sb concentrations, overall. In [Appendix A, Figure A2](#) we show that the mobile Sb was

predominantly in the Sb(V) oxidation state. In comparison, Pb behavior was distinct relative to Sb. Lead concentrations were significantly lower overall relative to Sb (**Figure 24**) with the highest Pb coming in the effluent from silt loam column 'a' and lowest in the effluent draining from sand column 'b' (**Figure 24**). Despite differences between silt loam 'a' and sand 'b' end members, distributions of Pb for the mixed soil effluent and the other end member columns were not statistically different at $p < 0.05$ (**Figure 24**). The column runoff analysis highlighted major differences between Pb and Sb mobility. Antimony concentrations are higher than Pb in the column runoff. Particularly for sand and the sand mixed soils, the concentration of Sb is an order of magnitude higher than Pb in some samples, demonstrating the tendency of Sb to become mobilized in shooting range systems more so than Pb, despite Pb comprising ~90% of the bullet mass. The higher content sand soil promotes the retention of Pb, whereas the higher content silt loam and loamy sand soil promotes the retention of Sb.

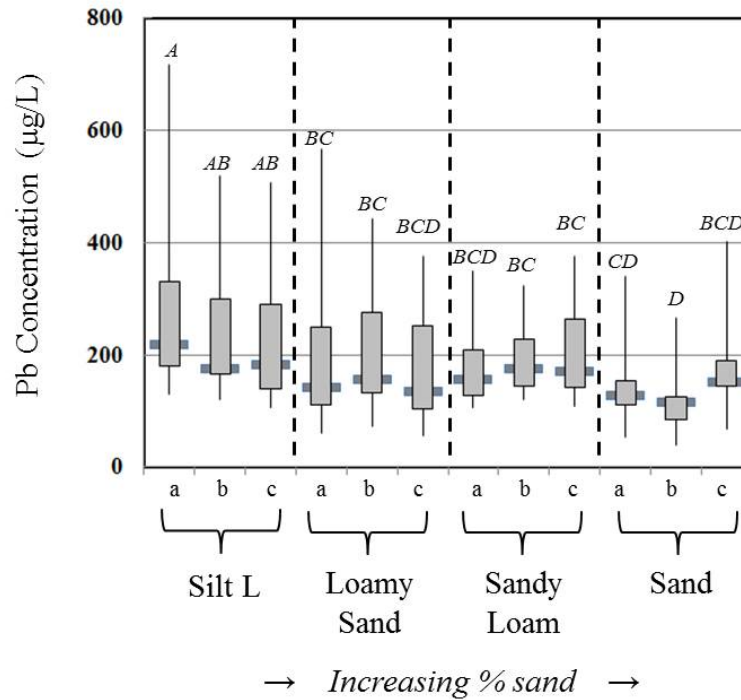


Figure 24. Box plot of Pb concentrations in runoff leachate for each of the soil types in all the columns prior to the Fe additions. Concentrations of Sb in each soil type leachate were measured in triplicate indicated by 'a, b, c' on the plot. Plot is arranged in order of increasing % of sand. Dark gray lines indicate median values during the runoff experiment (prior to the Fe additions) and the gray boxes depict the lower (25th percentile) and upper (75th percentile) quartiles. A, B, C, D indicates levels that are statistically different between data sets using one-way ANOVA with bivariate analysis and Student's t-test to compare means, p -value < 0.05 . Levels connected by the same letter were determined to not be significantly different at $p < 0.05$.

As noted above the saturation times were varied prior to the iron amendments to test the influence of wetting/drying cycles on Pb and Sb mobility. Lead concentrations as a function of saturation time are shown in **Figure 25**. Lead concentrations are grouped by soil type, in order of increasing % of sand content. For all soils there is an increase in the Pb concentration as a function of increasing saturation time, particularly over the first 40 hours. The initial spike at short sampling times are associated with the fresh bullet samples – these likely have an increased rate of solubility due to the presence of fresh surfaces associated with the bullet fragments. The decreasing concentration of Pb in the sand soil after 120 hours of saturation time is likely a result of saturation of Pb in solution and subsequent precipitation and/or sorption processes occurring between 80 and 120 hours of saturation (see discussion below).

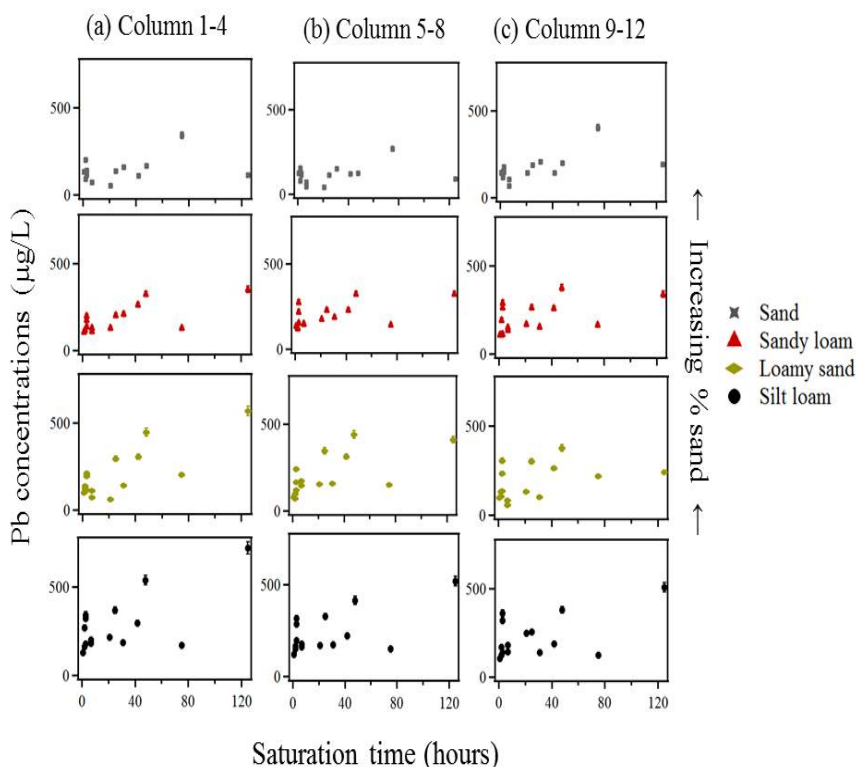


Figure 25. Effects of saturation time on Pb concentrations as a function of soil type and column set (a, Columns 1-4; b, columns 5-8; and c, columns 9-12) in triplicate in the column runoff experiment.

The effect of saturation time on the Sb concentrations is shown in **Figure 26**. Within the sand and sandy loam soils there is a steady rise in Sb concentration with saturation times up to about 40-80 hours. The lower sand content (and more acidic) soils show Sb concentrations reaching an apparent steady state at very short saturation times. The Sb concentrations in the silt loam and loamy sand are also significantly lower than the higher sand content soils.

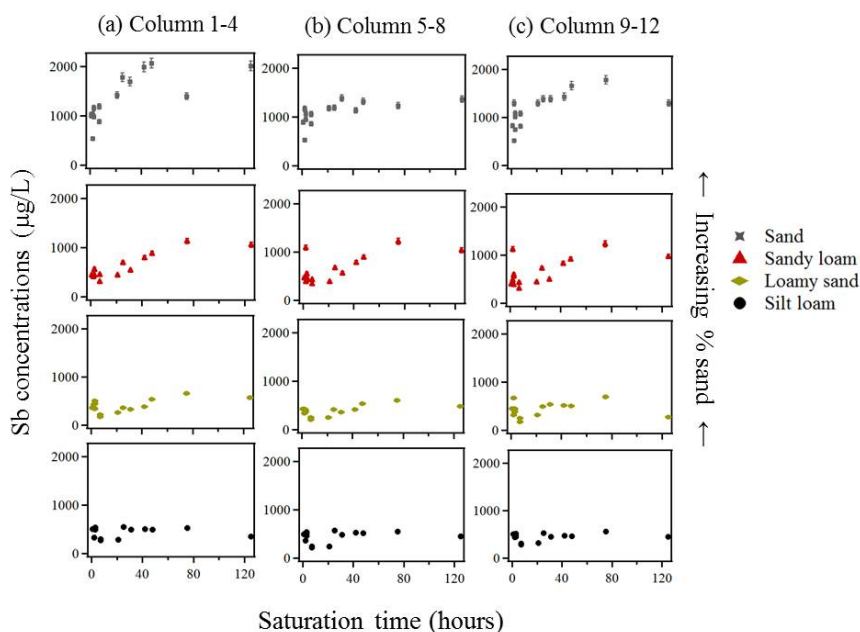


Figure 26. Effects of saturation time on Sb concentrations as a function of soil type and column set (a, Columns 1-4; b, columns 5-8; and c, columns 9-12) in triplicate in the column runoff experiment.

The effect of the addition of the iron amendments to the soil columns is shown in **Figures 27 and 28**. Antimony was significantly immobilized in systems implementing the $\text{FeCl}_2/\text{CaCO}_3$ amendment (**Figure 27**). Concentrations of Sb for the soil types in the sample prior to the Fe addition were approximately 200 $\mu\text{g/L}$ for the silt loam draining systems and 1000 $\mu\text{g/L}$ for the sand draining system and both systems saw a sharp decrease to less than 1 $\mu\text{g/L}$ (**Figure 27**). The addition of the nZVI had only a moderate effect on immobilizing Sb, particularly in the silt loam runoff. The general decrease in Sb concentrations in the unamended systems could be attributable to the lower saturation times for this phase of the experiment, where the saturation was kept constant at 1 hour per sampling event.

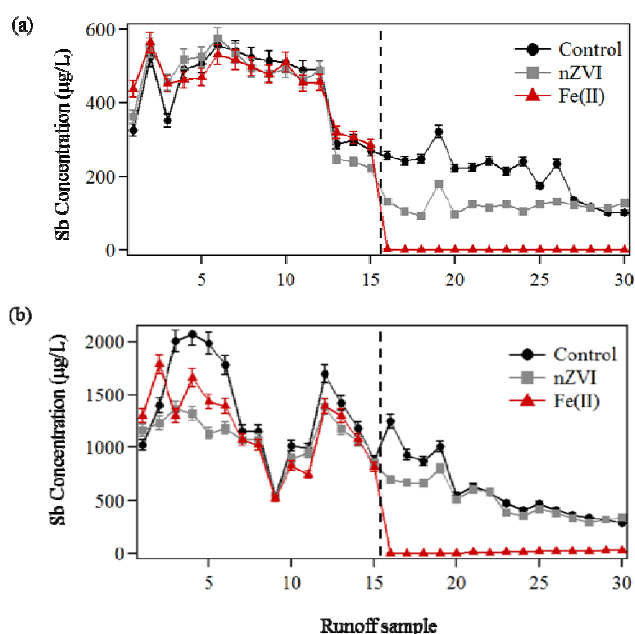


Figure 27. Antimony concentrations in runoff leachate for the (a) silt loam column set and the (b) sand column set (soil type end members). The amendments were added after runoff sample 15 and were (1) no amendment in the controls, (2) nZVI and (3) $\text{FeCl}_2 + \text{CaCO}_3$. Black dotted line indicates when the amendments were added.

Upon the addition of $\text{FeCl}_2/\text{CaCO}_3$ amendment there was an initial mobilization of Pb (**Figure 28**). The rise in concentration is consistent with an observed drop in pH caused associated with the hydrolysis of Fe(II). Over time the pH stabilized and concentrations of Pb dropped back to values similar to the control columns. The addition of the nZVI amendment also mobilized Pb initially in the silt loam draining columns, but not the sand columns. However, Pb concentrations in the sand columns remained similar to the Pb concentrations in the control columns. Overall, the Pb concentrations were lowest in the control columns, except for the silt loam draining soils with the nZVI addition after sample 21.

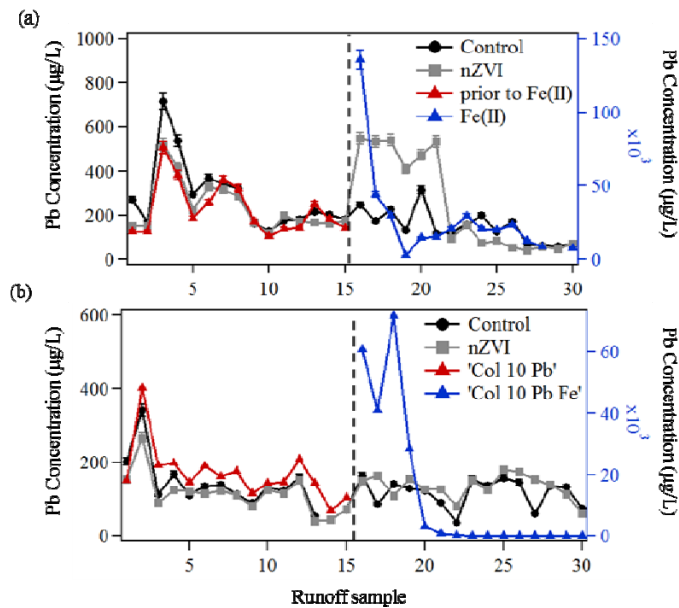


Figure 28. Lead concentrations in runoff leachate for the (a) silt loam column set and the (b) sand column set (soil type end members). The amendments were added after runoff sample 15 and were (1) no amendment in the controls, (2) nZVI and (3) $\text{FeCl}_2 + \text{CaCO}_3$ (plotted on the right axis for scale). Black dotted line indicates when the amendments were added.

The trends observed with iron-amendment are strongly correlated with a change in pH associated with the addition of the treatment. **Figure 29** shows the correlation between Pb and Sb with pH. The hydrolysis of Fe results in a pH drop. The FeCl_2 amendment also included a CaCO_3 addition to buffer the pH change, however, we still observed pH's as low as 3.15 after the addition. The decrease in pH led to an increase in Pb concentration, with the opposite behaviour observed for Sb. This observation is supported by other studies that find Sb mobility decreasing with decreasing pH (except for very acidic environments; $\text{pH} < 2$ and environments with high phosphate fraction) (Johnson et al., 2005; Okkenhaug et al., 2016) and Pb mobility increasing with decreasing pH, similar to other metal cations in solution (Elzahabi and Yong, 2001; Cao et al., 2003; Rooney et al., 2007). Right around circum-neutral pH we see a large changes in the Sb and Pb concentrations, likely associated with their differences in sorption affinity to the soil particles with pH. For soils below pH of about 6 the Sb concentrations are at or below $1 \mu\text{g/L}$. These observations suggest that while the addition of the iron amendment may increase the number of available sorption sites for both Pb and Sb, careful control of the pH is required to result in a reduction in the concentration. Furthermore, the differing behavior of Pb and Sb suggest that this or similar treatments will be challenging to apply without mobilizing one element of the other.

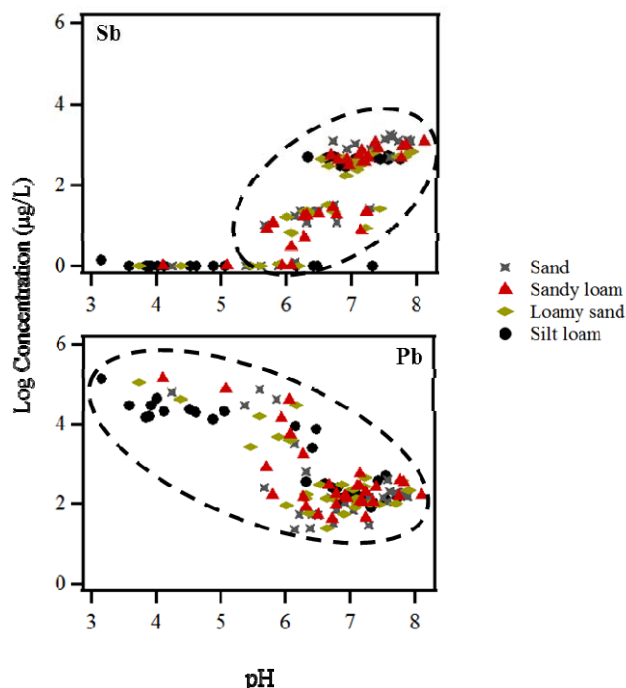


Figure 29. Trends between log Pb and Sb concentrations ($\mu\text{g/L}$) and pH as a function of soil type in the Fe(II) amended columns.

Another key aspect of this study was to try and determine whether the mobilized metal(oids) were truly dissolved or associated with colloidal particles. The majority of our solution analysis included samples that were filtered to 0.45 μm , which is the commonly used method for operationally defined “dissolved” species. In order to investigate if a significant fraction of these “dissolved” species were in fact associated with colloidal particles we utilized a Postnova Field Flow Fractionation instrument, AF2000-FFF (Postnova Analytics, Landsberg, Germany), coupled to a UV-VIS diode array detector (UV-DAD; Shimadzu SPD-M20A) and to an ICP-MS for colloid separation and compositional characterization. Analyses were performed on mixed-soil types column runoff.

The FFF fractogram (UV signal) of the mixed soil runoff is shown in **Figure 30a** with the corresponding element counts shown in **Figure 30c**. The void peak (0-100 seconds) is indicative of all particles passing through the 300 Da membrane and is correlated with the Cu, Fe and Sb peaks in the ICP-MS signal. These species are considered as the truly dissolved fraction of the sample. In addition to the void peak, there are increases in UV detector signal approximately 200, 600 and 1200 seconds in the UV spectra (**Figure 30a**). The shoulder at 200 seconds (visually expanded in **Figure 30f**) correlates with peaks in Ni and Pb ICP-MS counts and is mostly likely indicative of soil organic matter (SOM) particles that have a strong UV absorbance (e.g. humic/fulvic acids) (Regelink et al., 2013). The peak at 600 seconds is correlated with primarily Fe and Pb and is indicative of an inorganic Fe colloid. The ICP-MS counts of Fe versus Pb are shown in **Figure 30e**, and indicate that Fe concentrations are significantly greater than Pb (based on un-normalized counts). The peak from 1200-3000 seconds is broad and poorly

separated indicative of a wide range of colloidal sizes. This broad peak when coupled to the ICP-MS shows increases in Ni, Cu and Fe concentrations. Antimony and Pb do not seem to be co-eluted with this broad peak. Therefore based on these results we can say that in the sandy loam it appears that the majority of the mobilized Sb is dissolved. There is also a significant fraction of dissolved Pb, however, the majority of the Pb was found to be associated with Fe-colloids. There are also organic colloids that appear to be binding Pb, as well as Ni.

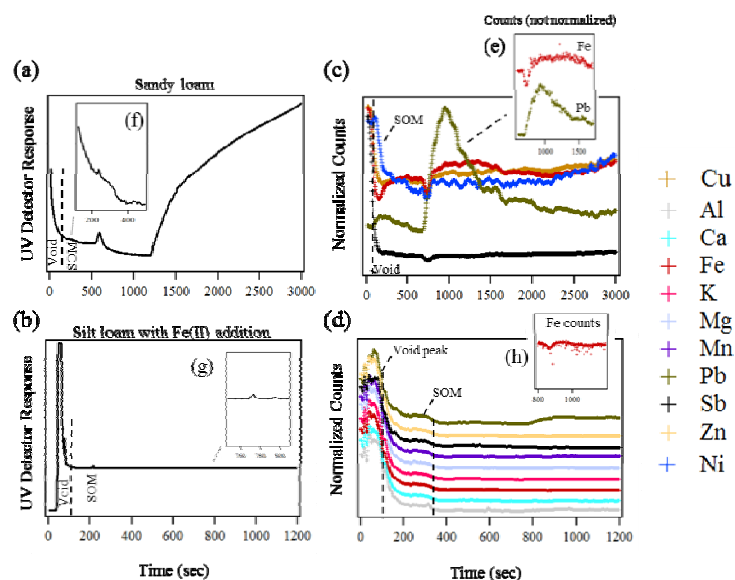


Figure 30. FFF-ICP-MS results of the sandy loam mixed soil column and the silt loam soil after the addition of the Fe(II) amendment. (a, b) correspond to FFF fractogram of time versus UV detector response (a; 254 nm and b; 284 nm) and (c, d) refers to in-line coupling to ICP-MS detector counts. There is approximately a 100 second delay between FFF and ICP-MS signal. The ICP-MS data has been normalized to 1 and stacked. The UV detector signal has been visually increased in (f) for the sandy loam and (g) for the silt loam with Fe(II) addition. The ICP-MS counts (not normalized) were visually increased in (e) for the sandy loam and (h) for the silt loam with Fe(II) addition.

Size fraction analysis was also performed on a silt loam draining runoff sample from the Fe(II) amended column. These results (**Figure 30b,d**) show an increase in the ICP-MS void peak intensity, indicating greater concentrations of dissolved species. The majority of the Pb, Zn, Sb, Mg, K, Fe, Ca and Al are all in the dissolved fraction. We also observe a small increases in element count (normalized) in **Figure 30d** that correlates to the increase in UV detector signal labeled SOM in **Figure 30b**. This suggests a minor amount of transport is still associated with the SOM after the amendment (and corresponding drop in pH). Therefore with the amendment,

the majority of metals are in the dissolved phase, with very little colloid facilitated transport. Furthermore, it is apparent that the addition of the Fe(II) amendment changed the particle size distribution of the system.

The above results suggest that the weathering of the bullet fragments in the soil lead to slow leaching of metals to solution, and this process is sensitive to the soil environment and solution pH. We further investigated the metal(loid) speciation using X-ray absorption techniques to characterize the weathering products in the solid phase in order to correlate with the observed solution behavior. The speciation of Pb was investigated using micro-focused Pb-L_{III} XANES on polished thin sections collected from the columns after the completion of the leaching experiment. Linear combination fitting of the Pb XANES spectra was carried out using a set of standards and model compounds, shown in **Figure 31** with corresponding fit parameters shown in **Table 5**. We were able to describe the sample XANES based only on contributions of four components; metallic Pb, lead oxide (litharge), lead carbonate (cerussite) and laboratory-prepared Pb(II) sorbed to synthetic Fe(III) oxides.

With respect to soil type, there was little distinction between the two soil end members in terms of Pb speciation, except for the generally greater presence of PbCO₃ in sand (**Table 5**). We note these are spot analysis and therefore expect the relative proportions to vary depending on location. However, we found that hydrocerussite did not significantly contribute to the best fits, and “sorbed” Pb was an important component to nearly all samples. With respect to Fe amendments, we saw little distinction in the near edge absorption spectra for Pb in the unamended, nZVI and FeCl₂/CaCO₃ columns, indicating Pb and Fe associations are present within all soil types, regardless of amendment.

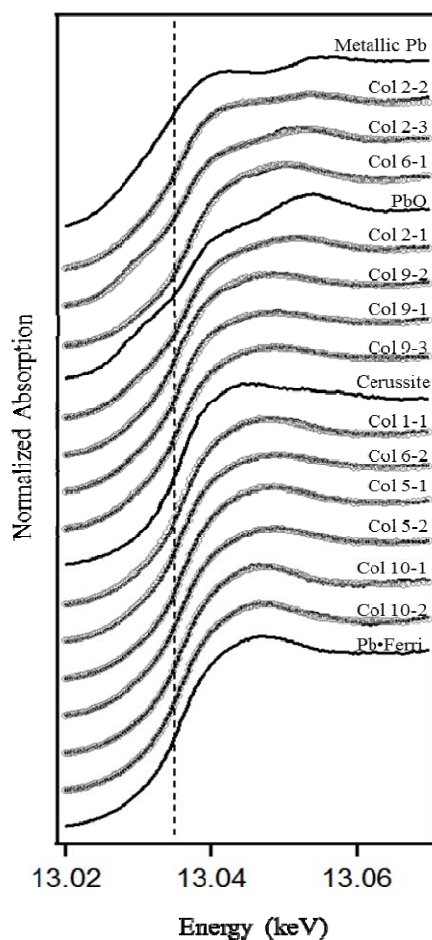


Figure 31. Normalized Pb-L_{III} μ -XANES spectra of end member column samples and corresponding linear combination fits. Black lines representing the LCF fits. Black dotted line represents the Pb L_{III} absorption edge.

Sample	Soil type	Addition	Spot	Pb(0)	L	C	Ferri	Sum	χ^2	red. χ^2
Col 1	Loam	none	1		10 (2)		85 (2)	95.4	2.3E-02	1.7E-04
Col 2	Sand	none	1		49 (1)		47 (1)	96.5	3.4E-03	2.5E-05
Col 2	Sand	none	2	29 (1)	23 (1)	48 (1)		99.5	8.8E-03	6.5E-05
Col 2	Sand	none	3	19 (1)	50 (2)		28 (1)	96.6	1.2E-02	9.4E-05
Col 5	Loam	nZVI	1		14 (1)	10 (1)	75 (1)	99.2	4.3E-03	3.2E-05
Col 5	Loam	nZVI	2		20 (1)		77 (1)	97.1	3.3E-03	2.5E-05
Col 6	Sand	nZVI	1		31 (1)	29 (1)	37 (2)	96.2	1.7E-02	1.3E-04
Col 6	Sand	nZVI	2		23 (1)	8 (5)	67 (4)	98.3	1.1E-02	8.2E-05
Col 9	Loam	Fe(II)	1	22 (1)	8 (1)		67 (1)	96.8	8.2E-03	6.2E-05
Col 9	Loam	Fe(II)	2	19 (1)	8 (1)		70 (1)	96.9	9.6E-03	7.1E-05
Col 9	Loam	Fe(II)	3	12 (1)	15 (1)		69 (1)	97.0	4.6E-03	3.4E-05
Col 10	Sand	Fe(II)	1			<5 (5)	94 (5)	94.3	1.2E-02	9.2E-05
Col 10	Sand	Fe(II)	2			<5 (4)	93 (4)	94.4	9.4E-03	7.0E-05

Table 5. Linear combination fitting results for column experiment end member soil types using reference spectra. Sum (%) refers to the actual sum of the partial contributions of reference spectra for the overall best fit. χ^2 and reduced χ^2 are derived from the fit refinement process. Pb(0) = Metallic bullet alloy; L = Litharge (PbO); C = Cerussite; Ferri = Pb(II) sorbed to Fe(III) oxides; error associated with fit in parenthesis.

Antimony speciation was examined using L_{III}-edge XANES measurements (**Figure 32**). The absorption energies of all samples analyzed were consistent with Sb(V). Sample energies ranged from 4139.3 eV to 4143.0 eV, while absorption energies for Sb(V) standards analyzed ranged from 4140.9 to 4143.6 eV. Metallic Sb edge energy is 4132.0 eV and Sb(III) standards range from 4133.1 to 4133.4 eV. The detection of Sb(V) in the column soil fraction is consistent with liquid speciation data that show the majority of dissolved Sb fully oxidized. Further speciation analysis of the solid phase Sb was not possible due to the low signal intensity associated with the diffuse distribution of Sb as shown in **Appendix A, Figure A3** (consistent with low concentrations of sorbed Sb(V) within the soil matrix).

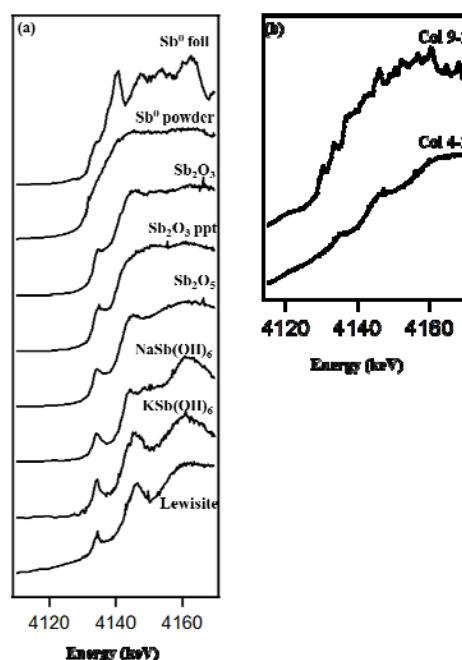


Figure 32. Normalized Sb-L_{III} μ -XANES spectra of (a) standards and model compounds used for visual comparison with (b) column samples.

4.8 Structure of sorption complexes binding to a hematite model substrate

One of the main goals of this project was to provide a molecular scale analysis of the controls on Pb and Sb mobility within shooting range soils. Based on the results above we observe that the mobile forms of the metalloids are soluble Pb(II) and Sb(V), transported as free ions in soil-solution and via colloid facilitated transport (in the case of Pb(II)). Furthermore, we observe that sorption to soil particles is a major retention/retardation mechanism for these species, with good evidence that iron-oxides in the soils (and associated with bullet oxidation) serve as primary sorbents. To further characterize the manner in which Pb(II) and Sb(V) bind to iron-oxide surfaces we undertook a series of measurements using model substrates to elucidate the structural details of the sorption complexes. These results provide additional details about the reactions occurring at the mineral-solution interfaces (which cannot be determined using field or bulk laboratory measurement) and also serve as a basis for our proposal of using clean metal-oxide substrates as passive sensors to provide qualitative indications of free metal(loid) mobility in field systems.

Crystal truncation rod (CTR) diffraction was utilized to investigate the adsorption of Pb(II) and Sb(V) on the hematite ($1\bar{1}02$) surface. CTR has been used to investigate the surface structure of numerous (hydr)oxides in the presence of water (liquid form or water vapor), including the hematite ($1\bar{1}02$) (Catalano et al., 2007; Tanwar et al., 2007ab), hematite (0001) (Trainor et al., 2004), hematite (110) (Catalano et al., 2009), corundum (0001) (Eng et al., 2000; Catalano, 2010), goethite (100) (Ghose et al., 2010), calcite ($10\bar{1}4$) (Geissbühler et al., 2004; Heberling et al., 2011), and muscovite mica (Cheng et al., 2001). Hematite (α -Fe₂O₃) was chosen in our study because it serves as a model substrate with similar types of surface functional groups to those exposed on other common forms of soil iron-(oxyhydr)oxides, such as goethite, lepidocrocite, and ferrihydrite, (Cornell and Schwertmann, 2003). The surface structure of the hydrated hematite ($1\bar{1}02$) has been well characterized using both theoretical and experimental approaches (Catalano et al., 2007; Tanwar et al., 2007ab; Lo et al., 2007), allowing us to investigate the stoichiometry of sorption complexes starting with a well constrained surface structure.

In all our measurements a clean and highly polished surface is reacted in situ with either Pb(II) or Sb(V) at fixed concentration and pH. Measurements were carried out the GSECARS surface diffraction facilities at the Advanced Photon Source, Argonne National Laboratory. Surface models were constructed on the basis of current knowledge of bulk termination for the hematite (1-102) surface (Tanwar et al., 2008) and refined using a modified version of the GenX analysis program (Björck et al., 2007), which takes advantage of a differential evolution algorithm in model fitting the measured CTR data. We have recently modified this package to use high performance parallel computing systems and included a bond-valence penalty function to help constrain the analysis.

The hematite (1-102) surface structure has two structurally distinct terminations. **Figure 33** illustrates the top and side views of these terminations that we identify as the half-layer termination (HLT) and full layer termination (FLT) structures. As shown in **Figure 33** (panels A and B), the FLT has only two types of surface functional groups (^IO and ^{III}O), while the HLT consists of three types of surface functional groups, including ^IO, ^{II}O and ^{III}O (left superscripts

are coordination number of O groups to the associated Fe atoms). Within the surface plane, the Fe-octahedra form a zig-zag pattern of surface atoms parallel to the b_s axis (**Figure 33 C and D**). The geometrical relationship between two adjacent Fe octahedral units can be described by b_s glide planes at $x = \frac{1}{4}$ and $\frac{3}{4}$ in the pseudo-orthorhombic surface unit cell. The surface oxygens (likely hydroxyl groups when hydrated) provide the potential binding sites for Pb(II) and Sb(V). By considering possible coordination geometries of Pb(II) and Sb(V) to these surface groups we generate initial models of the sorption complexes which are refined against the experimental data. The final result are the optimized models of the predominant sorption complexes present under the given experimental conditions.

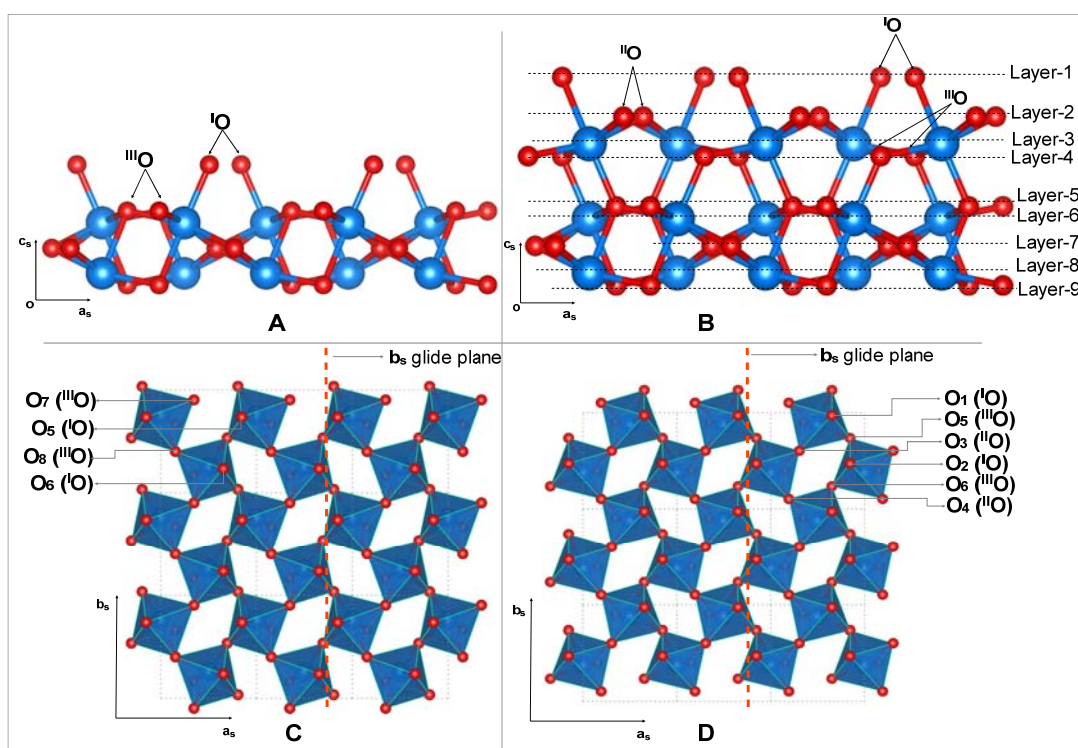


Figure 33. (A) Layer stacking sequence along the C_s axis for the full layer termination ($\bar{1}\bar{1}02$); (B) Layer stacking sequence along the C_s axis for the half layer termination ($\bar{1}\bar{1}02$); (C) polyhedral representation of the oxygen-terminated full layer termination surface of hematite ($\bar{1}\bar{1}02$) (second octahedral layer and those beneath are not shown for clarity) ; (D) polyhedral representation of the oxygen-terminated half layer termination surface of hematite ($\bar{1}\bar{1}02$) (second octahedral layer and those beneath are not shown for clarity). Lengths for unit cell edges are $a_s=5.035$ Å, $b_s=5.427$ Å and $c_s=7.364$ Å. The ^{III}O , ^{II}O , and IO represent oxygen triply, doubly and singly coordinated to iron, respectively. Each atom layer is labelled as “Layer-n E”, where n is integer from 1 and E is the element symbol for either O or Fe.

4.8.1 Pb(II) sorption

The list of potential binding models used in our analysis are provided in [Appendix A, Table A5](#). The models including one corner-sharing site and two edge-sharing sites for both the HLT and the FLT surfaces. Each model was run refined separately to optimize the sorption geometry and sorption site occupancy. We then refined the models allowing a mixture of potential binding sites. **Figure 34** shows the resulting best fit models versus the full CTR data set. Two models provided a reasonable fit to the data; model O5O7_O5O8 and O1O3_O1O4. Both of these models are based on the presences of multiple surfaces with predominantly edge sharing (ES) Pb(II). Of the two models O1O3_O1O4 resulted in the lowest figure of merit and is therefore the overall best fit model. This model results in a surface consisting of four terminations: 1) 19% Pb-bonded HLT with Pb(II) binding at the edge-sharing type 1 (ES1) site, i.e. O_1O_3 and the symmetry related site O_2O_{4+y} ; 2) 25% Pb-bonded HLT with Pb(II) binding at the edge-sharing type 2 (ES2) site, i.e. O_1O_4 site and the symmetry related site O_2O_{3+x} ; 3) 27% hydroxylated HLT; and 4) 29% hydroxylated FLT. The structural models of the sorption complexes are depicted in **Figure 35**.

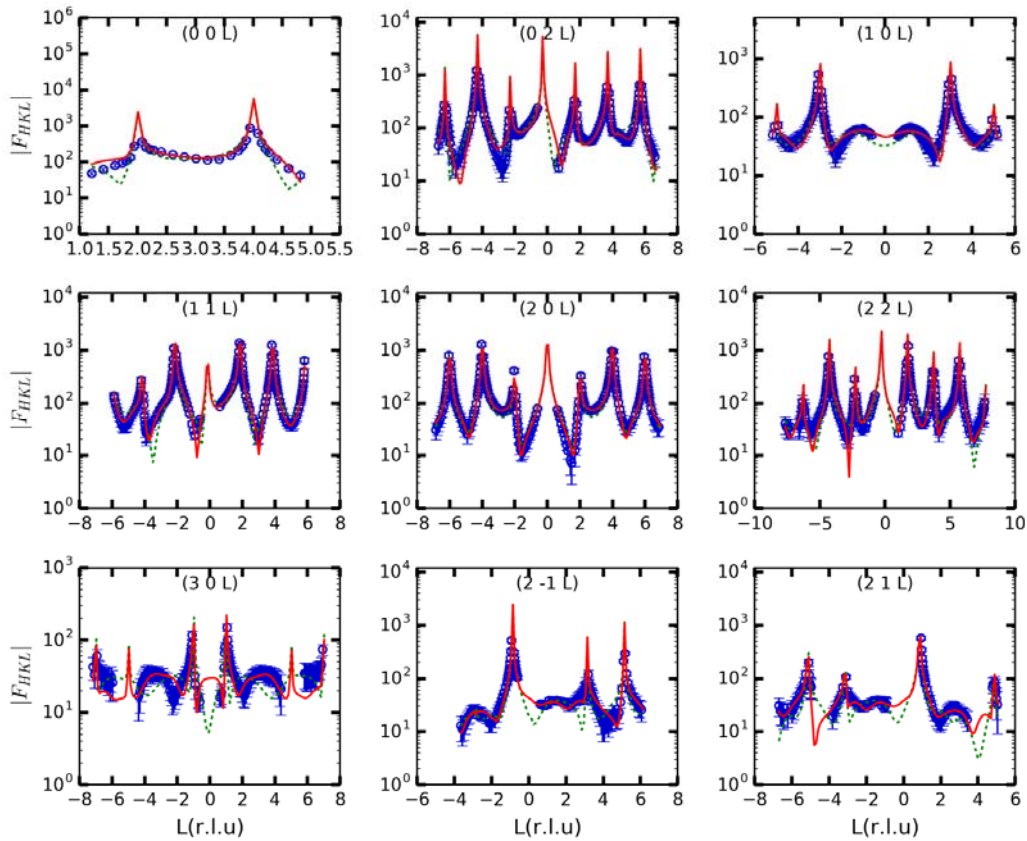


Figure 34. Experimental structure factors (F_{HKL}) as a function of perpendicular momentum transfer (L , in reciprocal lattice units) for the hematite ($\alpha\text{-Fe}_2\text{O}_3$); surface reacted with 200 μM Pb(II) at pH 5.5. The red solid lines represent the calculated CTR profiles based on the optimized model O1O3_O1O4 and the green dashed lines represent the calculated CTR profiles based on the optimized model O5O7_O5O8.

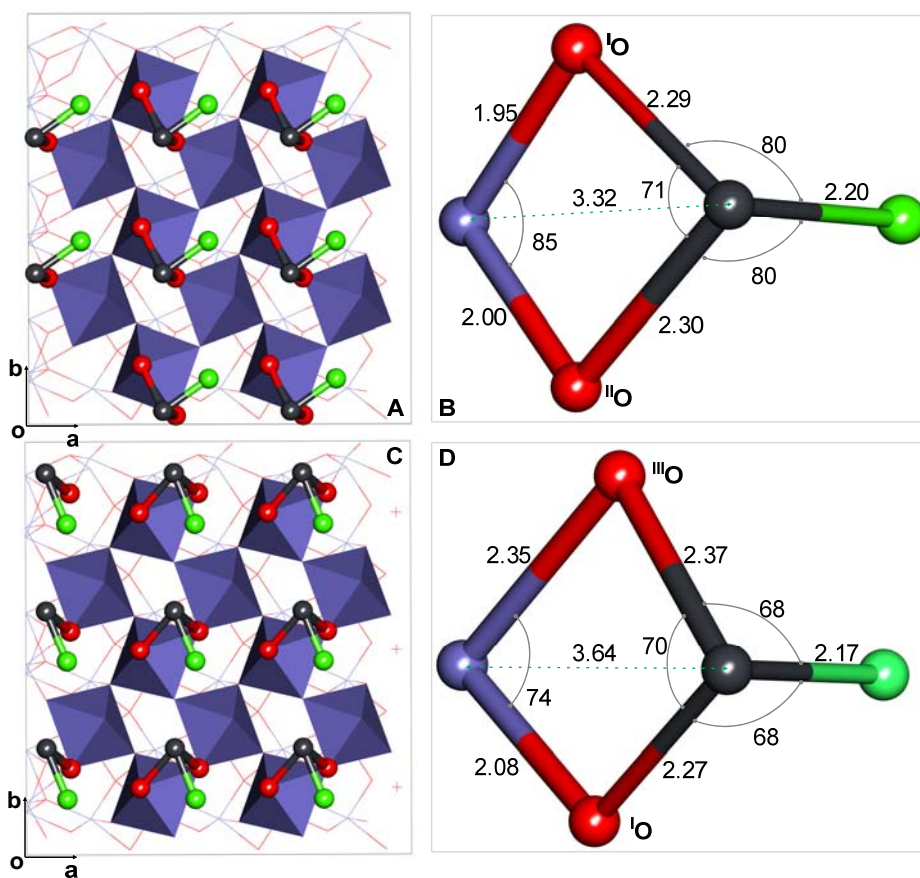
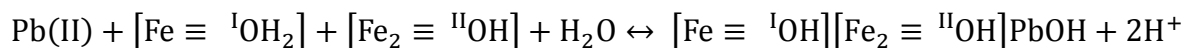


Figure 35. Structures of surface complex species with two types of edge-sharing binding configurations on the HLT based on the best fit model. The top view of the interfacial structure for Pb binding at site O_2O_{4+x} (A) and site O_2O_{3+x} (C) with the first Fe layer visualized as octahedra and the local structure of surface complex species as ball and stick models with green spheres representing distal oxygen, red spheres surface binding oxygen, and gray spheres Pb. Symmetry related sites are omitted for clarity. Detailed structural information for the surface complex species at site O1O3 (B) and site O1O4 (D) in terms of bond angles (°) and bond lengths (Å). The near neighbor Fe atoms (blue spheres) are shown as well.

The surface complex structures illustrated in **Figure 35** have average Pb-O bond lengths of 2.26 Å and 2.27 Å which are in good agreement with the value of 2.28 Å reported in previous XAFS studies (Bargar et al., 1997; 2004). The characteristic Pb-Fe separations are 3.32 Å and 3.64 Å corresponding to the ES1 site and the ES2 site, respectively. The XAFS study by Bargar et al. (1997) using a hematite powder sample suggested a single Pb-Fe distance of 3.28 Å, which is consistent with that for the ES1 site in the present study. The Pb-Fe distance of 3.64 Å is longer than those assigned to edge sharing binding sites in previous XAFS studies using powder samples (Bargar et al., 1997; Ostergren et al., 1999; Trivedi et al., 2003). However, this larger Fe-Pb separation is consistent with a smaller O-Fe-O bond angle for the ES2 site (74°) compared to the ES1 site (85°) as is shown in **Figure 35**.

The intrinsic b_s glide plane symmetry on the hematite ($1\bar{1}02$) plane determines that there are two symmetry related sites per surface unit cell for each type of surface site resulting in four edge sharing sites in total within one unit cell. In theory, all four sites within one unit cell could be occupied. However, this would result in severe steric hindrance due to physically implausible Pb-Pb distances. To study the steric constraints imposed by occupied sites, site coverage simulations were performed based on occupying available surface sites randomly with a set of predefined minimum inter-site distance cutoff limits. A 20×20 supercell was defined for each simulation using the positions derived from the best fit CTR model. The simulations were performed at Pb-Pb cutoff limits ranging from 2.84 Å to 10.08 Å which were identified from the site distribution pattern (**Figure 36A**). As illustrated in **Figure 36B**, the simulation results show, as expected, a trend of decreasing site coverage with increasing sorbate-sorbate cutoff limits. The experimental CTR derived occupancy of 0.75 Pb atoms per surface unit cell is in good agreement with the simulated site coverage corresponding to a cutoff of 5.42 Å (**Figure 36 B**). A representative site occupation pattern simulated at the 5.42 Å cutoff limit is illustrated in **Figure 36C**. We note that a cutoff limit of 5.42 Å is only slightly smaller than the lattice parameter b_s (5.43 Å), which indicates two adjacent occupied sites of the same type are allowed to be aligned in the y (b_s) direction. However, the case with two adjacent occupied sites aligned in the x (a_s) direction is forbidden at this cutoff since that would result in a sorbate-sorbate distance as short as 5.04 Å (the associated lattice parameter a_s). In addition, a cutoff limit of 5.42 Å could give rise to a coverage of one Pb per surface unit cell if a super lattice formed containing columns of occupied sites of two different types alternating along the x axis direction (An example is given in **Figure 36D**). However it appears that the sorption process results in less than a maximum sorption capacity due to the random nature of initial site occupancy.

Based on the best fit surface structural model we also propose protonation schemes for surface functional groups (using bond valence constraints) and propose an overall reaction stoichiometry for the sorption reactions. Following Tanwar et al. (2007b) ^{18}O groups, doubly protonated initially, would release one proton upon Pb(II) adsorption to the surface while the protonation state of the ^{16}O groups does not change after Pb(II) binding to the surface. The resulting reaction stoichiometry would then (for an initially protonated surface) be expressed as:



The stoichiometry proposed here suggests a strong dependency on solution pH, in agreement with observation.

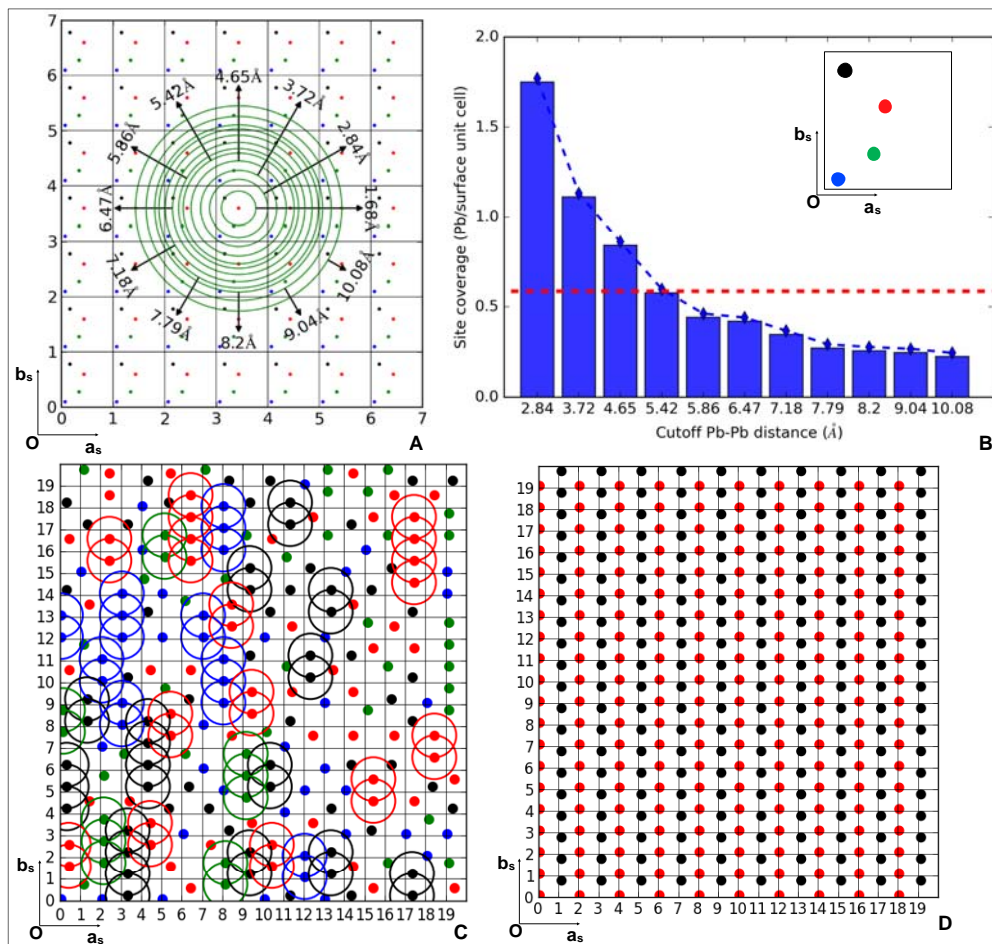


Figure 36. (A) Schematic showing inter-site distances identified from a fully occupied super cell. (B) The simulated site coverage (%) as a function of the Pb-Pb cutoff distances. The horizontal dashed line marks the CTR derived site occupancy. (C) Simulated site occupation pattern associated with a Pb-Pb cutoff distance of 5.42 Å, where the circles in different colors highlight the adjacent sites of same type aligned along b_s . (D) Maximum site occupation via super lattice formation satisfying the cutoff Pb-Pb distance of 5.42 Å.

4.8.2 Sb(V) sorption

An analogous study of possible Sb(V) binding sites and geometries on the hematite (1-102) surface was carried out. When considering possible binding sites we ignored the monodentate binding mode since it was not observed in previous XAFS studies (Scheinost et al., 2006; Mitsunobu et al., 2010b; Guo et al., 2014). In addition, we observe that Sb(V) adsorption at the bidentate edge-sharing sites would lead to extremely small O-O separations (<2.0 Å) between the distal oxygens (bonding to Sb only) and the substrate surface oxygens. Therefore, these sites were also excluded from surface modeling due to the steric constraints we imposed on the sorbate (O-O separation greater than 2.5 Å). As a result, the surface modeling in the current study was limited to six trial models (Appendix A, Table A6) corresponding to bidentate corner-sharing, tridentate corner-sharing/edge-sharing and tridentate face-sharing binding configurations on both the HLT and the FLT surfaces. Note that each site consists of two symmetry related sites due to the presence of the b_1 glide plane symmetry at the surface. To distinguish different surface sites, we gave each site a unique name by concatenating labels for the constituent surface oxygens. Each unique surface oxygen was distinguished using a subscript integer starting from 1. The associated in-plane translation symmetry operation was defined by suffixing the number with “ $\pm x$ ” or “ $\pm y$ ” to label the translation along x or y axis.

The CTR measurements were performed at three Sb(V) concentrations, including 50, 200 and 400 μM . The CTRs for 200 and 400 μM were comparable within experimental errors suggesting a surface site saturation of Sb(V) on the substrate surface was achieved at 200 μM . Modeling was carried out using the 200 μM data set.

As with Pb, several scenarios needed to be considered for Sb binding at the possible sites on the two distinct surface terminations. Structural models with Sb(V) binding on the FLT include bidentate corner-sharing (Model1), tridentate corner-sharing/edge-sharing (Model2), and tridentate face-sharing (Model3) binding configurations. Refinement and comparison of the data versus the computed structure factors showed that none of these models were able to reproduce the data. Therefore we conclude that Sb(V) purely associated with the FLT surface does not provide a good fit to the data and we need to consider Sb(V) on the HLT as well. Analogous to the cases of Sb-bonded FLT, we developed three models (Model4, Model5 and Model6) to consider Sb(V) sorption to the HLT surface with three different binding configurations. Of these models we observe that both Model4 and Model5 yielded a good fit to the experimental data (Figure 37). However, the fit based on Model4 generated a large FOM due to unrealistic small separations between distal oxygens and surface oxygens (<2.5 Å). Thus, Model5 is the only model we tested that was capable of reproducing the CTR intensity and provided reasonable structure during model refinement. Further analysis of Model5 including Sb binding to the FLT led to no improvement in the fit, with large uncertainties in the Sb site occupancy on the FLT. Therefore we propose that Model5 best describes the predominant binding mode of Sb(V) on the hematite (1-102) surface.

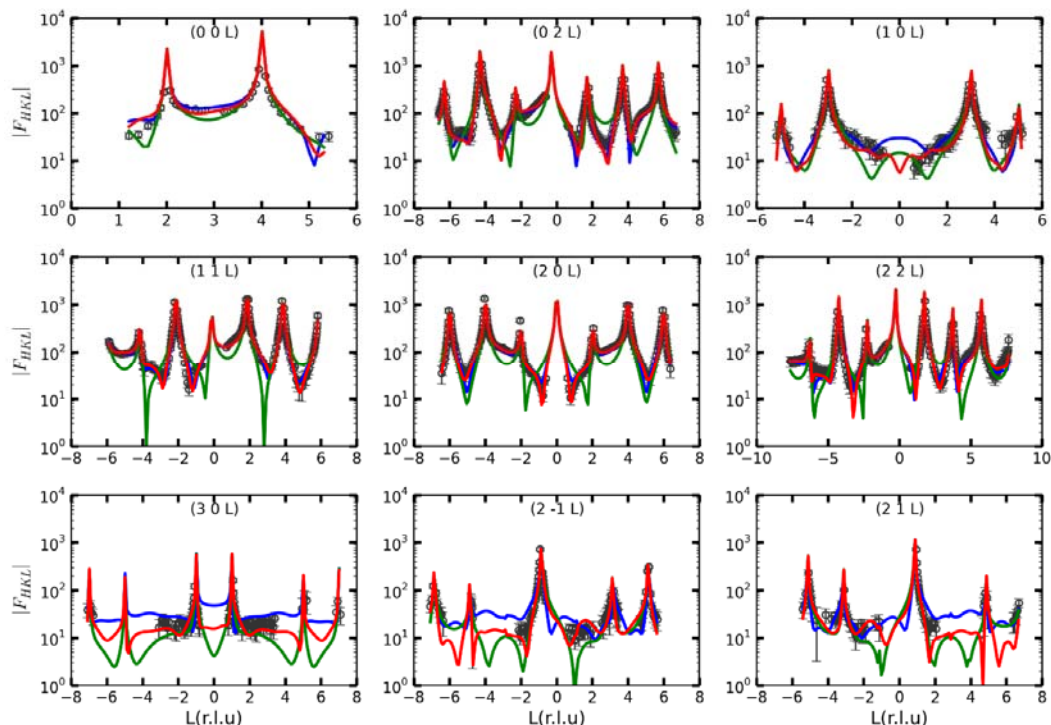


Figure 37. Experimental (gray circles) and model-based structure factors (F_{HKL}) as a function of perpendicular momentum transfer (L , in reciprocal lattice units) for the hematite () surface reacted with 200 μM Sb(V) at pH 5.5. The solid lines in green represent the calculated CTR profiles based on the best fit model Model4, solid lines in blue represent the calculated CTR profiles based on the best fit model Model6, and solid lines in red represent the calculated CTR profiles based on the best fit model Model5.

The best fit model resulted in a surface structure with a 22% clean FLT surface and a 78% HLT surface. The HLT surface was partially occupied by Sb (0.74 mono-layer coverage). The proportion of FLT to HLT was in good agreement with what was reported in a previous study of a similarly prepared substrate ((72/28 HLT/FLT; Tanwar et al., 2007). As shown in **Figure 38**, the best fit structural model generated a Sb surface complex binding at the HLT surface in a tridentate mode with a corner-sharing/edge-sharing binding configuration. The Sb surface complex is a distorted octahedron with asymmetric Sb-O bond lengths (2.00 Å \times 3, 2.05 Å, 2.15 Å and 2.21 Å) and a nearest Sb-Fe separation of 3.05 Å. The Sb-Fe separation derived in our CTR study (3.05 Å) is in good agreement with those resulting from XAFS spectroscopy studies (3.00-3.19 Å) of Sb(V) sorbed to a range of different powdered synthetic substrates, including goethite (Mitsunobu et al., 2010b), ferrihydrite (Mitsunobu et al., 2010b) hydrous ferric oxide (Guo et al., 2014), and environmental samples (Scheinost et al., 2006; Ritchie et al., 2013).

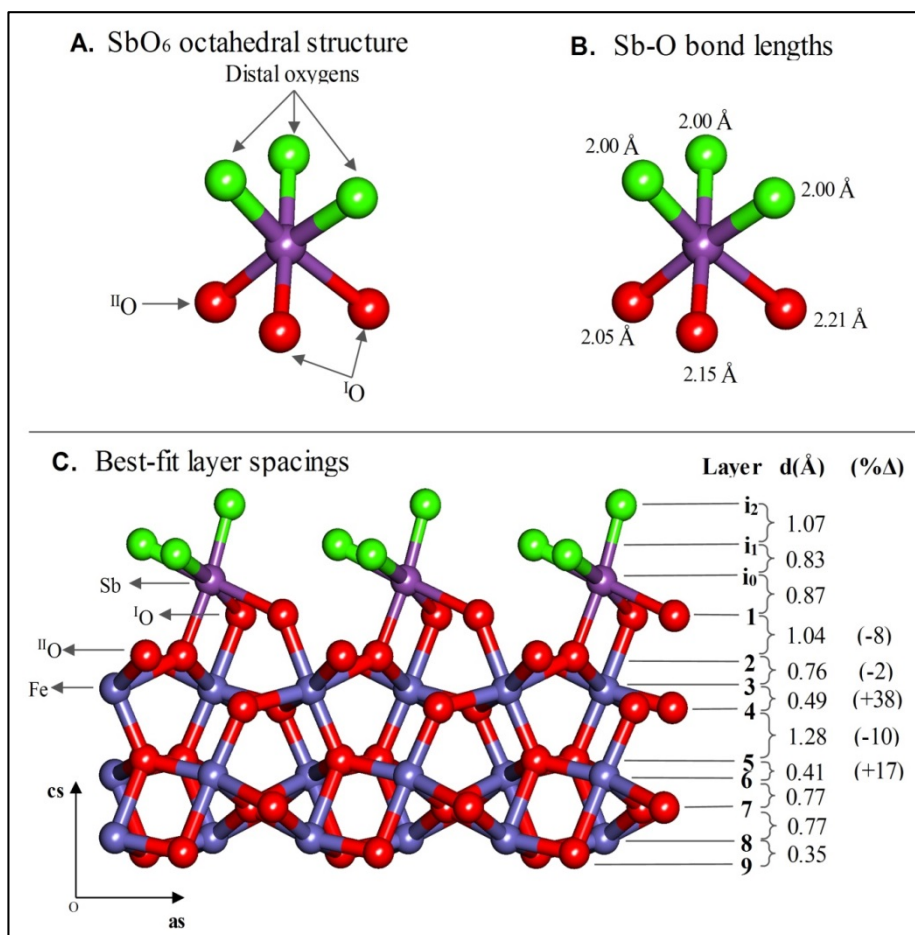
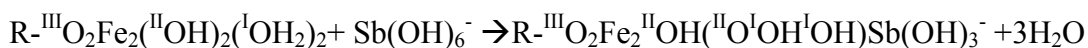


Figure 38. (A) Octahedral local structure of the Sb(V) surface complex in the best fit model structure. (B) bond lengths of the Sb(V) surface complex. (C) Surface binding structure and atomic layer spacing values for Sb(V) sorbed to the half layer termination based on the best fit model structure for Model5.

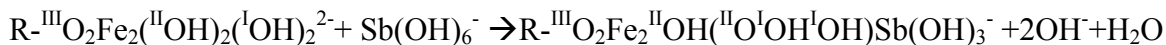
The distortion of the Sb(V) octahedral coordination arises from two relatively long Sb-O bonds associating with the ^IO groups, compared to the Sb-O bond associating with the ^{II}O group and the three associated with distal oxygens that are nearly equivalent in length (~2.0 Å). We suggest that this distortion is associated with maintaining an Sb-Fe separation distance that reduces unfavorable cation-cation interactions. Hence, in our system, it appears the energy cost associated with placing Sb closer to the Fe exceeds that arising from the distortion in Sb-O bond lengths. Similar findings were found in our previous theoretical study of Sb(V) binding on the hematite (0 0 0 1) (Mason et al., 2012). In that study, we observed a site preference trend in which the larger Sb-Fe separation corresponded to the more energetically favorable site. The electrostatic repulsion between Sb and Fe was also highlighted by Bolanz et al. (2013), who

studied the substitution of Sb(V) in structural Fe(III) sites during the transformation of 2-line ferrihydrite to hematite, goethite and ferroxhyte. The authors proposed a mechanism of isomorphic substitution of Sb(V) for Fe(III) in goethite and ferroxhyte while they claimed the strong electrostatic repulsion should significantly impede the isomorphic substitution of Sb(V) in hematite due to the short cation-cation separation ($<3.0 \text{ \AA}$) associated with the face-sharing octahedral units. Similar findings were reported by Mitsunobu et al. (2013), who highlight that the immobilization of Sb(V) through substitution during the process of transforming ferrihydrite to more crystalline iron oxy(hydr)oxide products could be more effective than pure surface adsorption.

Similar to our analysis of the Pb reacted surface, we use predicted protonation schemes of surface oxygen groups on the Sb reacted surface to deduce an adsorption reaction stiochiometry:



Interestingly, the stoichiometry outlined above does not predict any proton/hydroxyl release, which implies a pH independence of Sb(V) adsorption on the hematite surface. However, if we consider that singly protonated $^{\text{I}}\text{O}$ groups are likely to be predominate at higher pH, the stoichiometry can be re-written as:



In this scenario, due to the production of OH^- , a higher solution pH will favor the reactants leading to the desorption of Sb(V) under alkaline conditions. This is consistent with the pH adsorption edge results presented in previous studies using different types of Fe-(oxy)hydroxide samples (Leuz et al., 2006; Martínez-Lladó et al., 2008; Vithanage et al., 2013), which showed a maximum uptake at low pH but a decline of uptake at a higher pH. Considering the relatively high pH (7-9) of the point of zero charge on hematite substrates (Kosmulski, 2011), the surface functional groups on the HLT are likely fully protonated at pH 5.5 consistent with that shown in the first stoichiometry discussed above.

4.9 Substrates as passive sensors

Following on our laboratory studies of metal(loid) sorption to clean highly polished single crystal substrates, we wanted to test the idea if these could be used as passive sensors in real soil systems. Such sensors may be placed in berm soils and help to monitor geochemical conditions pertinent to weathering of fresh metallic surfaces and to giving a qualitative indication of the lability of oxidized metal(loid)s originating from the weathered bullet fragments. Outcomes of our controlled laboratory experiments with metallic Sb and Pb indicate that temporal evolution on the scale of days and months can be characterized by large, hard-to-predict changes in solid and liquid phase speciation. On this time scale, in-situ monitoring can provide a more realistic outlook of the fate of metal(loid)s from spent bullets in soils of impact berms at shooting ranges. We used

two types of passive sensors: polycrystalline Sb metal chips and single surface hematite crystals (**Figure 39**). All sensors were highly polished and their working surfaces were probed with a combination of in-house techniques like SEM, grazing incidence XRD (GI-XRD) and atomic force microscopy, and a suite of synchrotron-based x-ray scattering and spectroscopy techniques, high resolution x-ray reflectivity (XR), and grazing incidence angle measurements such as fluorescent yield (GI-FY), GI-XAFS and GI-XRD. Sensors were deployed into soils of our newly constructed berms, both contaminated and uncontaminated (field control), at our field site for a period of one to two months. Working surfaces were oriented down with respect to the surface of the berms to limit deposition of suspended solids with gravitational flow. Sensors were isolated from direct contact with soil by a non-reactive envelope of either acid washed, ignited quartz (SiO_2) sand or acid washed PTFE beads (**Figure 39**).

Surfaces of the passive sensors evolved in the course of the field deployment as determined by in-house SEM measurements. The presence of calcium carbonate (CaCO_3) on the surfaces of sensors deployed in the sandy berms was predicted as the soil pore water is in apparent equilibrium with CaCO_3 as indicated by its high pH. However, phyllosilicate minerals such as muscovite $[\text{KAl}_2(\text{Si}_3\text{Al})\text{O}_{10}(\text{OH})_2]$ and clinocllore $[(\text{Mg}_5\text{Al})(\text{Si}_3\text{Al})\text{O}_{10}(\text{OH})_8]$ were not predicted on such surfaces because these are constituents of our other textural end member, the loamy soil. Their observation in SEM measurements led us to hypothesize that dust particles, derived from local loamy soil, were deposited on the surface of the sandy berms and were transported with percolating rain water in colloidal suspension laterally to the surfaces of the passive sensors. Since attached colloids, and carbonate and oxide precipitates could potentially block (or compete for) Pb and Sb reactive sites on the working surfaces we applied synchrotron based GI-FY

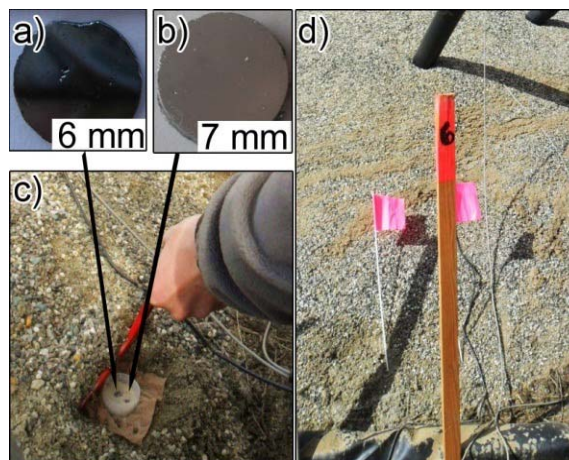


Figure 39. Field deployment of (a) single crystal hematite ($\alpha\text{-Fe}_2\text{O}_3$) and (b) polished antimony metal chip in (c) acid washed quartz (SiO_2) sand; (d) samples were reacted for 30 days.

measurements to determine vertical distribution of the elements ($Z \geq 14$), including Pb and Sb, above the working surfaces.

Using GI-FY element distributions are determined from the shape of the fluorescence yield curve with respect to the position of the critical angle for the substrate (below the critical angle the substrate acts as a perfect mirror, with effectively 100% reflectivity) (**Figure 40**). Iron and chromium (Cr) fluorescent yields increase steeply above the critical angle as x-rays of the incident beam interacted with an increasingly larger volume of the bulk substrate at higher incidence angles. These profiles are characteristic of an element contained within the “bulk” of the substrate (i.e. Fe oxide with some Cr substitution for Fe). Therefore, the hematite substrate is not suitable for probing Fe or Cr associated with transport from soil solution to the surface due to these (relatively) high background signals. However, we observe that the fluorescent yields of Cu, Zn and Pb are peaked sharply at the critical angle which is indicative of surface limited sequestration as expected for adsorption from soil solution. Subsequent GI-XAFS verified the presence of Pb in the +2 oxidation state, possibly in the form of carbonate complexes (data not shown). This observation indicates that (oxidized) metals from the soil solution were transported to the surface of the substrate, and indicate that these metals are labile in the soil solution as dissolved/reactive species.

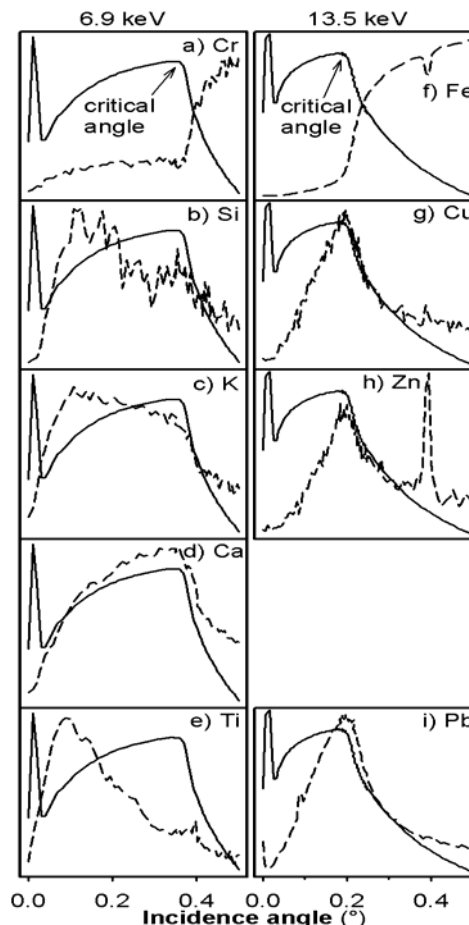


Figure 40. Fluorescence yield for the surface of a single surface hematite (α -Fe₂O₃) crystal after 30-day deployment in the contaminated soil of a newly constructed berm. Fluorescence data (dashed) are contrasted with the surface x-ray reflectivity (solid). Concurrent measurements were conducted at two beam energies, 6.9 and 13.5 keV, at GSECARS, Advanced Photon Source, Chicago, IL.

The broader more asymmetric fluorescent yield curve of Ca is indicative of a broad elemental distribution in the direction normal to the substrate surface. This yield is associated with fine-grained precipitates or colloids on the substrate surface. Further, we observe that silicon (Si) and potassium (K) curves also show broad distribution indicating their likely association with minerals like muscovite, clinochlore and/or quartz, associated with the substrate surface.

Titanium (Ti) appears to reside well above the substrate surface, due to the low angle peak, which may be indicative of large, uniformly-sized Ti-bearing colloids.

The most important finding of this study is that the working surface of the single crystal hematite passive sensor seems to maintain its reactivity towards Cu, Zn, and Pb during field deployment despite attachment of colloids and precipitation of carbonates – in other words the intrinsic reactivity of the substrate is not altered under environmental conditions, including due to accumulation of colloidal phases at the substrate interface – a key trait for suitability as a passive sensor. As noted above, these results indicate that these metals are labile as “reactive” species within soil solution, giving a qualitative indication of metal lability, and indicating that sorption to mineral surfaces is a significant retardation mechanism. Furthermore, we note that “capturing” these metals on the substrate surface allows for additional speciation analysis as for example in the case of Pb in which we used surface sensitive XAFS analysis to identify it as being fully oxidized.

5. Conclusions and Implications for Future Research/Implementation

The findings of this project show that initial oxidation of Pb and Sb metals associated with bullets deposited in berm soils is rapid. As observed at the field site within the first 3 months there is extensive oxidation and mobilization of metals which has persisted through duration of the project. Furthermore, we observe that although Sb is present at roughly 1wt% in the bullet matrix the aqueous concentrations of Sb in the soil pore waters are generally greater than the dissolved Pb concentrations. Thus we conclude that Sb is generally much more mobile than Pb in the test soils. We also found that the aqueous Sb was predominantly Sb(V) in the soil solutions, with only traces of Sb(III) observed in more organic rich soils at very early oxidation times. Our field observations also show that there was little variation in the average Pb concentrations based on soil type, whereas aqueous concentrations of Sb appear to be elevated in the more sand rich (and higher pH) soils. We suggest that the small variation in Pb concentrations is likely linked to the fact the secondary mineral phases, including PbCO_3 and PbO , are controlling the release of Pb to solution rather than direction from the metallic bullet surfaces. Nevertheless sorption processes are an important mechanism of Pb retention within the soil matrix, and we qualitatively observe increasing fractions of “sorbed-Pb” over time. On the other hand Sb oxidizes rapidly at the bullet / solution interface possibly forming a transient Sb(III) oxide phase that is highly susceptible to dissolution and further oxidation – except in the rare occurrences where the initial oxidation occurs within a “protected pocket” where the Sb(III) phase may be preserved (possibly as an Sb(V) oxide). Sorption is also an important retention mechanism for Sb, but at the higher pH’s of these soil systems, it is not an effective barrier to mobility for any of the soil types examined. These processes are summarized in **Figure 41**.

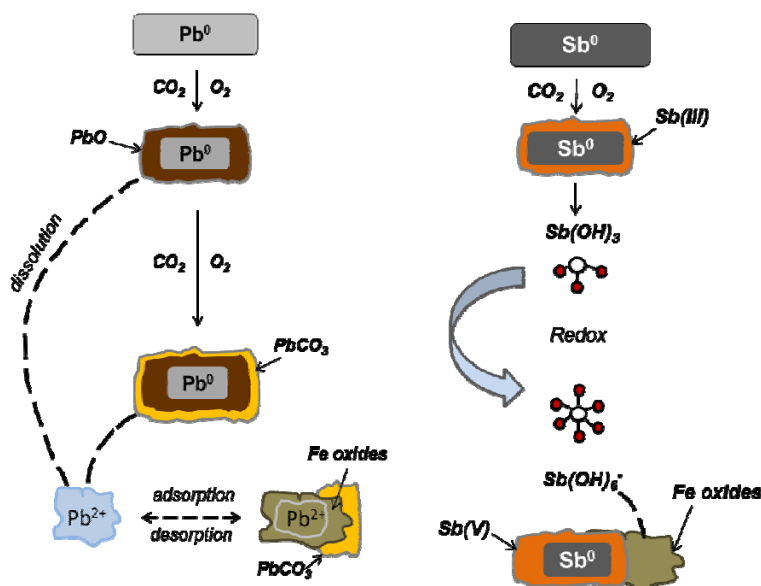


Figure 41. Simplified conceptual model of key processes controlling the mobilization of Pb and Sb within the berm soils.

Our laboratory measurements generally help to guide our interpretation of the field observations. We found that the laboratory oxidation and dissolution of Sb(0) is very rapid. There is always an initial release of Sb(III), but this is relatively rapidly oxidized to Sb(V). The second oxidation is strongly dependant on solution conditions and it appears that organic ligands help preserve the more reduced form of Sb. We also observe that the initial dissolved concentrations exceed the solubility of expected Sb secondary oxides. Over time it appears that the oxides do ultimately control Sb solubility, with laboratory measurements showing that ultimate phase that forms is highly sensitive to pH and solution composition. The current scarcity of thermodynamic data for these phases makes prediction difficult.

Our laboratory column studies point show that saturation time is, in most cases, an important variable to consider. Short exposure times result in rapid increases of dissolved metals that tend to plateau after roughly a day of reaction time. This has important implications for berm soils, which are typically subject to short term saturating rain event followed by flushing of the pore waters. This shows that even short contact times with a dry soil can lead to a significant plug of metal rich waters. The column studies also showed that the use of an iron-oxide type amendment is potentially highly effective at sequestering Sb, but results in a “plug” of elevated Pb concentrations. These results can be traced back primarily to the changes in pH associated with the treatments. Finally the column studies also point out the importance of colloid facilitated transport, particularly for the mobility of Pb within these soils. The results indicate that while most of the “apparently dissolved” Sb is truly dissolved, this is not the case for Pb. The key colloids for Pb transport are iron oxides.

Our study of the historic berms points to potential long(er) term fate of the young shooting range berms. These studies show that after many years the Pb-carbonates are the primary weathering phase associated with the metals, and that “oxidation rind” can be many tens of microns thick. Distal to the weathering products the soil contains significant fractions of sorbed Pb. The speciation of the Sb was dominated by Sb-Fe sorption complexes. While we did observe the presence of and Sb(III) secondary phase, this was again likely a transient that occur within a protected pocket.

The results of our sorption studies on well characterized iron-oxide substrates provide new details on the stoichiometry and structure of the important Pb and Sb surface species present at the mineral-fluid interface. In both cases we observe that strong inner-sphere complexes are formed, and that the local structure of the sorption complex is dependant on the types of surface functional groups exposed to the solution. This latter point is an important illustration of the importance of the affinity of certain reactive sites for binding particular metal(oids) and the influence of steric effects. Another important observation from these studies is the limit in maximal uptake to less than a complete mono-layer. During the sorption process, reactive sites are filled at random. However, there is a sorbate-sorbate interaction that limits certain neighboring sites from being occupied, and hence these interaction limit overall uptake. Finally we show that we can translate these systems from the laboratory to the field and use these types of substrates as passive sensors. The highly reactive nature of the Fe-oxide surfaces in particular make them a useful (qualitative) indicator of free metal(loid) mobility by observing the presence of sorbed species at the surface after deployment. The GI-FY methods also allows for the discrimination between truly sorbed species and those associated with colloid adhesion.

Ultimately the goal of this study is generate information useful to land managers in understanding the fate of Pb and Sb in shooting ranges. We can summarize the main points of the study by saying that (i) metal(loid) oxidation is rapid and releases significant Pb and Sb to soil solution regardless of soil type; (ii) Sb appears to be much more mobile than Pb, although somewhat less so in organic rich soils; (iii) the distinct differences in mobility are in part due to the fact that Pb weathering products include stable mineral phases such as Pb-carbonates adjacent to deposited metals while there is little evidence for secondary Sb phases, and Pb appears to have a greater sorption affinity with respect to soil particles than Sb; and (iv) while sorption processes are an important retention mechanism, the process is highly pH sensitive and Pb and Sb have contrary trends with pH. This latter point is especially born out in our test of iron amendments to limit Pb and Sb mobility. A system buffered to a high pH will have some limited enhancement of Pb sequestration but have little effect of Sb concentrations. The iron amendments that were less buffered were very effective at the sequestration of Sb, but of course came with large pulses of Pb (and other cations) being released to solution. This results in the direct application of a “soil treatment” of this type very difficult. Therefore, as a recommendation for future work we suggest that one possible route to investigate is a two stage treatment of berm runoff, in which an iron-oxide bed, buffered to a lower pH is used to remove Sb, followed by a carbonate buffered iron-oxide bed to remove cations.

6. Literature Cited

- Ackermann, S., R. Gieré, M. Newville, and J. Majzlan (2009) Antimony sinks in the weathering crust of bullets from Swiss shooting ranges. *Science of the Total Environment* **407**, 1669–1682.
- Ahmad, M.; Lee, S.S.; Lim, J.E.; Lee, S.E., Cho, J.S.; Moon, D.H.; Hashimoto, Y.; Ok, Y.S. (2014) Speciation and phytoavailability of lead and antimony in a small arms range soil amended with mussel shell, cow bone and biochar: EXAFS spectroscopy and chemical extractions. *Chemosphere*, **95**, 433–441.
- Allison, J.D., D.S. Brown, and K.J. Novo-Gradac (1991) MINTEQA2/PRODEFA2, A geochemical assessment model for environmental systems. U.S. Environmental Protection Agency, Athens, GA.
- Andreae, M.O., J.-F. Asmode, P. Foster, L. Van't dack (1981) Determination of antimony (III), antimony (V), and methylantimony species in natural waters by atomic absorption spectrometry with hydride generation. *Analytical Chemistry* **53**, 1766–1771.
- Astrup, T., J.K. Boddum, and T.H. Christensen (1999) Lead distribution and mobility in a soil embankment used as a bullet stop at a shooting range. *Journal of Soil Contamination* **8**, 653–665.
- Bagby, E.L. and West, C.M. (1995) Treatment of an anionic metal by adsorption on iron oxides. In *Emerging Technologies in Hazardous Waste Management V*, Tedder, D.W.; Pohland, F.G., Eds.; American Chemical Society: Washington, DC, **607**, 64–73.
- Bargar, J.R., S.N. Towle, G.E. Brown, Jr., and G.A. Parks (1996) Outer-sphere Pb(II) adsorbed at specific surface sites on single crystal γ -alumina. *Geochimica et Cosmochimica Acta* **60**, 3541–3547.
- Bargar, J.R., G.E. Brown, Jr., and G.A. Parks (1997) Surface complexation of Pb(II) at oxide-water interfaces: II. XAFS and bond-valence determination of mononuclear Pb(II) sorption products and surface functional groups on iron oxides. *Geochimica et Cosmochimica Acta* **61**, 2639–2652.
- Bargar, J.R., T.P. Trainor, J.P. Fitts, S.A. Chambers, and G.E. Brown, Jr. (2004) Surface complexation of Pb(II) on single crystal hematite surfaces: A grazing incidence XAFS study. *Langmuir* **20**, 1667–1673.
- Basunia, S., Landsberger, S. (2001) Contents and leachability of heavy metals (Pb, Cu, Sb, Zn, As) in soil at the Pantex firing range, Amarillo, Texas, *Air Waste Manage. Assoc.* **51**, 1428–1435.
- Bedzyk, M.J., and L. Cheng (2002) X-ray standing wave studies of minerals and mineral surfaces: Principles and applications. *Reviews in Mineralogy and Geochemistry* **49**, 221–266.
- Belzile, N., Chen, Y.W., Wang, Z. (2001) Oxidation of antimony (III) by amorphous iron and manganese oxyhydroxides. *Chemical Geology*, **174**, 379–387.

Bencze, K., (1994) Antimony. *In* Seiler, H.G., A. Sigel, and H. Sigel (Eds.), *Handbook on Metals in Clinical and Analytical Chemistry*. Marcel Dekker, New York, pp. 227–236.

Björck, M., and G. Andersson (2007) GenX: An extensible x-ray reflectivity refinement program utilizing differential evolution. *Journal of Applied Crystallography* **40**, 1174–1178.

Bolanz R. M., Blaess U., Ackermann S., Ciobota V., Roesch P., Tarcea N., Popp J. and Majzlan J. (2013) The effect of antimonate, arsenate, and phosphate on the transformation of ferrihydrite to goethite, hematite, feroxyhyte, and tripuyhyte. *Clays Clay Miner.* **61**, 11–25.

Briggs, P.H., and A.L. Meier (2002) The determination of forty-two elements in geological and botanical samples by inductively coupled plasma-mass spectrometry. *In* Taggart, J.E. (Ed.) *Analytical methods for chemical analysis of geologic and other materials*, U.S. Geological Survey, Open-file Report 02–223, pp. I1–I14.

Bridges, T., et al. (2008) SERDP and ESTCP expert panel workshop on research and development needs for understanding & assessing the bioavailability of contaminants in soils and sediments. Strategic Environmental Research and Development Program, Environmental Security Technology Certification Program, Arlington, VA.

Brown G.E. Jr., Henrich, V.E., Casey, W.H., Clark, D.L., Eggleston, C., Felmy, A., Goodman, D.W., Grätzel, M., Maciel, G., McCarthy, M.I., Nealson, K.H., Sverjensky, D.A., Toney, M.F., Zachara, J.M., (1999a) Metal oxide surfaces and their interactions with aqueous solutions and microbial organisms. *Chemical Reviews* **99**, 77–174.

Brown, G.E., Jr., A.L. Foster, and J.D. Ostergren (1999b) Mineral surfaces and bioavailability of heavy metals: A molecular-scale perspective. *Proceedings of the National Academy of Sciences of the USA* **96**, 3388–3395.

Brown, G.E. Jr., T.P. Trainor, and A.M. Chaka (2007) Geochemistry of mineral surfaces and factors affecting their chemical reactivity. *In* Nilsson, A., L. Pettersson, and J. Norskov (Eds.) *Chemical Bonding at Surfaces and Interfaces*, Elsevier, New York, pp. 457–509.

Brown, Z., and K.J. Curry (2002) Total carbon by combustion. *In* Taggart, J.E. (Ed.) *Analytical methods for chemical analysis of geologic and other materials*, U.S. Geological Survey, Open-file Report 02–223, pp.R1–R4.

Cao, X., L.Q. Ma, M. Chen, D.W. Hardison, Jr., and W.G. Harris (2003a) Weathering of lead bullets and their environmental effects at outdoor shooting ranges. *Journal of Environmental Quality* **32**, 526–534.

Cao, X., L.Q. Ma, M. Chen, D.W. Hardison, Jr., and W.G. Harris (2003b) Lead transformation and distribution in the soils of shooting ranges in Florida, USA. *Science of the Total Environment* **307**, 179–189.

Catalano J. G., Fenter P. and Park C. (2007) Interfacial water structure on the (0 1 2) surface of hematite: Ordering and reactivity in comparison with corundum. *Geochim. Cosmochim. Acta* **71**, 5313–5324.

Catalano J. G., Fenter P. and Park C. (2009) Water ordering and surface relaxations at the hematite (110)--water interface. *Geochim. Cosmochim. Acta* **73**, 2242–2251.

Catalano J. G. (2010) Relaxations and Interfacial Water Ordering at the Corundum (110) Surface. *J. Phys. Chem. C* **114**, 6624–6630.

Ceriotti, G., and D. Amarasiriwardena (2009) A study of antimony complexed to soil-derived humic acids and inorganic antimony species along a Massachusetts highway. *Microchemical Journal* **91**, 58–93.

Chen, M., S.H. Daroub, L.Q. Ma, W.G. Harris, and X. Cao (2002) Characterization of lead in soils of a rifle/pistol shooting range in central Florida, USA. *Soil and Sediment Contamination* **11**, 1–17

Cheng L., Fenter P., Nagy K. L., Schlegel M. L. and Sturchio N. C. (2001) Molecular-scale density oscillations in water adjacent to a mica surface. *Phys. Rev. Lett.* **87**, 156103.

Clausen, J., J. Robb, D. Curry, and N. Korte (2004) A case study of contaminants on military ranges: Camp Edwards, Massachusetts, USA. *Environmental Pollution* **129**, 13–21.

Clausen, J.L., Bostick, B., Korte, N. (2011). Migration of Lead in Surface Water, Pore Water, and Groundwater With a Focus on Firing Ranges. *Critical Reviews in Environmental Science and Technology*, **41**, 15, 1397-1448.

Conesa, H.M., Wieser, M., Gasser, M., Hockmann, K., Evangelou, M.W.H., Studer, B., Schulin, R. (2010) Effects of three amendments on extractability and fractionation of Pb, Cu, Ni and Sb in two shooting range soils. *Journal of Hazardous Materials*, **181**, 845-850.

Cornell R. M. and Schwertmann U. (2003) *The iron oxides: structure, properties, reactions, occurrences and uses.*, John Wiley & Sons.

Craig, J.R., J.D. Rimstidt, C.A. Bonnaffon, T.K. Collins, and P.F. Scanlon (1999) Surface water transport of lead at a shooting range. *Bulletin of Environmental Contamination and Toxicology* **63**, 312–319.

Creed, J., C. Brockhoff, T. Martin (1994) EPA method 200.8, Revision 5.4 Determination of trace elements in waters and wastes by inductively coupled plasma - mass spectrometry. United States Environmental Protection Agency.

Defense Ammunition Center (DAC), Munitions Items Disposition Action System (MIDAS). Detailed Structure for CTG 5.56 mm Ball M855.

- de Boer, D.K.G. (1991) Glancing-incidence x-ray fluorescence of layered materials. *Physical Review B* **44**, 498–511.
- Diemar, G.A., M. Filella, P. Leverett, and P.A. Williams (2009) Dispersion of antimony from oxidizing ore deposits. *Pure and Applied Chemistry* **81**, 1547.
- Dorjee, P., Amarasiriwardena, D., Xing, B. (2014). Antimony adsorption by zero-valent iron nanoparticles (nZVI): Ion chromatography-inductively coupled plasma mass spectrometry (IC-ICP-MS) study. *Microchemical Journal*, **116**, 15-23.
- Duggan, J., and A. Dhawan (2007) Speciation and vertical distribution of lead and lead shot in soils at a recreational firing range. *Soil and Sediment Contamination* **16**, 351–369.
- Dzombak, D.A. and Morel, F. M. M. (1990) Surface Complexation Modeling, Hydrous Ferric Oxide; John Wiley & Sons: New York.
- Elzahabi, M.; Yong, R.N. (2001) pH Influence on sorption characteristics of heavy metal in the vadose zone. *Engineering Geology*, **60**, 61-68.
- Eng P.J., T.P. Trainor, G.E. Brown Jr., G.A. Waychunas, M. Newville, S. Sutton, and M. Rivers (2000) Structure of the Hydrated γ -Al₂O₃ (0001) Surface. *Science* **288**, 1029–1033.
- Exponent (2005) Final technical report: Development of extraction tests for determining the bioavailability of metals in soil: SERDP Project Number CU-1165.
- Fendorf, S., M.J. Eick, P. Grossl, and D.L. Sparks (1997). Arsenate and chromate retention mechanisms on goethite. *Environmental Science and Technology* **31**, 315–320.
- Fenter, P.A. (2002) X-ray reflectivity as a probe of mineral-fluid interfaces: A user guide. *Reviews in Mineralogy and Geochemistry* **49**, 149–220.
- Fenter, P.A., and N.C. Sturchio (2004) Mineral–water interfacial structures revealed by synchrotron x-ray scattering. *Progress in Surface Science* **77**, 171–258.
- Filella, M., N. Belzile, and Y.W. Chen (2002) Antimony in the environment: A review focused on natural waters I. Occurrence. *Earth-Science Reviews* **57**, 125–176.
- Filella, M., N. Belzile, and Y.W. Chen (2002) Antimony in the environment: A review focused on natural waters II. Relevant solution chemistry. *Earth-Science Reviews* **59**, 265–285.
- Garten, C.T., Jr., T.L. Ashwood, and V.H. Dale (2003) Effect of military training on indicators of soil quality at Fort Benning, Georgia. *Ecological Indicators* **3**, 171–179.
- Geissbühler P., Fenter P., DiMasi E., Srajer G., Sorensen L. B. and Sturchio N. C. (2004) Three-dimensional structure of the calcite--water interface by surface X-ray scattering. *Surf. Sci.* **573**, 191–203.

- Ghose S.K., S.C. Petitto, K.S. Tanwar, C.S. Lo, P.J. Eng, A.M. Chaka, and T.P. Trainor (2008) Surface Structure and Reactivity of Iron Oxide Water Interfaces. *In* Barnett, M.O., and D.B. Kent (Eds.) Adsorption of Metals to Geomedia II, Elsevier, New York, NY pp. 1–24.
- Griggs, C.S., Martin, A.W., Larson, S.L., O'Connor, G., Fabian, G., Zynda, G., Mackie, D. (2011) The effect of phosphate application on the mobility of antimony in firing range soils. *Science of the Total Environment*. **409**, 12, 2397-2403.
- Guemiza, K., Mercier, G., Blais, J. (2014). Pilot-Scale Decontamination of Small-Arms Shooting Range Soil Polluted with Copper, Lead, Antimony, and Zinc by Acid and Saline Leaching. *J. Environ. Eng.* **141**, 1.
- Gurnani, N., A. Sharma, and G. Talukder (1994) Effects of antimony on cellular systems in animals – a review. *Nucleus* **37**, 71–96.
- Guo, X., Wu, Z., He, M. (2009) Removal of antimony(V) and antimony(III) from drinking water by coagulation-flocculation-sedimentation (CFS). *Water Research*, **43**, 4327-4335.
- Guo, X.; Wu, Z.; He, M.; Meng, X.; Jin, X.; Qiu, N.; Zhang, J. (2014) Adsorption of antimony onto iron oxyhydroxides: adsorption behavior and surface structure. *J. Hazard. Mater.* **276**, 339-345.
- Hansel, C.M., S.G. Benner, and S. Fendorf (2005) Competing Fe(II)-induced mineralization pathways of ferrihydrite. *Environmental Science and Technology* **39**, 7147–7153.
- Hardison, D.W., Jr., L.Q. Ma, T. Luongo, and W.G. Harris (2004) Lead contamination in shooting range soils from abrasion of lead bullets and subsequent weathering. *Science of the Total Environment* **328**, 175–183.
- Hazell, P. (2003) Numerical simulations and experimental observations of the 5.56-mm L2A2 bullet perforating steel targets of two hardness values. *Journal of Battlefield Technology* **6**.
- Heberling F., Trainor T. P., Lützenkirchen J., Eng P., Denecke M. A. and Bosbach D. (2011) Structure and reactivity of the calcite--water interface. *J. Colloid Interface Sci.* **354**, 843–857.
- Houlihan, J., and R. Wiles (2002) Lead pollution at outdoor firing ranges. Environmental Working Group, Washington, DC. www.ewg.org/reports/poisonouspastime/leadpoll.pdf.
- Ilgen, A.G., and T.P. Trainor (2012a) Sb(III) and Sb(V) sorption onto Al-rich phases: Hydrous Al oxide and the clay minerals kaolinite KGa-1b and oxidized and reduced nontronite NAu-1. *Environmental Science and Technology* **46**, 843–851.
- Ilgen, A.G., A.L. Foster, and T.P. Trainor (2012b) Role of structural Fe in nontronite NAu-1 and dissolved Fe(II) in redox transformations of arsenic and antimony. *Geochimica et Cosmochimica Acta* **94**, 128–145.

Ilgen, A.G., Majs, F., Barker, A.J., Douglas, T.A., Trainor, T.P. (2014). Oxidation and mobilization of metallic antimony in aqueous systems with simulated groundwater. *Geochimica et Cosmochimica Acta*. **132**, 16-30.

Interstate Technology and Regulatory Council (ITRC) (2003) Characterization and remediation of soils at closed small arms firing ranges.

Jansen, M. (1979) Die Kristallstruktur von Antimon(V)-oxid. *Acta Crystallographica B* **35**, 539–542.

Jardine, P.M., J.C. Parker, , M.A. Stewart, M.O. Barnett, and S.E. Fendorf (2007) Final Report, Project CU-1350 Decreasing Toxic Metal Bioavailability with Novel Soil Amendment Strategies, p. 22.

Johnson, C.A., H. Moench, P. Wersin, P. Kugler, and C. Wenger (2005) Solubility of antimony and other elements in samples taken from shooting ranges. *Journal of Environmental Quality* **34**, 248–254.

Jørgensen, S.S., and M. Willems (1987) The fate of lead in soils: The transformation of lead pellets in shooting range soils. *Ambio* **16**, 11–15.

Kang, M., Kamei, T., Magara, Y. (2003) Comparing polyaluminum chloride and ferric chloride for antimony removal. *Water Res.*, **37**, 17, 4171-4179.

Kelly, S.D., D. Hesterberg, and B. Ravel (2008) Analysis of soils and minerals using x-ray absorption spectroscopy. In Ulery, A.L., and L.R. Drees (Eds.) *Methods of Soil Analysis*. Part 5, Mineralogical Methods, Soil Science Society of America, Madison, WI, pp. 387–463.

Keto, R.O. (1999). Analysis and comparison of bullet leads by inductively-coupled plasma mass spectrometry. *J. Forensic. Sci.* **44**, 1020-1026.

Knutzen, P.J.T., J.S. Vigsnaes, R. Rasmussen , and P.S. Nissen (1995) Terminal ballistics of 7.62-mm NATO bullets: Experiments in ordnance gelatin. *International Journal of Legal Medicine* **108**, 62–67.

Krachler, M.; Emons, H.; Zheng, J.; Speciation of antimony for the 21th century: promises and pitfalls. *Trends Anal. Chem.* **2001**, *20*, 79-90.

Labare, M.P., M.A. Butkus, D. Riegner, N. Schommer, and J. Atkinson (2004) Evaluation of lead movement from the abiotic to biotic at a small-arms firing range. *Environmental Geology* **46**, 750–754.

Lamothe, P.J., A.L., Meier, and S.A. Wilson (2002) The determination of forty-four elements in aqueous samples by inductively coupled plasma-mass spectrometry. In Taggart, J.E. (Ed). *Analytical methods for chemical analysis of geological and other materials*, U.S. Geological Survey. U.S. Geological Survey open-file report 02–223.

Langmuir, D. (1997) Aqueous Environmental Geochemistry. Prentice-Hall, Upper Saddle River, New Jersey.

Lee, S.H., Lee, J.S., Choi, Y.J. Kim, J.G. (2009) In situ stabilization of cadmium-, lead-, and zinc-contaminated soil using various amendments. *Chemosphere*. **77**, 1069-1075.

Leuz, A.-K., H. Monch, and C.A. Johnson (2006) Sorption of Sb(III) and Sb(V) to goethite: Influence of Sb(III) oxidation and mobilization. *Environmental Science and Technology* **40**, 7277–7282.

Lide, D. (1993) CRC Handbook of Chemistry and Physics, 72 ed. CRC press, Boca Raton, Florida.

Lin, Z., B. Comet, U. Qvarfort, and R. Herbert (1995) The chemical and mineralogical behavior of Pb in shooting range soils from central Sweden. *Environmental Pollution* **89**, 303–309.

Lin, Z. (1996) Secondary mineral phases of metallic lead in soils of shooting ranges from Orebro County, Sweden. *Environmental Geology* **27**, 370–375.

Lo C. S., Tanwar K. S., Chaka A. M. and Trainor T. P. (2007) Density functional theory study of the clean and hydrated hematite (1-102) surfaces. *Phys. Rev. B* **75**, 75425.

Manceau, A., M.A. Marcus, and N. Tamura, (2002) Quantitative speciation of heavy metals in soils and sediments by synchrotron x-ray techniques. *Reviews in Mineralogy and Geochemistry* **49**, 341–428.

Martin, A.W., Lee, L.S., Schwab, P. (2013) Antimony migration trends from a small arms firing range compared to lead, copper, and zinc. *Science of the Total Environment*. **463-464**, 222-228.

Mason, S.E., C.R. Iceman, K.S. Tanwar, T.P. Trainor, and A.M. Chaka (2009) Pb(II) adsorption on isostructural hydrated alumina and hematite (0001) surfaces: A DFT study. *The Journal of Physical Chemistry C* **113**, 2159–2170.

Mason, S.E., T.P. Trainor, and A.M. Chaka (2011) Hybridization-reactivity relationship in Pb(II) adsorption on α -Al₂O₃-water interfaces: A DFT study. *Journal of Physical Chemistry C* **115**, 4008–4021.

Mason S. E., Trainor T. P. and Goffinet C. J. (2012) DFT study of Sb(III) and Sb(V) adsorption and heterogeneous oxidation on hydrated oxide surfaces. *Comput. Theor. Chem.* **987**, 103–114.

Martínez-Lladó X., de Pablo J., Giménez J., Ayora C., Martí V. and Rovira M. (2008) Sorption of antimony(V) onto synthetic goethite in carbonate medium. *Solvent Extr. Ion Exch.* **26**, 289–300.

McComb, K.A., Craw, D., McQuillan, A.J. (2007) ATR-IR Spectroscopic Study of Antimonate Adsorption to Iron Oxide. *Langmuir*, **23**, 24, 12125-12130.

Mitsunobu, T.; Harada, T.; Takahashi, Y. (2006) Comparison of antimony behavior with that of arsenic under various soil redox conditions. *Environ. Sci. Technol.*, **40**, 7270-7276.

Mitsunobu S., Takahashi Y. and Terada Y. (2010a) mu-XANES Evidence for the Reduction of Sb(V) to Sb(III) in Soil from Sb Mine Tailing. *Environ. Sci. Technol.* **44**, 1281–1287.

Mitsunobu S., Takahashi Y., Terada Y. and Sakata M. (2010b) Antimony(V) Incorporation into Synthetic Ferrihydrite, Goethite, and Natural Iron Oxyhydroxides. *Environ. Sci. Technol.* **44**, 3712–3718.

Mitsunobu S., Muramatsu C., Watanabe K. and Sakata M. (2013) Behavior of Antimony(V) during the Transformation of Ferrihydrite and Its Environmental Implications. *Environ. Sci. Technol.* **47**, 9660–9667.

Moon, D.H., Cheong, K.H., Khim, J., Wazne, M., Hyun, S., Park, J.H., Chang, Y.Y., Ok, Y.S. (2013a) Stabilization of Pb²⁺ and Cu²⁺ contaminated firing range soil using calcined oyster shells and waste cow bones. *Chemosphere*, **91**, 1349-1354.

Moon, D.H., Park, J.W., Cheong, K.H., Hyun, S., Koutsospyros, A., Park, J.H., Ok, Y.S. (2013b) Stabilization of lead and copper contaminated firing range soil using calcined oyster shells and fly ash. *Environ. Cheochem. Health.* **35**, 705-714.

Moon, D.H., Park, J.W., Chang, Y.Y., Ok, Y.S., Lee, S.S., Ahmad, M., Koutsospyros, A., Park, J.H., Baek, K. (2013c) Immobilization of lead in contaminated firing range soil using biochar. *Environ. Sci. Pollut. Res.* **13**, 1964-1967.

Murray, K., A. Bazzi, C. Carter, A. Ehlert, A. Harris, M. Kopec, J. Richardson, and H. Sokol (1997) Distribution and mobility of lead in soils at an outdoor shooting range. *Journal of Soil Contamination* **6**, 79–93.

Nevin, K.P., and D.R. Lovley (2002) Mechanisms for Fe(III) oxide reduction in sedimentary environments. *Geomicrobiology Journal* **19**, 141–159.

Newville, M. (2001) IFEFFIT: Interactive XAFS analysis and FEFF fitting. *Journal of Synchrotron Radiation* **8**, 322–324.

Newville, M., P. Livins, Y. Yacoby, J.J. Rehr, and E.A. Stern (1993) Near-edge x-ray-absorption fine structure of Pb: A comparison of theory and experiment. *Physical Review B* **47**, 14126–14131.

Okkenhaug, G.; Amstätter, K.; Bue, H.L.; Cornelissen, G.; Breedveld, G.D.; Henriksen, T.; Mulder, J. (2013) Antimony (Sb) Contaminated Shooting Range Soil: Sb Mobility and Immobilization by Soil Amendments. *Environ. Sci. Technol.* **47**, 6431-6439.

Okkenhaug, G. Gebhardt, K.A.G., Amstaetter, K., Bue, H.L., Herzel, H., Mariussen, E., Almås, A.R., Cornelissen, G., Breedveld, G.D., Rasmussen, G., Mulder, J. (2016). Antimony (Sb) and lead (Pb) in contaminated shooting range soils: Sb and Pb mobility and immobilization by iron based sorbents, a field study. *Journal of Hazardous Materials*, **307**, 336-343.

Ostergren, J.D., G.E. Brown, Jr., G.A. Parks, and T.N. Tingle (1999). Quantitative speciation of lead in selected mine tailings from Leadville, CO. *Environmental Science and Technology* **33**, 1627–1636.

Ostergren, J.D., T.P. Trainor, J.R. Bargar, G.E. Brown, Jr., and G.A. Parks (2000a) Inorganic ligand effects on Pb(II) sorption to goethite (α -FeOOH) I. Carbonate. *Journal of Colloid and Interface Science* **225**, 466–482.

Ostergren, J.D., G.E. Brown, Jr., G.A. Parks, and P. Persson (2000b) Inorganic ligand effects on Pb(II) sorption to goethite (α -FeOOH) II. Sulfate. *Journal of Colloid and Interface Science* **225**, 483–493.

Park, C., and P.A. Fenter (2007) Phasing of resonant anomalous x-ray reflectivity spectra and direct Fourier synthesis of element-specific partial structures at buried interfaces. *Journal of Applied Crystallography* **40**, 290–301.

Randich, E., W. Duerfeldt, W. McLendon, and W. Tobin (2002) A metallurgical review of the interpretation of bullet lead compositional analysis. *Forensic Science International* **127**, 174–191.

Regelink, I.C.; Weng, L.; Koopmans, G.F.; van Riemsdijk, W.H. (2013) Asymmetric flow field-flow fractionation as a new approach to analyse iron-(hydr)oxide nanoparticles in soil extracts. *Geoderma*, **202-203**, 134-141.

Ritchie, V.J., A.G. Ilgen, S.H. Mueller, T.P. Trainor, and R.J. Goldfarb (2013) Mobility and chemical fate of antimony and arsenic in historic mining environments of the Kantishna Hills District, Denali National Park and Preserve, Alaska. *Chemical Geology*, **335**, 172-188.

Robinson, I.K. (1986) Crystal truncation rods and surface roughness. *Physical Review B* **33**, 3830–3836.

Roden, E.E., and J.M. Zachara (1996) Microbial reduction of crystalline Fe(III) oxides: Influence of oxide surface area and potential for cell growth. *Environmental Science and Technology* **30**, 1618–1628.

Rooney, C.P., McLaren, R.G., Cresswell, R.J. (1999) Distribution and phytoavailability of lead in a soil contaminated with lead shot. *Water, Air and Soil Pollution*, **116**, 3, 535-548.

Rooney, C.P., McLaren, R.G., Condon, L.M. (2007) Control of lead solubility in soil contaminated with lead shot: Effect of soil pH. *Environmental Pollution*, **149**, 149-157.

Sanderson, P., Naidu, R., Bolan, N. (2013) Effectiveness of chemical amendments for stabilization of lead and antimony in risk-based land management of soils of shooting ranges. *Environ. Sci. Pollut. Res.* **22**, 8942-8956. DOI 10.1007/s11356-013-1918-0.

Scheinost, A.C., A. Rossberg, D. Vantelon, I. Xifra, R. Kretzschmar, A.-K. Leuz, H. Funke, and C.A. Johnson (2006). Quantitative antimony speciation in shooting-range soils by EXAFS spectroscopy. *Geochimica et Cosmochimica Acta* **70**, 3299–3312.

Scheuhammer, A.M., and S.L. Norris (1995) A review of the environmental impacts of lead shotshell ammunition and lead fishing weights in Canada. Report 88, Minister of Environment, Canadian Wildlife Service, Ottawa, ON.

Sporting Arms and Ammunition Manufacturers' Institute, SAAMI (1996) Lead mobility at shooting ranges. Facility Development Series, No.1., Newtown, CT.

Spuller, C., Weigand, H., Marb, C. (2007) Trace metal stabilisation in a shooting range soil: Mobility and phytotoxicity. *Journal of Hazardous Materials Stabilisation/Solidification Treatment and Remediation: Advances in S/S for Waste and Contaminated Land*. **141**, 378-387.

Strategic Environmental Research and Development Program (October, 2007) Final Report: SERDP and ESTCP Technical Exchange Meeting on DoD Operational Range Assessment and Management Approaches, 114 pages.

Strawn, D.G., and D.L. Sparks (1999). The use of XAFS to distinguish between inner- and outer-sphere lead adsorption complexes on montmorillonite. *Journal of Colloid and Interface Science* **216**, 257–269.

Strømseng, A.E., Ljones, M., Bakka, L., Mariussen, E. (2009). Episodic discharge of lead copper and antimony from a Norwegian small arm shooting range. *J. Environ. Monit.* **11**, 6, 1259-1267.

Sturchio, N.C., R.P. Chiarello, L. Cheng, P.F. Lyman, M.J. Bedzyk, M.J. Qian, H. You, D. Yee, P. Geissbuhler, L.B. Sorensen, L.B. Liang, and D.R. Baer (1997) Lead adsorption at the calcite-water interface: Synchrotron x-ray standing wave and x-ray reflectivity studies. *Geochimica et Cosmochimica Acta* **61**, 251–263.

Taggart, J.E. (2002) Analytical methods for chemical analysis of geologic and other materials, U.S. Geological Survey, U.S. Geological Survey open-file report 02–223.

Tanwar K.S., C.S. Lo, P.J. Eng, J.G. Catalano, D.A. Walko, G.E. Brown Jr., G.A. Waychunas, A.M Chaka, and T.P. Trainor (2007a) surface diffraction study of the hydrated hematite (1-102) surface. *Surface Science* **601**, 460–474.

Tanwar K.S., J.G. Catalano, S.C. Petitto, S.K. Ghose, P.J. Eng, T.P. Trainor (2007b) Surface preparation dependent structure of γ -Fe₂O₃ (1-102). *Surface Science* **601**, L59–L64.

Tanwar K.S., S.C. Petitto, S.K. Ghose, P.J. Eng, and T.P. Trainor (2008) Structural study of Fe(II) adsorption on hematite (1-102). *Geochimica et Cosmochimica Acta* **72**, 3311–3325.

Templeton, A.S., T.P. Trainor, A.M. Sporemann, M. Newville, S.R. Sutton, A. Dohnalkova, Y. Gorbi, and G.E. Brown, Jr. (2003a). Sorption vs biomineralization of Pb(II) within Burkholderia cepacia biofilms. *Environmental Science and Technology* **37**, 300–307.

Templeton, A.S., T.P. Trainor, A.M. Spormann, and G.E. Brown, Jr., Selenium speciation and partitioning within *Burkholderia cepacia* biofilms formed on alpha-Al₂O₃ surfaces. *Geochimica et Cosmochimica Acta* (2003b) **67**, 3547–3557.

Tessier, A., P.G.C. Campbell, and M. Bisson (1979). Sequential extraction procedure for the speciation of particulate trace metals. *Analytical Chemistry* **51**, 844–851.

Thanabalasingam, P., and W.F. Pickering (1990) Specific sorption of antimony (III) by the hydrous oxides of Mn, Fe, and Al. *Water, Air, and Soil Pollution* **49**, 175–185.

Theodorakos, P.M., (2002a), Fluoride, chloride, nitrate, and sulfate in aqueous solution utilizing autosuppression chemically suppressed ion chromatography. In Taggart, J.E. (Ed.) Analytical methods for chemical analysis of geological and other materials, U.S. Geological Survey. U.S. Geological Survey open-file report 02–223.

Theodorakos, P.M., (2002b). Ferrous iron (Fe²⁺) from 0 to 3.00 mg/L for water, wastewater, and seawater utilizing the HACH DR/2010 spectrophotometer method. In Taggart, J.E. (Ed.) Analytical methods for chemical analysis of geological and other materials, U.S. Geological Survey. U.S. Geological Survey open-file report 02–223.

Trainor T.P., P.J. Eng, G.E. Brown Jr., I.K. Robinson, and M. De Santis (2002a) Crystal truncation rod diffraction study of the <-Al₂O₃ (1-102) surface. *Surface Science* **496**, 238–250.

Trainor, T.P., P.J. Eng, and I.K. Robinson (2002b) Calculation of crystal truncation rod structure factors for arbitrary rational surface terminations. *Journal of Applied Crystallography* **35**, 696–701.

Trainor T.P., A.C. Chaka, P.J. Eng, M. Newville, J. Catalano, G.A. Waychunas, and G.E. Brown Jr. (2004) Structure and reactivity of the hydrated hematite (0001) surface. *Surface Science* **573**, 204–224.

Trainor T.P., A.S. Templeton, and P.J. Eng (2006) Structure and reactivity of environmental interfaces: Application of grazing angle x-ray spectroscopy and long-period x-ray standing waves. *Journal of Electron Spectroscopy and Related Phenomena* **150**, 66–85.

Trivedi P., Dyer J. A. and Sparks D. L. (2003) Lead Sorption onto Ferrihydrite. 1. A Macroscopic and Spectroscopic Assessment. *Environ. Sci. Technol.* **37**, 908–914.

United States Environmental Protection Agency (2001) Best management practices for lead at outdoor shooting ranges. EPA-902-B01-001.

United States Environmental Protection Agency (2009) National primary drinking water regulations. EPA 816-F-09-004.

Vantelon, D., A. Lanzirotti, A. Scheinost, and R. Kretzschmar (2005) Spatial distribution and speciation of lead around corroding bullets in a shooting range soil studied by micro-x-ray fluorescence and absorption spectroscopy. *Environmental Science and Technology* **39**, 4808–4815.

Venema, P., T. Hiemstra, and W.H. van Riemsdijk (1996) Multisite adsorption of cadmium on goethite. *Journal of Colloid and Interface Science* **183**, 515–527.

Villalobos, M., M.A. Trotz, and J.O. Leckie (2001) Surface complexation modeling of carbonate effects on the adsorption of Cr(VI), Pb(II) and U(VI) on goethite. *Environmental Science and Technology* **35**, 3849–3856.

Vink, B.W. (1996) Stability relations of antimony and arsenic compounds in the light of revised and extended Eh-pH diagrams. *Chemical Geology* **130**, 21–30.

Vithanage M., Rajapaksha A. U., Dou X., Bolan N. S., Yang J. E. and Ok Y. S. (2013) Surface complexation modeling and spectroscopic evidence of antimony adsorption on iron-oxide-rich red earth soils. *J. Colloid Interface Sci.* **406**, 217–224.

Walsh, M.E. (2004) Field-Portable X-Ray Fluorescence (FP-XRF) Determinations of Metals in Post-Blast Ordnance Residue. ERDC/CRREL Technical Report 04-05, 33 pages.

Waychunas, G.A. (2002) Grazing-incidence x-ray absorption and emission spectroscopy. *Reviews in Mineralogy and Geochemistry* **49**, 267–315.

Yanina, S.V., and K.M. Rosso (2008) Linked reactivity at mineral–water interfaces through bulk crystal conduction. *Science* **320**, 218–222.

Zachara, J.M., J.K. Fredrickson, S.C. Smith, and P.L. Gassman (2001) Solubilization of Fe(III) oxide-bound trace metals by a dissimilatory Fe(III) reducing bacterium. *Geochimica et Cosmochimica Acta* **65**, 75–93.

Zheng J., M. Ohata, and N. Furuta (2000), Antimony speciation in environmental samples by using high-performance liquid chromatography coupled to inductively coupled mass spectrometry. *Analytical Sciences* **16**, 75–80.

Zimdahl, R., and R. Skogerboe (1977) Behavior of lead in soil. *Environmental Science and Technology* **11**, 1202–1207.

Appendix A. Supporting Data

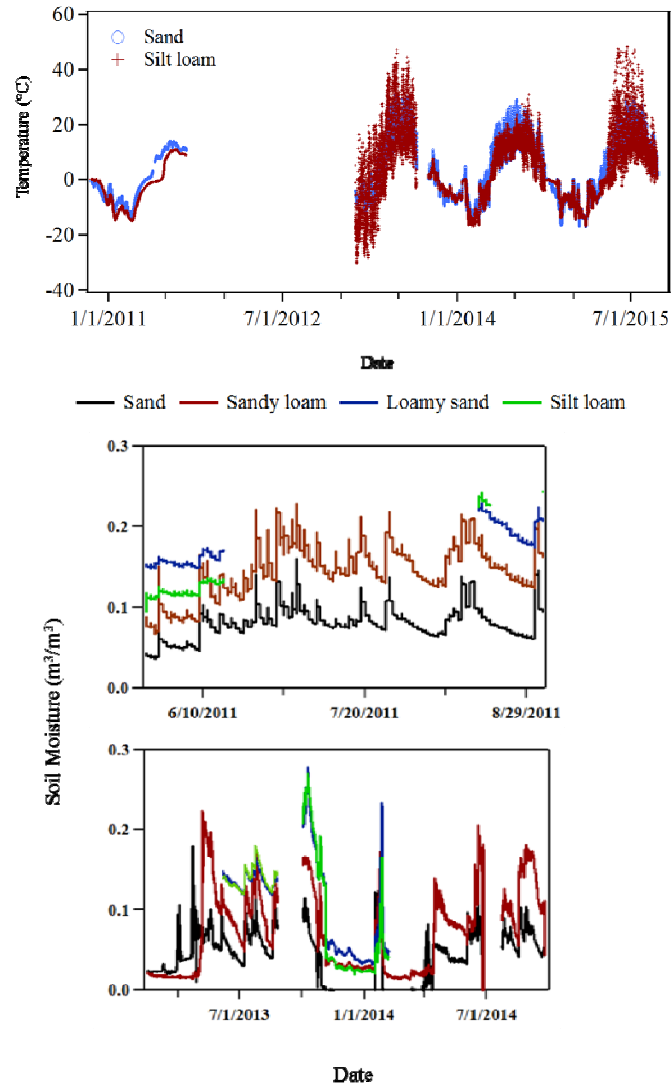


Figure A1. Soil temperature and soil moisture content in the experimental berms.

Jacket		Mass (g)
	Cu	17.82
	Zn	1.96
	Pb	0.01
	Fe	0.01
Core		
	Fe	9.80
	Mn	0.08
	C	0.05
	S	0.01
Slug		
	Pb	31.68
	Sb	0.32

Table A1. Bullet chemical composition provided by Defense Ammunition Center (DAC) Munitions Items Disposition Action System (MIDAS).

Year	Berm	Soil type	Spot	Sb(0)	Sb ₂ O ₅	Sum (%)	X ²	red. X ²
2	12	Loam	1	100		100	9.3E-02	5.6E-04
2	12	Loam	2		100	100	2.7E-01	1.5E-03

Table A2. Fitting parameters for the LCF of the normalized Sb-L_{III} μ -XANES from the silt loam constructed target berm with Sb⁰ standard and Sb₂O₅.

Year	Berm	Soil type	Name	Pb(0)	L	C	H	Ferri	Sum (100%)	X ²	red. X ²
1	5	Sand	S-1	65 (1)	14 (1)	23 (1)			101	9.6E-03	7.0E-05
2	5	Sand	S-2	~99					99	1.1E-02	8.1E-05
2	5	Sand	S-3	~100					100	1.8E-02	1.3E-04
3	5	Sand	S-4		45 (1)	28 (2)	26 (1)		99	1.4E-02	1.1E-04
3	5	Sand	S-5			37 (1)	38 (1)		95	8.9E-03	7.0E-05
4	5	Sand	S-6		20 (2)			74 (1)	93	2.1E-02	1.5E-04
2	12	Silt loam	L-1	~100					101	1.6E-02	1.3E-04
2	12	Silt loam	L-2	15 (3)	10 (3)	50 (2)	25 (2)		100	1.1E-02	7.9E-05
3	12	Silt loam	L-3	100					100	1.8E-02	1.3E-04
3	12	Silt loam	L-4		16 (1)	70 (3)	14 (1)		100	1.8E-02	1.3E-04
4	12	Silt loam	L-5		26 (1)	30 (3)	23 (1)	22 (1)	100	1.1E-02	8.0E-05
4	12	Silt loam	L-6		17 (1)	63 (3)	10 (1)	11 (2)	100	1.3E-02	9.4E-05

*Refers to Pb(II) sorption product with synthesized Fe(III)oxides

(#) Refers to linear combination fitting error

Table A3. Select linear combination fitting results for the constructed target berms using Pb reference spectra, samples were collected in 2011-2014. Sum (%) refers to the actual sum of the partial contributions for the overall best fit. X² and reduced X² are derived from the fit refinement process. Pb(0) = Metallic bullet alloy; L = Litharge (PbO); C = Cerussite; H = Hydrocerussite; Ferri = Pb(II) sorbed on synthesized Fe(III)oxides; error associated with fit in parenthesis.

Sample	¹⁾ k-range	R-range (Å)	Shell	²⁾ CN	³⁾ R (Å)	⁴⁾ σ^2 (Å ²)	⁵⁾ ΔE_0 eV	⁶⁾ R-factor	⁷⁾ Red χ^2	⁸⁾ Ind. Pts.
Senarmontite	2.7-12.6	1.0-4.5	Sb-O	3.6(2)	1.97(1)	0.003(1)	8.3(7)	0.006	243	22
			Sb-Sb	2.4(5)	3.61(1)	0.003(1)				
			Sb-Sb	1.1(7)	3.96(3)	0.004(3)				
Antimony metal	1.8-11.7	1.0-5.0	Sb-Sb	1.8(2)	2.89(1)	0.003(1)	6(1)	0.046	48.6	25
			Sb-Sb	0.8(3)	3.32(2)	0.003(2)				
			Sb-Sb	1.6(6)	4.31(2)	0.003(2)				
			Sb-Sb	1.7(7)	4.48(2)	0.003(2)				
SGW/Sb (5 months)	2.8-12.0	1.0-5.0	Sb-O	1.8(1)	1.97(1)	0.003(1)	10.3(7)	0.009	27	23
			Sb-Sb	1.0(1)	2.91(1)	0.003(1)				
			Sb-Sb	0.7(3)	3.35(2)	0.004(2)				
			Sb-Sb	1.4(3)	3.61(1)	0.004(1)				
			Sb-Sb	0.5(5)	3.93(6)	0.005(6)				
			Sb-Sb	0.5(6)	4.24(8)	0.005(7)				
DI/Sb (5 months)	2.7-11.9	1.0-4.5	Sb-O	1.4(1)	1.96(1)	0.004(1)	9(1)	0.008	57	20
			Sb-Sb	0.7(1)	2.89(1)	0.002(1)				
			Sb-Sb	0.8(2)	3.36(1)	0.004(1)				
			Sb-Sb	1.5(3)	3.60(1)	0.004(1)				
			Sb-Sb	0.8(4)	3.90(2)	0.004(2)				
			Sb-Sb	1.3(6)	4.36(2)	0.006(2)				

Table A4. Final EXAFS fitting parameters for Sb samples from batch laboratory oxidation experiments. Fitting done in R-space, k-weights of 1, 2, and 3 were fitted simultaneously, the amplitude reduction factor S_0 was 0.97. Error at a 95% confidence level is shown in parenthesis. ¹ Usable k-range, ² Coordination number, ³ Bond length, ⁴ Debye-Waller factors: mean-square amplitude reduction factor, including thermal and static disorder components, ⁵ Energy shift between the theoretical and measured spectrum, ⁶ R-factor (mean square misfit), ⁷ Reduced chi-square, ⁸ Number of independent points.

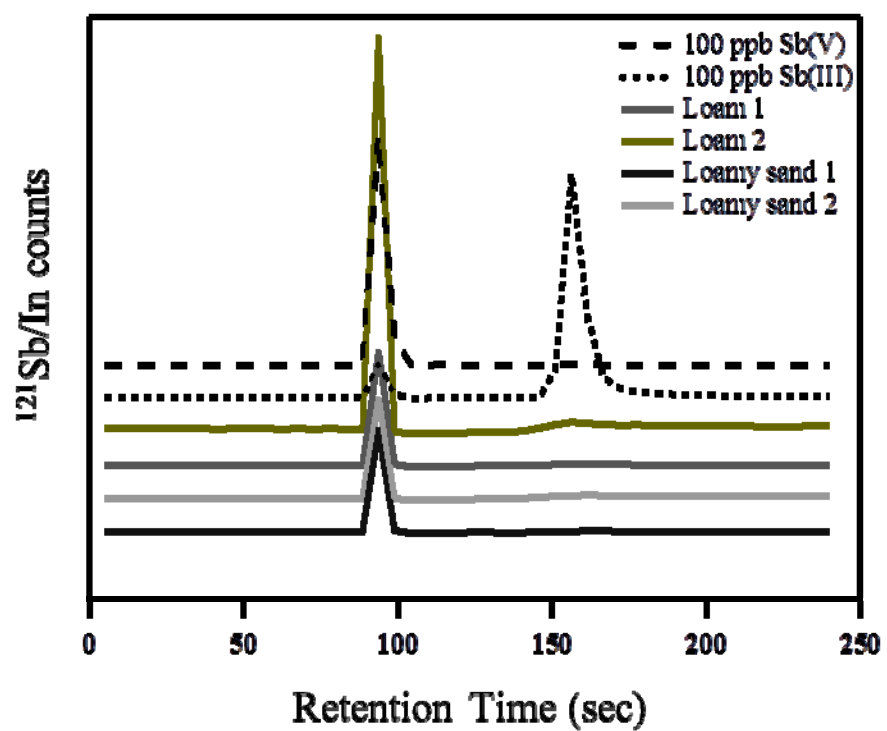


Figure A2. Antimony aqueous speciation in porevolume sample 1 and 2 from silt loam and loamy sand columns.

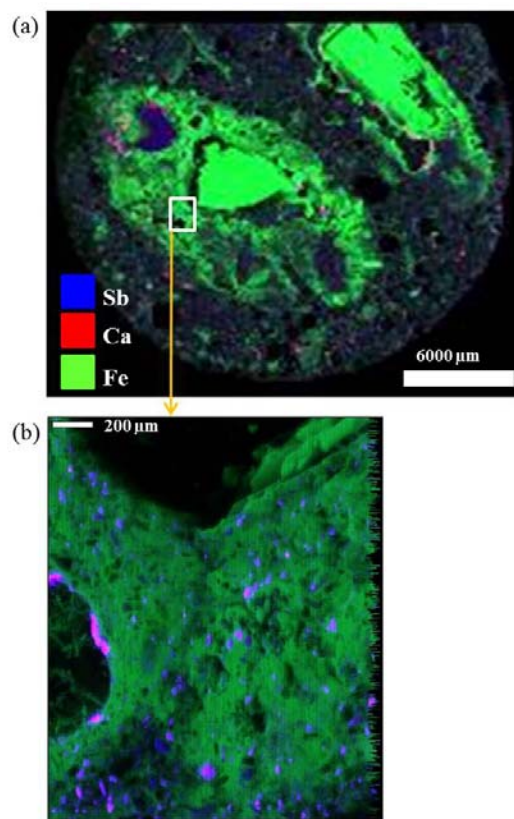


Figure A3. XRF maps showing the distribution of Sb (blue), Ca (red) and Fe (green) in the silt loam soil (a) macro-scale ~1x1mm soil plug thin section the remaining maps are sample subsets of various hotspots for microanalysis.

Models	Binding sites		Binding modes		Protonation schemes of surface functional groups*		FOM
	HLT	FLT	HL	FL	HL	FL	
O1O2	O ₁ O ₂ , O ₁ O _{2+y}	clean	CS	N/A	Pb-(^I OH) ₂ -(^{II} OH) ₂ -Fe ₂ -O ₂ - R	(^I OH ₂) ₂ -(^{III} OH) ₂ -Fe ₂ -O ₂ -Fe ₂ -O ₂ - R	5.0
O1O3	O ₁ O ₃ , O ₂ O _{4+x}	clean	ES	N/A	Pb-(^I OH ^I OH ₂)-(^{II} O ^{II} OH)-Fe ₂ -O ₂ - R	(^I OH ₂) ₂ -(^{III} OH) ₂ -Fe ₂ -O ₂ -Fe ₂ -O ₂ - R	6.0
O1O4	O ₁ O _{4+y} , O ₂ O _{3+x}	clean	ES	N/A	Pb-(^I OH ^I OH ₂)-(^{II} O ^{II} OH)-Fe ₂ -O ₂ - R	(^I OH ₂) ₂ -(^{III} OH) ₂ -Fe ₂ -O ₂ -Fe ₂ -O ₂ - R	5.8
O5O6	clean	O ₅ O ₆ , O ₅ O _{6+y}	N/A	CS	(^I OH ₂) ₂ -(^{II} OH) ₂ -Fe ₂ -O ₂ - R	Pb-(^I OH) ₂ -(^{III} OH) ₂ -Fe ₂ -O ₂ -Fe ₂ -O ₂ - R	4.9
O5O7	clean	O ₅ O _{7+x} , O ₆ O ₈	N/A	ES	(^I OH ₂) ₂ -(^{II} OH) ₂ -Fe ₂ -O ₂ - R	Pb-(^I OH ^I OH ₂)-(^{III} O ^{III} OH)-Fe ₂ -O ₂ -Fe ₂ -O ₂ - R	5.4
O5O8	clean	O ₅ O _{8+x} , O _{6+y} O ₇	N/A	ES	(^I OH ₂) ₂ -(^{II} OH) ₂ -Fe ₂ -O ₂ - R	Pb-(^I OH ^I OH ₂)-(^{III} O ^{III} OH)-Fe ₂ -O ₂ -Fe ₂ -O ₂ - R	5.2
O1O3_O5O7	O ₁ O ₃ , O ₂ O _{4+x}	O ₅ O _{7+x} , O ₆ O ₈	ES	ES	Pb-(^I OH ^I OH ₂)-(^{II} O ^{II} OH)-Fe ₂ -O ₂ - R	Pb-(^I OH ^I OH ₂)-(^{III} O ^{III} OH)-Fe ₂ -O ₂ -Fe ₂ -O ₂ - R	5.5
O1O3_O5O8	O ₁ O ₃ , O ₂ O _{4+x}	O ₅ O _{8+x} , O _{6+y} O ₇	ES	ES	Pb-(^I OH ^I OH ₂)-(^{II} O ^{II} OH)-Fe ₂ -O ₂ - R	Pb-(^I OH ^I OH ₂)-(^{III} O ^{III} OH)-Fe ₂ -O ₂ -Fe ₂ -O ₂ - R	5.4
O1O4_O5O7	O ₁ O _{4+y} , O ₂ O _{3+x}	O ₅ O _{7+x} , O ₆ O ₈	ES	ES	Pb-(^I OH ^I OH ₂)-(^{II} O ^{II} OH)-Fe ₂ -O ₂ - R	Pb-(^I OH ^I OH ₂)-(^{III} O ^{III} OH)-Fe ₂ -O ₂ -Fe ₂ -O ₂ - R	5.5
O1O4_O5O8	O ₁ O _{4+y} , O ₂ O _{3+x}	O ₅ O _{8+x} , O _{6+y} O ₇	ES	ES	Pb-(^I OH ^I OH ₂)-(^{II} O ^{II} OH)-Fe ₂ -O ₂ - R	Pb-(^I OH ^I OH ₂)-(^{III} O ^{III} OH)-Fe ₂ -O ₂ -Fe ₂ -O ₂ - R	5.2
O5O7_O5O8	clean	O ₅ O _{7+x} , O ₆ O ₈ , O ₅ O _{8+x} , O _{6+y} O ₇	N/A	ES	Pb-(^I OH ^I OH ₂)-(^{II} O ^{II} OH)-Fe ₂ -O ₂ - R	(^I OH ₂) ₂ -(^{III} OH) ₂ -Fe ₂ -O ₂ -Fe ₂ -O ₂ - R	3.9
O1O3_O1O4	O ₁ O ₃ , O ₂ O _{4+x} , O ₁ O _{4+y} , O ₂ O _{3+x}	clean	ES	N/A	Pb-(^I OH ^I OH ₂)-(^{II} O ^{II} OH)-Fe ₂ -O ₂ - R	(^I OH ₂) ₂ -(^{III} OH) ₂ -Fe ₂ -O ₂ -Fe ₂ -O ₂ - R	2.2

Table A5. A description of the binding sites, binding modes and possible protonation schemes associated with the different model trials for Pb on the hematite (**1102**) surface. HL and FL represent the half layer termination and the full layer termination surfaces, respectively. CS, ES represent corner-sharing, edge-sharing binding mode, respectively. The naming rules for binding sites are followed as described in Figure 33 (C and D). A suffix with a term ‘+x’ or ‘+y’ in the binding sites denotes the associated atom after translating along **a**_s or **b**_s axis by one unit cell. *The proposed protonation schemes are based on the bond valence analysis using the ideal surface structure. The protonation schemes in the real situation for the best fit model could be different from those for the ideal case (see the text for detail). **R** represents the stoichiometric repeat of the atom layers (O₂-Fe₂-O₂-Fe₂-O₂) along **c**_s axis.

Termination patterns	Binding sites	Binding configurations	Binding modes	Model trials	FOM ^a
FLT	O ₅ O ₆ , O ₅ O _{6+y}	Corner-sharing	Bidentate	Model1	10.08
	O ₅ O _{7+y} , O ₆ O ₈	Edge-sharing	Bidentate	Excluded	-
	O ₅ O _{8+x} , O ₆ O _{7-y}	Edge-sharing	Bidentate	Excluded	-
	O ₅ O _{6+y} O ₇ , O ₅ O ₆ O _{8+x}	Corner/edge-sharing	Tridentate	Model2	6.94
	O ₅ O _{7+x} O _{8+x} , O ₆ O _{7-y} O ₈	Face-sharing	Tridentate	Model3	9.88
HLT	O ₁ O ₂ , O ₁ O _{2+y}	Corner-sharing	Bidentate	Model4	710.32
	O ₁ O ₃ , O ₂ O _{4+x}	Edge-sharing	Bidentate	Excluded	-
	O ₁ O _{4+y} , O ₂ O _{3+x}	Edge-sharing	Bidentate	Excluded	-
	O ₁ O ₂ O ₃ , O _{1-y} O ₂ O _{4+x}	Corner/edge-sharing	Tridentate	Model5	2.25
	O ₁ O ₃ O _{4+y} , O ₂ O _{3+x} O _{4+x}	Face-sharing	Tridentate	Model6	10.73

Table A6. Potential binding sites for Sb(V) on the hematite (**1102**) surface and goodness-of-fit for different models. ^aThe FOM has been scaled by the bond valence penalty factor.

Appendix B. List of Publications

Barker, A.J., Douglas, T.A., Ilgen, A.L., Trainor, T.P. (In prep) Lead and antimony speciation associated with weathering bullets in newly constructed test berms. Prepared for submission in *Geochimica et Cosmochimica Acta*.

Barker, A.J., Mayhew, L.E., Douglas, T.A., Ilgen, A.L., Trainor, T.P. (In prep) Lead and antimony speciation associated with the weathering of bullets in a historic shooting range in Alaska. Prepared for submission in *Science of the Total Environment*.

Barker, A.J., Douglas, T.A., Spaleta, K.J., Trainor, T.P. (In prep) Attenuation of Pb and Sb in shooting range soils by Fe amendments. Prepared for submission in *Geochimica et Cosmochimica Acta*.

Ilgen, A.G., and T.P. Trainor (2012) Sb(III) and Sb(V) sorption onto Al-rich phases: Hydrated Al oxide and the clay minerals kaolinite KGA-1b and oxidized and reduced nontronite NAu-1. *Environmental Science and Technology* **46**, 843–851.

Ilgen, A.G., A.L. Foster, and T.P. Trainor (2012) Role of structural Fe in nontronite NAu-1 and dissolved Fe(II) in redox transformations of arsenic and antimony. *Geochimica et Cosmochimica Acta* **94**, 128–145.

Ilgen, A.G., Majs, F., Barker, A.J., Douglas, T.A., Trainor, T.P. (2014). Oxidation and mobilization of metallic antimony in aqueous systems with simulated groundwater. *Geochimica et Cosmochimica Acta*. **132**, 16-30.

Ilgen, A.G., and T.P. Trainor (2016) Homogeneous oxidation of Sb(III) by aqueous O₂: the effect of ionic strength, Pb(II) and EDTA. *Environmental Chemistry*, **13**, 936-944.

Mason S. E., Trainor T. P. and Goffinet C. J. (2012) DFT study of Sb(III) and Sb(V) adsorption and heterogeneous oxidation on hydrated oxide surfaces. *Comput. Theor. Chem.* **987**, 103–114.

Ritchie, V.J., A.G. Ilgen, S.H. Mueller, T.P. Trainor, and R.J. Goldfarb (2013) Mobility and chemical fate of antimony and arsenic in historic mining environments of the Kantishna Hills District, Denali National Park and Preserve, Alaska. *Chemical Geology*, **335**, 172-188.

Qiu, C., F. Majs, P.J. Eng, J.E. Stubbs, T.A. Douglas, M. Schmidt, T.P. Trainor (In prep) Structural study of Pb(II) on the hydrated hematite (1-102) surface.

Qiu, C., F. Majs, P.J. Eng, J.E. Stubbs, T.A. Douglas, T.P. Trainor (In prep) Structural study of Pb(II) on the annealed and hydrated hematite (1-102) surface.

Qiu, C., F. Majs, P.J. Eng, J.E. Stubbs, T.A. Douglas, M. Schmidt, T.P. Trainor (In prep) Structural study of Sb(V) on the hydrated hematite (1-102) surface.